INTERFACIAL INSTABILITY DRIVEN GROWTH OF LOW DIMENSIONAL STRUCTURES

Thesis submitted to
JADAVPUR UNIVERSITY
for the degree of
DOCTOR OF PHILOSOPHY (SCIENCE)

by

JAYANTA KR. BAL

Surface Physics Division
Saha Institute of Nuclear Physics
Kolkata, India

December, 2010

CERTIFICATE FROM THE SUPERVISOR

This is to certify that the thesis entitled "**INTERFACIAL INSTABILITY DRIVEN GROWTH OF LOW DIMENSIONAL STRUCTURES**" submitted by Sri **Jayanta Kr. Bal**, who got his name registered on **26.05.2009** for the award of Ph.D. (Science) degree of Jadavpur University, is absolutely based upon his own work under the supervision of **Prof. Satyajit Hazra** and that neither this thesis nor any part of it has been submitted for any degree/diploma or any academic award anywhere before.

_____

(Signature of the Supervisor & date with official seal)

To my family

Acknowledgements

The thesis dissertation marks the end of a long and eventful journey for which there are many people that I would like to acknowledge for their support along the way.

My first and foremost acknowledgement must go to my advisor, Prof. Satyajit Hazra for his sincere guidance, inspiration and patience from the very early stage of this research as well as giving me extraordinary experiences through out the work. He has taught me, both consciously and unconsciously, how good experimental physics is done and how a ordinary presentation can be made extraordinary. Above all and the most needed, he provided me unflinching encouragement and support in various ways. His truly scientist intuition has made him as a constant oasis of ideas and passions in science, which exceptionally inspire and enrich my growth as a student, a researcher and a scientist want to be. I am indebted to him more than he knows.

I am indebted to Dr. Sarathi Kundu for general help, encouragement and useful discussions and particularly, for his direct involvement in the work presented in chapter 7. I would like to thank him for being the first person who taught me how to prepare a Langmuir-Blodgett film. I am proud to record that I had several opportunities to work with an exceptionally experienced researcher like him.

I would like to extend my sincere thanks to Prof. Milan K. Sanyal, Director of our Institute and Head of Surface Physics Division for providing the necessary facilities and his constant encouragement and support throughout my Ph.D. tenure.

also thankful to hostel cooks, Shakti-da, Suresh-da and Madhu-da and Kartik-da for providing excellent healthy food.

It is a pleasure to express my gratitude wholeheartedly to Prof. Dr. Ullrich Pietsch for his kind hospitality during my stay in Siegen, Germany.

Finally, I would like to share this moment of happiness with my family. Their cheerful faces have motivated me to overcome the difficult times beyond the academic. They have rendered enormous support and constant encouragement throughout this long journey. Without the care, love and blessings of my family I could never have completed my work. This thesis mostly owes to them.

Jayanta Kr. Bal
Saha Institute of Nuclear Physics
Kolkata, India
December, 2010.

Contents

Chapter 1

Introduction

Low dimensional systems are those in which the size of the materials is reduced to nanometer length scale, in atleast one direction or dimension (D). Such reduction can however, be in one, two or in all three directions and accordingly one can have 2D (nanolayers), 1D (nanowires) and 0D (nanoparticles or nanodots) systems, respectively. Low dimensional systems or nanomaterials demonstrate properties that are sometime completely different from bulk one [1; 2]. Confinement effect and the large surface to volume ratio of nanomaterials are some of the reasons behind such behavior. Among the low dimensional systems, nanolayers grown on semiconductor substrates have received much attention due to their critical importance in different device applications such as integrated circuits (ICs), optoelectronics, microelectronics, biosensors, catalysis, etc. The wide use of nanolayer/semiconductor heterostructure in important engineering applications also has initiated extensive research on nanolayer materials. The explosion in both academic and industrial interest in these materials over the past few decades arises from the remarkable variations in fundamental optical, electrical and magnetic properties that occur as one progress from an 'infinite extended' solid to a low dimensional system consisting of a countable number of atoms. These properties are strongly correlated with the structures of low dimensional systems. For example, high sheet resistances due to the rough surface morphologies (arises due to poor wettability) of Ag and Au

layers, have been observed on electrically insulating substrates [3] which led to diminished device yields and poor optical quality, repeatability and reliability [4; 5]. Structure can be modified and even can be made smooth by incorporation of certain layer at the film-substrate interface [6; 7]. This suggests that the structure of overlayer or nanolayer is strongly dependent on the nature of the underlying substrate surface where it is grown. That means both the substrate surface and the nanolayer-substrate interface plays significant role in the growth and stability of the overlayer.

Despite the practical importance, the fundamental understanding of surface and interface phenomena is rather slow, as the progress of surface science is taking shape through trial-and-error empirical approaches. This is due to the complexity of studying the surface-interface phenomena. From the words of W. Pauli, "God created the bulk and the Devil made the surface" it can be understood about the complexity. Surface and interface structures are determined by the relative importance of many small effects. For example, the structure of a clean surface, elastic strain, Coulomb, rehybridization, exchange and correlation energies, all of them contribute to the total energy. As a result, the surface atoms often undergo relatively large displacements compared to their positions in an infinite bulk crystal. The main difficulty lies in tracking such surface atoms in high resolution using nondestructive way, especially when they are buried inside (i.e. interface atoms to form interfacial layer), which is beyond the reach of many experimental techniques. However, recent development of numerous experimental techniques along with theoretical calculations made it possible not only to overcome such difficulty but also to bring out new results and understanding, which have never thought of.

1.1   Motivation or driving force

1.1.1   Technological driving force

The digital revolution brought about by the development of ICs over the last half century is one of the most astonishing achievements in human history. Computers, cellular phones and many other information technologies have now become indispensable parts of modern societies. These technologies - modern computers, the internet, telecommunications, as well as modern financial, business, manufacturing, and transportation systems - all depend on the existence of ICs. For all their importance, ICs could have never been achieved without the creative and efficient exploration of thin film materials. Most materials used in advanced microelectronic devices are in thin film form. For example, a single state-of-the-art microprocessor contains hundreds of millions of thin-film transistors that are interconnected by numerous thin metal wires. The continuing miniaturization and increasing complexity of metal interconnects have become the cost, yield, and performance limiter for advanced ICs. Moreover, metal thin films of Au, Ag, Cu, etc. act as contact layers in many systems because of their low resistivity and high electromigration resistance. Low reactivity of these metals with the ambient oxygen facilitates them to apply in practical purposes. Among these metals Au is widely used in electronic devices to control the base minority-carrier lifetime due to its ability to act as a recombination center when dissolved in Si [8]. Hence, the understanding of interface of such metal films with the semiconductor plays an important role. On the other hand, nanolayer of soft materials like Langmuir-Blodgett (LB) films grown on semiconductor substrates have potential applications in variety of fields such as sensors, corrosions, photoresists and in the studies of non-linear optics [9–16]. These ordered arrays of oriented amphiphilic molecules may be useful as insulating or patterning layers in microelectronics [17; 18], as model systems for studies of 2D phases [19] and as molecular templates for protein crystallization [20]. The potential of LB films for these applications is sensitive to the details of their molecular packing; in particular,

they require that the layers have a defect-free, periodic structure [21].

Among the semiconductors, Si is best known for its role in the microelectronics industry, most notably as transistors, precisely because of the way its surface oxide leads to unique electrical properties [22–24]. Almost as important as oxidation, the removal of surface oxide by wet chemical surface passivation technique (described in the section 2.2.3.3) has had a pivotal role not only for the development of the microelectronic industry [25] but also for facilitating the attachment of nanolayers critical for optoelectronic devices, sensors, etc. [9; 10]. Surface passivation has been found to be an absolutely essential process, for example, in the manufacturing of microdisk lasers [26]. For passivation of Si surfaces, two main procedures are used nowadays. First, using ex-situ chemical processing involving the etching of Si samples in aqueous solution of hydrofluoric acid (HF) or alkaline solution of potassium hydroxide (KOH) and/or immersion into a appropriate solution of desired species. By this technique a high quality Si surface passivated with desired species can be created. An alternative preparation method of such passivated Si surfaces is in-situ exposure of the atomically clean Si surfaces to desired atomic species in the ultra-high vacuum (UHV) chamber. The wet-chemical method is very appealing and popular due to its simplicity. Moreover in some cases wet chemically passivated Si surface is more passive against oxygen in comparison with the passivated surface prepared in UHV [27]. Among differently passivated surface H-passivated Si surface is the most stable passivated surface and it is often used as the starting substrate for further processing for biological, energy and microelectronic applications [28]. Additionally, H adsorption at solid surfaces is the initial step for a variety of surface and bulk phenomena such as H storage in materials and hydrogenation reactions. Furthermore, there are few studies exist where authors claimed that the Br-passivated Si surface is more stable than the H-passivated Si surface [29; 30]. This creates renewed interests to understand and/or to verify the nature of such passivated surfaces using novel techniques, which have never attempted for.

1.1.2   Scientific driving force

Apart from the technological driving force, there are strong scientific motivation to study the growth and stability of nanolayers on differently passivated or terminated Si substrates. Si is a typical covalent semiconductor with a large bond energy (2 eV/bond) and consequently its melting point is high ($\sim$ 1400 °C). Growth of nanolayers, specially of hard material like metal, depends on how it reacts with Si. That means, the ability of metals to weaken the Si-Si covalent bonds. In this sense, metals can be subdivided into two main groups, first (e.g. Ag, Al, In, Pb, etc.) which form non-diffusive metal/Si interface and second (e.g. Au, Cu, Ni Fe, Co, etc.) which react with Si substrate to form diffusive interfaces. Diffusive and non-diffusive growth behavior of metal/Si system can be drastically modified by the passivation of Si surface as mentioned before prior to deposition of metal. The interface formation temperature of diffusive metal nanolayers (e.g. Cu) is reduced substantially [29; 31] and the growth mode of the overlayer film of non-diffusive metal (e.g. Ag) changes with the passivation [6].

Contact problem of second group of metals with Si is very crucial. For example, when Si is in contact with metal like Au or Cu it readily reacts with them. Such reaction or diffused zone have been studied extensively after broadening it by applying temperature [29; 32–34]. Broadening of diffused zone is needed in order to make it sensitive for the well known instruments like Rutherford back scattering (RBS) [29; 34], secondary ion mass spectrometry (SIMS) [35], nuclear reaction analysis (NRA) [36], radio tracers techniques [37; 38]. From these studies the diffusion of thick film (few hundred nanometer to micrometer order) in micron length scale and at elevated temperature is well established. However, the questions lie how interfacial modification takes place in ambient condition and how such interfacial modification affects the growth and evolution of the nanolayer. Difficulties in answering such questions, using above mentioned techniques, are their poor depth

resolution[1] and/or destructiveness[2]. X-ray photoelectron spectroscopy (XPS) can however overcome some of these difficulties, which have been used for such study. But due to the limited penetration depth of the photoelectrons (1 - 10 nm depending on their energy) XPS can not probe beyond certain depth without affecting the film structure [39]. To probe further, the top layer has to be eroded by sputtering, which is also a destructive method. Another technique is often use to study the interface is the cross sectional transmission electron microscopy (TEM). However, such technique requires special sample preparation, which is not only a tedious job but also can modify the actual structure of the sample. Most important step for sample preparation is the ion milling, which can modify or induce defect into the interface [40]. For proper understanding of interface, especially in nanolevel, such modification can not be ignored. Additionally, the main interest lies in the understanding the dynamics of the interface or system as a whole, which is beyond the scope of most of the instruments discussed before. It is necessary to mention that, observation of diffused layer and its dynamics with time is essential to calculate the diffusivity and activation energy of the diffusion processes. In this respect, X-ray reflectivity (XRR) [41; 42] is an extremely powerful and non-destructive tool to investigate such behavior. XRR technique essentially provides an electron density profile (EDP), i.e., in-plane $(x-y)$ average electron density (ρ) as a function of depth (z) in high resolution [43]. From EDP it is possible to estimate film thickness, electron density, and interfacial roughness, which in turn can provides information about surface and interface of nanolayer/Si systems in angstrom resolution [35; 41; 42; 44–46] and also information about the evolution of buried layer. XRR combined with surface imaging techniques like scanning probe microscopy (SPM), scanning electron microscopy (SEM), etc. promises better understanding of growth, structure and evolution of nanolayer/Si system and deeper insight into the processes related or responsible to those.

---

[1]RBS has the depth resolution is ~ 100 Å.
[2]SIMS is a destructive technique.

This is also true for nanolayer of soft materials. Structure of soft materials like LB films is strongly related to two main factors: (i) the structure or order of the starting Langmuir monolayer and (ii) the substrate-surface condition where it is transferred. The structure of the Langmuir monolayer can be tuned through the attachment of different number of metal ions by varying pH [47; 48], selection of different metal ions having different type and/or strength of interaction [49; 50] etc. which are well investigated. As the LB film deals with the amphiphilic molecules, which have both hydrophobic and hydrophilic parts, its structure can be modified by changing the nature of the substrate surface. As mentioned before, such modification of surface can be easily done by passivation through wet chemical reaction. Furthermore, growth of self assembled monolayers on the Si surface [49; 51–53] can modify the nature of the substrate surface. This is the well known technique. But in some work [52; 54], the wet chemical passivation technique has been used to modify the growth of LB films. However, not much work has been carried out to investigate the structure and stability of LB films on wet chemically passivated or terminated Si surface. XRR along with SPM can be useful to extract such structural information, which is essential for understanding physics of low dimensional system. Additionally, such structural information is extremely important to know the nature (hydrophilic or hydrophobic) of a particular passivated surface whose nature is not known. Particularly for heterogenous surface where heterogeneity exists in nanometer scale, which is much smaller than the dimension of liquid drop used for contact angle (CA) measurement of the surface. In such case, through CA measurement it is not possible to find out individual heterogeneity, which may be possible by studying the structure of LB film as its growth proceeds via molecule-by-molecule on solid surface.

1.2 Goal of the thesis

In the light of above discussion, the goal of the present thesis is to understand the growth, structure and stability of nanolayer on semiconducting surface by studying

7

the nanolayer/substrate interfacial structure and its dynamics. In particular, to extend our understanding about the interface that control the growth and stability of metal or metal-organic (LB film) nanolayers on chemically modified Si surfaces, especially using novel experimental and analysis techniques, which have never sought of. For example, we are interested to know how wet chemical passivation (e.g. O/OH-, H- and Br-passivation) of the underlying Si substrates can control the out-of-plane diffusion i.e. interdiffusion for diffusive interfaces like Au/Si and Cu/Si, the in-plane diffusion i.e. wetting/dewetting for abrupt interfaces like Ag/Si or even manipulate the structure of the LB film through the hydrophilic-hydrophobic interactions. Understanding the time evolution structure, the role of interface and the deeper insight into the processes behind those, are not only important to take full advantage of the materials and improve device reliability, but also important to expand our knowledge of the process-structure-property relationship, one of the basic tasks in materials science.

1.3 Outline of the thesis

The dissertation is organized in different chapters as follows:

In chapter 1, we have introduced the subject followed by motivation and goal of the thesis.

In chapter 2, a review of nanolayer growth on semiconductor surface, with special emphasis on metal and metal-organic (LB) nanolayers on Si substrate has been presented. Processes, which are responsible for the change in the nature of Si substrate surface, are also discussed.

In chapter 3, we have discussed in details the actual experimental procedure, namely substrate treatment, sample preparation and their characterizations.

In chapter 4, we have presented the time evolution growth of Au nanolayers on differently passivated Si surfaces at room temperature. The formation of unusual Gaussian shaped interdiffused nanolayer is quite evident. The evolution of which

is strongly dependent on the passivating elements, Si surface crystallinity direction and the pressure; and can be understood quantitatively, as discussed in this chapter.

In chapter 5, the growth and evolution of Ag nanolayers on differently passivated Si surfaces have been presented. Sharp interface formed between Ag/Si system, shows interesting evolution with time. Accordingly, wetting to dewetting transition with or without epitaxy has been observed. The origin behind such evolution has been discussed in this chapter.

In chapter 6, the growth and evolution of Cu nanolayers on differently passivated Si surfaces have been presented, which show interdiffusion as well as dewetting. The possible reason behind such behavior is discussed. The interesting part of Cu/Si system is that its intermediate behavior makes it a more general metal/Si system for further theoretical studies, from where one can approach to the two extreme ends (namely interdiffusion that observed for Au/Si system and sharp interface with dewetting that observed for Ag/Si system).

In chapter 7, we have presented the structural study of LB films on three differently passivated Si surfaces and also investigated the long-term stability of the films. From these studies the hydrophilic or hydrophobic nature of the passivated surface and also their stability have been explored. Interesting structures have been observed on the surfaces where hydrophilic and hydrophobic domains coexist. It is clear that ring-shaped structures are formed on such surface to release the hydrophilic/hydrophobic interfacial stress. However, depending upon the metal headgroups (and their interaction with tails) the formation of such nanostructures is similar to that of a collapse or buckling, which is discussed in this chapter.

Finally, the conclusions and impact of this work, as well as the most promising avenues for future are summarized in chapter 8.

Chapter 2

Nanolayer on semiconductor: A review

2.1   Introduction

As the dimensions of electronic devices decrease with increasing packing density, the thickness of material layers decreases continuously and finally becomes nanolayer. Accordingly, understanding of the growth and stability of nanolayer on semiconductor becomes important both from fundamental and practical points of view.

In the growth of heterostructure, where the substrate and the deposited material are different, the parameters like surface energy and the elastic strain due to different lattice constants become important. The lattice mismatch between deposited material and the substrate will produce a strain in the deposited overlayer, affecting the layer morphology and forcing 'metastable artificial' structures. The growing film initially conforms to the substrate geometry adopting a pseudomorphic structure. As the thickness, so does the strain energy, increases the overlayer film eventually can choose several pathways to relieve strain, typically by introduction of misfit dislocations or by surface roughening.

Adsorbed atoms or molecules, which accumulate on the surface, do not necessarily form a single monolayer. Whether or not they do this depends on how much the adsorbate wets the surface. In other words, is the energy gained, as a result of bonding to the surface, is sufficient to overcome the energy required to form a
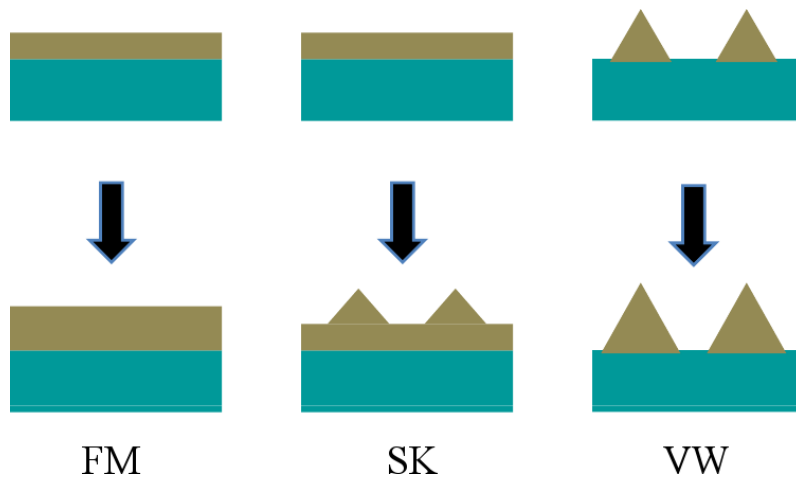
Figure 2.1: Schematic diagrams of the three growth modes for heterostructural systems: Frank-van der Merwe (FM), Stranski-Krastanow (SK), and Volmer-Weber (VW).

large area of adsorbate which is only a single atom or molecule thick? It may be possible that it is energetically more favorable for the adsorbate to form 'clumps', more correctly called 3D islands or crystallites, on the surface. Formally, we can describe the growth of a nanolayer film in terms of three possible models which are shown in Fig. 2.1.

(i) Frank-Van der Merwe (FM) or layer-by-layer growth: This is the ideal growth of a film. The important feature is that as the atoms or molecules are deposited on the surface, they form layers. Each layer is complicated before the next one starts to grow.

(ii) Stranski-Krastanov (SK) or layer-plus-island growth: Here, the initial layers grow in layer-by-layer, but after a certain critical thickness the subsequent layers form islands of deposited material.

(iii) Volmer-Weber (VW) or island growth: In this process, the material immediately lands on the surface, the adsorbates do not wet the surface and so form island or bulk crystallites on the surface from the first monolayer.

One approach to describe the various relevant interactions is to use the concept

of surface and interface energies, γ, similar to what is done for wetting phenomena. Typically, the surface energies (i.e., the relative contributions of the free substrate surface, γ_s, the film surface, γ_f, and the film-substrate interface, γ_i) are then related to the different growth modes mentioned above. In terms of surface and interface energies above three growth modes can be described as below:

$$\gamma_f + \gamma_{in} < \gamma_s \qquad [\text{FM}] \tag{2.1}$$

$$\gamma_f + \gamma_{in} = \gamma_s \qquad [\text{SK}] \tag{2.2}$$

$$\gamma_f + \gamma_{in} > \gamma_s \qquad [\text{VW}] \tag{2.3}$$

It is interesting to turn our attention to the structures of the adsorbate layers which result from the above growth processes. When atoms and molecules adsorb at low coverages there is a tendency for them to form a so-called 'commensurate' structure with the underlying substrate. This means that the overlayer has a (1×1) structure with the substrate acting as a template. The formation of such overlayer films is called epitaxial growth. When adsorbates form a condensed layer, the adsorbate-adsorbate (A-A) and the substrate-adsorbate (S-A) forces control the structure of the layer formed. The A-A forces attempt to impose a structure on the layer which is similar to that of the bulk solid of the adsorbate. This might be very different from the structure of a commensurate layer on the substrate, and strongly depends on which of the two types of forces is strongest. Comparatively strong A-A forces will produce a layer not in registry with the substrate surface, and these are known as an 'incommensurate' layers. Epitaxy occurs when the overlayer material 'distorts' from its bulk lattice to fit in registry with the substrate surface. This is often called 'row matching' and the distortion occurs to cope with the 'misfit' of the two lattices. A useful parameter is the misfit f which is given by

$$f = \frac{(a-b)}{a} \tag{2.4}$$

where a and b are the nearest-neighbor distances of the two contact materials. It has been found that description of surface geometry can be done conveniently using the concept of fractals [55].

Nanolayer of metal-organic, such as LB film, being composed of amphiphilic molecules, its growth is dominated by special type of van der Waal interactions namely, hydrophilic and hydrophobic interactions with the underlying substrate (as described in section 2.4). So the growth of nanolayer is dependent on the surface free energy and hydrophilic-hydrophobic nature of the substrate surface. The surface free energy and hydrophilic-hydrophobic nature of the substrate surface actually depend upon how surface is terminated or passivated.

2.2 Substrate surface

Among different substrates, Si is probably the most studied substrate for its versatile use in device fabrication. In the following we will give brief review of such Si surface.

2.2.1 Si surface: Native oxide

There are many types of oxides that grow on Si, such as thermal oxide, chemical vapor deposition (CVD) oxide, native oxide, anodized oxide. Here we will mainly concentrate on native oxide growth. A surface is normally covered by a very thin ($\sim$ 5-20 Å) oxide layer which is called native oxide. Native oxide layers on Si surfaces prevent the low-temperature growth of high-quality epitaxial Si films and precise control of the thickness and electrical properties of very-thin-gate oxide films, plus give an increase in contact resistance. The control of native oxide growth rate on Si surfaces is of great importance in the fabrication of ultra-large scale integrated devices, especially with a decrease in pattern dimension. Consequently, the understanding of the growth of native oxide layer has received increasing attention [56–61].

Elemental semiconductor such as Si is characterized with purely covalent bonds. Each bond contains two spin-paired electrons. When a surface is created atleast
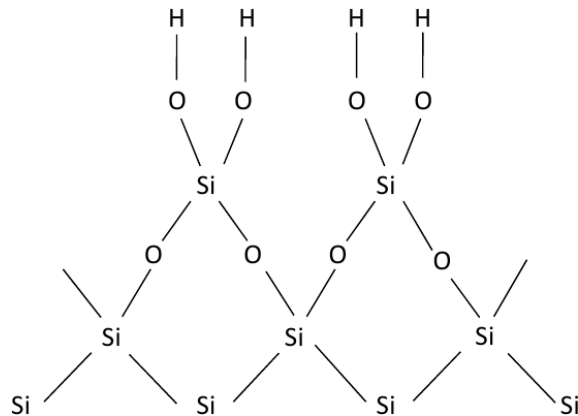
Figure 2.2: Schematic presentation of native oxide on Si surface.

one such bond per atom is cut. A cut bond which is dangle into the environment is called a dangling bond and contains less than two electrons. The lack of electron pairing makes dangling bonds unstable. Thus a cleaved, fresh or clean surface is normally very reactive towards the atoms, molecules or particles, impinging on the surface. In case of Si, highly electronegative oxygen (given in Table 2.1) available in the ambient condition reacts with these bonds to saturate them and to form a very thin (thickness varies from 5-20 Å) native oxide layer as shown in Fig. 2.2. It effectively suppresses the diffusion of metals into Si substrate [29; 31].

Growth of thermal oxides follows different kinetics depending on the thickness of the oxide. Thick SiO_2 films, from about several hundred angstroms upwards, grow according to $linear-parabolic\ kinetics$, where the transport of oxidant through the oxide is the rate limiting step. Below this oxidation regime is a thin oxide regime in which the kinetics is not described by linear-parabolic kinetics but is determined by the interface reactions. This regime can be further divided into two regimes: one from 0 to about 20 Å, representing the native oxide, and the other from 20 Å to several hundred angstroms. While the kinetics of the thick oxide regime is well established, that of the native oxide and thin oxide regimes is not, due to the complexity of the reactions involved at the interface. Thickness or coverage and the growth rate of native oxides strongly depend on surface preparation (i.e., pre-

treatment or in another words surface passivation conditions) and the environmental conditions regarding exposure. It is thus very difficult to prepare a native oxide of certain quality. The transport of oxygen consists of two parts, one related to the interstitial transport of O_2 through the network and the other to a step by step motion of network oxygen atoms. A significant part of oxygen diffusion may be of ionic nature since an electric field is found to affect the growth of oxide.

2.2.1.1   Out-of-plane (thickness) growth

The formation of oxide on a perfectly clean Si surface, e.g., a cleaved surface, is relatively fast, reaching 5-7 Å within a few minutes after exposing to air [58]. The formation of native oxide on the surface after being treated in hydrofluoric acid (HF) solution is much slower. For example, in one case the HF-treated surface is covered with an oxide of 2-3 Å after exposure to air for 1 hour [58]; in another, it takes about 1 week for a monolayer to form [62]. The slow growth of native oxide on the HF-treated surface is attributed to the hydrogen termination which passivates the surface. The formation of the first monolayer of oxide requires the breakup of the Si-H bonds. According to Graf *et al*. [62; 63], the oxide growth on HF-treated Si in air follows two distinct stages. There is an incubation period initially, during which the oxide grows very little. Afterwards, the growth shows a logarithmic dependence on time with a rate of ~ 5 Å/decade. Another study reported similar growth kinetics as shown in Fig. 2.3 [64]. There is very little growth up to about 200 min after which the growth rate increases significantly. The S-shaped curve in Fig. 2.3 is attributed to a layer-by-layer growth of the oxide with 5.4 to 7.6 Å corresponding to two layers of native oxide. The substrate condition plays an important role in the growth of native oxide on Si. The growth rate of native oxide films is similar for lowly and moderately doped Si substrates [58]. An increased growth rate is observed with high dopant concentration $> 10^{19}/cm^3$ on both n- and p-type Si substrates [64].
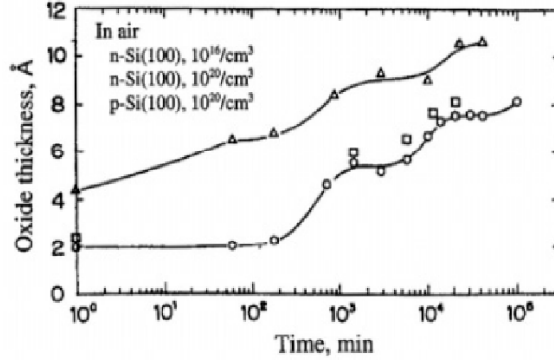
Figure 2.3: Oxide thickness data plotted as a function of the logarithm of the exposure time of the wafers to air at room temperature. This figure has been taken from the paper of Morita *et al.* [64].

2.2.1.2   In-plane (coverage) growth

Very few studies are present regarding the direct in-plane growth of native oxide till date. Those work were involved to the desorption study of passivating elements like F, Br [65] and correspondingly the native oxide growth on the Si surface by using x-ray photoelectron spectroscopy (XPS) technique [66]. The decrease of F and Br coverage with time was correlated with the native oxide growth. The decay function was assumed of the form [65; 66]

$$C(t) = C(0)e^{-k_D t} , \tag{2.5}$$

or,

$$C_{\mathrm{F,Br}}(t) = C_{\mathrm{F,Br}}(0)e^{\left(-\frac{t}{\tau}\right)} , \tag{2.6}$$

where the desorption rate constant $k_D = 1/\tau$, τ is the decay time of coverage. Such decay is the indicative of oxide growth of the form

$$C_{\mathrm{ox}}(t) = C_{\mathrm{ox}}(0)[1 - e^{\left(-\frac{t}{\tau}\right)}] . \tag{2.7}$$

16
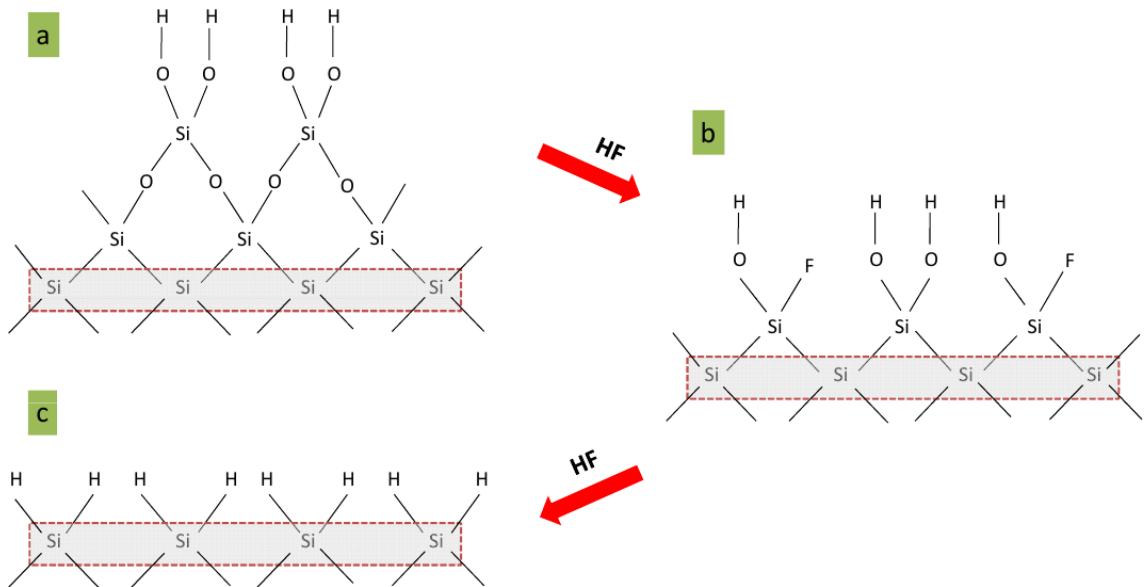
Figure 2.4: Schematic and simplified two-dimensional representation of the oxide removal on Si(001) surface in HF solution which results in a H-passivated Si(001) surface.

2.2.2 Si surface: Etching

Chemical etching is a process for removal of silicon oxides through the dissolution in solutions. It is a key processing step in practically all silicon-based microfabrication technologies. The premier practical application of this process is in the manufacture of ICs, in wafer cleaning, and in pattern delineation. Also etching of silicon oxide as a surface micromachining process is utilized in the fabrication of precision quartz and silicon based micromechanical structures, where chemical etching provides a convenient method for removing undesired surface layers, and for surface micromachining of the desired microstructures [67; 68]. On the other hand, etching of silicon oxide is also important in situations where the oxides are used as the masking material and etching of the oxides can be detrimental. The spatially preferential, or nonplanar etching caused by the effect of doping and crystal orientation, which are widely utilized in device fabrications. Also, the surface roughness resulting from

17
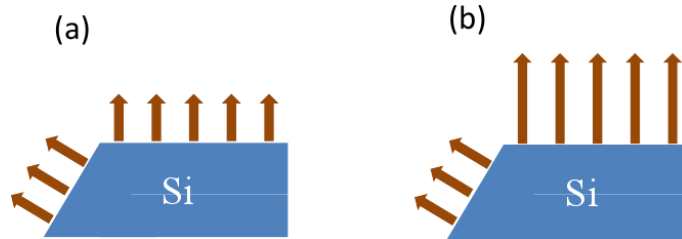
Figure 2.5: Etching of Si surfaces: (a) *isotropic* etching, (b) *anisotropic* etching.

etching, which especially affects all aspects of Si technology.

The two principal etching solution systems for Si are HF solutions and alkaline solutions. This is because Si is inert in aqueous solutions due to the formation of an insoluble surface oxide except for HF solutions or alkaline in which the oxide is soluble. In Fig. 2.4 the oxide removal by HF solution is schematically illustrated. Various chemical agents can be added to these two solutions so as to control the etch rate, etch selectivity, solution stability, and quality of the etched surface. A major difference between these two systems is that the etch rate of Si in HF solution is similar among the various crystalline orientations i.e., it is *isotropic* (shown in Fig. 2.5a), whereas in alkaline solutions it strongly depends on the crystalline orientation i.e., it is *anisotropic* (shown in Fig. 2.5b). The etch rates of the three major crystal planes vary only marginally in HF solutions. The etch rate of Si or its oxides in a given system depends on many operational parameters such as size and geometry of the sample, volume of the solution, stirring condition, ambient (light and air) condition, and etching time. Thus for a given Si material and solution composition, the etch rate may vary significantly when it is measured under different operation conditions. This is responsible for the sometimes large difference in etch rates that can be found in identical systems studied by different investigators.

2.2.3   Si surface: Cleaning

2.2.3.1   Ultrasonic cleaning

Ultrasonic cleaning is used to remove the organic contaminants from the substrate surface. In this cleaning process, substrate is kept into trichloroethylene or acetone (for about 10 min) and methyl alcohol (for about 10 min) solution separately and placed into the ultrasonic bath. It removes organic contaminants only, preserving the native-oxide layer on the surface.

2.2.3.2   RCA cleaning

The RCA (Radio Corporation of America) cleaning process is a standard set of wafer cleaning process which needs to be performed before any application in semiconductor technology. The basic procedure was originally developed by Kern and Puotinen in 1970. It involves the following:

1. Removal of the organic contaminants (Organic clean).
2. Removal of thin oxide layer (Oxide strip).
3. Removal of ionic contamination (Ionic clean).

In the first step which is called SC1 (where SC stands for standard clean), a hot solution (approx. 100 °C) of ammonium hydroxide (NH_4OH, Merck, 30%), hydrogen peroxide (H_2O_2, Merck, 30%) and Milli-Q water (H_2O), with a proportion of $1:1:2$, by volume of chemical agents, is used. SC1 solution is designed to remove organic contaminants by both solvating action of the NH_4OH and the oxidizing action of the H_2O_2. The oxidizing agent H_2O_2 forms a continuous thin silicon oxide layer on the substrate surface. Thus it is very effective in the removal of organic contaminants and as well as in the formation of continuous oxide layer. This cleaning makes the silicon surface completely hydrophilic. Moreover, the metal surface contaminants such as Au, Cu, Ni, Ag, Cd, Zn, Co and Cr are also oxidized by H_2O_2 and dissolved by the complexing effectiveness of the NH_4OH; copper, for example, forms the $Cu(NH_3)_4^{2+}$ amino-complex.

The second treatment step exposes the rinsed wafer to a solution known as SC2, which is a hot mixture of H_2O_2 (30%), HCl (37%), and H_2O in the proportion of $1:1:6$ to $2:1:8$ by volume. This cleaning solution is designed to remove alkali ions and cations such as Al^{3+}, Fe^{3+}, and Mg^{2+} that form NH_4OH-insoluble hydroxides in the alkaline solution.

2.2.4 Si surface: Passivation

Termination of bonds on the semiconductor surface with elements assuring chemical stability of the surface; surface is rendered chemically "passive", such technique is called surface passivation. Surface passivation can be done in two ways, one in ultra high vacuum (UHV) by using selected chemical species in gaseous form or in ambient condition by using wet chemical passivation. The latter one is most easy and popular because of many applications in semiconductor industry. As clean Si surface is very reactive it is impossible to restore a clean surface in ambient conditions. Just after exposing the clean Si surface into the air it readily covered by very thin native oxide. Many schemes for working with Si, especially those operating in ambient conditions, rely on the fact that the high reactivity of the clean surface can be dramatically lowered by saturating the surface with monovalent atoms such as H, Br or Cl. While the cleaved or clean Si surface has very high reactivity due to the presence of "broken bonds" or "dangling bonds" at the surface, exposing the surface to monovalent atoms like H, Br or Cl can produce chemically passivated surface that can be easily handled under ambient conditions. Such surfaces are expected to be unreactive since all surface atoms achieve nearly ideal coordination. But after certain times these surfaces start to react with oxygen in ambient condition.

It should be mentioned here that passivation with different materials and their stability not only depends on the relative electronegativity (δ) and bond-energy (D) with Si, but also on the atomic size (R_a). Values of such parameters, obtained from the online sites [69; 70], which are essential in the description of passivation mechanism, are listed in Table 2.1.

Table 2.1: Relevant parameters, such as the covalent atomic radii (R_a), the electronegativity (δ) in Pauling scale, the bond-energy (D), and the bond-length (L_B) with Si for different elements, as obtained from online sites [69; 70].

Element	R_a [Å]	δ	D [kJ/mol]	L_B [Å]
Si	1.11	1.90	222	2.33
H	0.37	2.20	318	1.48
Br	1.14	2.96	310	2.15
O	0.73	3.44	452	1.63
F	0.71	3.98	565	1.60

2.2.4.1 Hydrogen passivation

In HF solution the oxide layer is removed from the surface and surface is predominantly terminated by hydrogen as shown previously in Fig. 2.4. H-passivated surface has a good resistance to chemical attack and a low surface recombination velocity which indicates a surface with a very low surface-state density.

Since the late 1980s it has been well accepted that such a surface is H-terminated instead of having F^- bonded to the Si atoms. Although the mechanism is not completely understood, it is known that the etching of SiO_2 from a Si surface occurs in two steps: In first step, the oxide layer is rapidly dissolved and forms SiF_6^{2-} ions in HF solution, making the surface temporarily F-terminated. Though the Si-F bond energy (D, given in Table 2.1) is very large but F-termination is not stable. Because in second step, large electronegativity of F polarizes the Si-Si back bonds [71] and anodic dissolution of the last monolayer of oxidized Si (Si^{n+} with $n = 1, 2, 3$) takes place, resulting H-passivated or H-terminated Si surface with dihydride species on the (001) surface and monohydride species on the (111) surface [72; 73] which is schematically illustrated in Fig. 2.6.
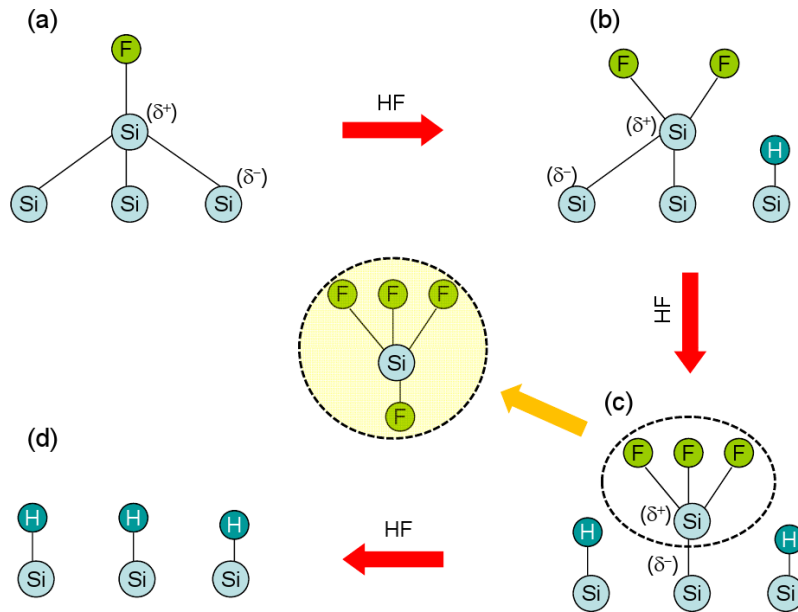
Figure 2.6: Schematic presentation of hydrogen passivation mechanism by HF solution of Si surface.

2.2.4.2 Bromine passivation

In Br-passivation HF-treated Si substrate is immersed into bromine-methanol solution where the concentration of Br is 0.05% by volume and rinse thoroughly [65; 74]. The Br atoms abstract H from the surface via an Eley-Rideal mechanism, producing HBr and leaving behind Si "dangling bonds" that can then react with additional Br radicals to produce Br-terminated surfaces. The replacement is also favored by the fact that Br is more electronegative than H, but it is not favored thermodynamically, as the Si-Br bond dissociation energy is slightly lower than the Si-H energy (listed in Table 2.1). Moreover, Br-passivation is strongly dependent on the crystalline orientation of the substrate surface [75]. The coverage of Br atom and its stability is greater for Si(111) than the Si(001) surface. In Si(111) surface each Si atom has one dangling bond whereas in Si(001) each Si atom has two dangling bond. The size of Br atom, which is large (given in Table 2.1), is the main obstacle in side-by-side accommodation to terminate both the dangling bonds of each Si on Si(001) surface
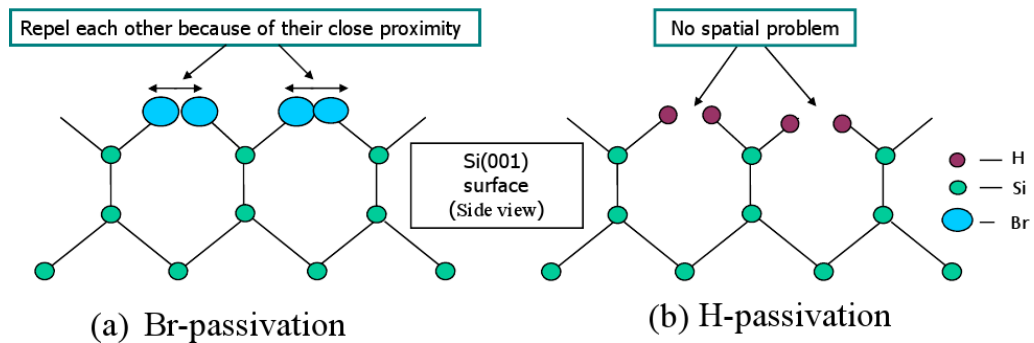
Figure 2.7: Side view of two differently passivated Si surface: (a) Br-passivated and (b) H-passivated surface.

(shown in Fig. 2.7). Such spatial problem does not arise for Si(111). Due to smaller size of H atom (given in Table 2.1), it does not face any problem to passivate both the Si surface i.e., Si(111) and Si(001). Consequently H-passivated surface becomes more stable compared to Br-passivated one.

2.3   Metal/Si

Many phenomena such as interdiffusion and/or interface formation may take place, apart from different growth modes discussed in section 2.1, when metal nanolayers are in contact with Si substrates. In the following we have first discussed some such interface formation mechanism.

2.3.1   Interface formation mechanism

2.3.1.1   Glassy membrane model

This model has been proposed by Walser and Bene [76]. According to this model, in the metal/Si interface there is a mixed phase where Si has no covalent bonding. Si atoms can thus be easily released from this phase for intermixing with the metal. But in their model it is not clear why such a mixed phase is formed. However, this

model is quite helpful for the prediction of the first formed silicide phase by the contact reaction.

2.3.1.2 Interstitial model

According to Tu's "interstitial model" the diffusion of metal atoms into the interstitial sites of Si is responsible for low temperature bond breaking of Si [77]. The occupation of interstitial sites in Si at the interface by metal atoms is an increase of nearest neighbors of the Si atoms which weakens the Si bonds due to charge transfer. If this model is correct, the in-diffused metal atoms must exert stress upon the Si lattice before the breakage of Si bonds at the initial stage. But ion scattering results indicate no presence of such stress at the initial stage [78]. By transmission channeling technique it is observed that Au does not diffuse into the interstitial sites of the Si surface at the initial stage [78]. Rather they migrate freely in <110> direction on Si(100) surface. Their migration continues until the available surface area for the migration is restricted with increasing Au thickness (up to 2 ML). Also the energy loss spectroscopy (ELS), auger electron spectroscopy (AES) and photoemission results by Braicovich *et al.* [79] are inconsistent with Tu's model. Such data indicate the formation of the Si-Au metallic bonding only after Au deposition thicker than the critical thickness. Because Tu's model assumes the formation of metallic bonding between Si atoms and interdiffused interstitial metal atoms from the initial stage, it consequently does not predict a critical Au thickness before the initiation of the Si-Au reaction.

2.3.1.3 Screening model

Hiraki's "screening model" [80] does not find any difficult in consistent explanation of the critical thickness of metal overlayer for intermixing with Si surface. This model postulates electronic screening of Coulomb interaction responsible for covalent bonding of Si crystal due to mobile free electrons in the deposited metal layer. As a consequence of the screening, the bonding character of the Si covalent bond is

largely modified and becomes unstable to facilitate bong breaking. The origin of the critical thickness can be well understood as follows. The film must be thicker than this critical thickness in order to provide for the z-directional freedom of mobile free electrons which is essential for the screening of Coulomb interaction responsible for covalent bonding of lower Si. Moreover, the kinetic energy of the mobile free electron decreases with thickness (d) of the film as d^{-2} due to the "uncertainty principle". Therefore a thinner Au film may more naturally act not as metal but as non-metal. This non-metallic or more atomic like substance then sits on Si surface merely satisfying the surface dangling bonds.

2.3.1.4 Thermodynamic model

Thermodynamic model proposed by Weaver *et al.* [81] suggests that there is a definite correlation between the reaction products observed at metal-semiconductor interfaces and the bulk thermodynamic properties of the constituents. Si and Ge core-level shifts (CLS) has been observed at room temperature for a large variety of metal overlayers such as Ce, Ti, Sc, V, Co, Pd, Au, Pt etc. It strongly suggests an underlying general mechanism which describes phase formation for metal-semiconductor interfaces. The observed behavior for reactive interfaces allows to predict the chemical shifts and to correlate the empirical composition to the spectroscopically observed shift in the semiconductor core level.

2.3.1.5 Cluster model

It is observed that (i) when the thickness of the deposited Au overlayer d<1 ML, Au is dispersed and does not react with the underlying Si substrate, (ii) d≤2 ML, the Au overlayer grows in layer-by-layer fashion i.e., in FM growth mode, (iii) d>2 ML, Au forms clusters and begins to react with Si, (iv) d≤3 ML, Si out diffuses. Following these observations, a "cluster model" has been developed by Lamontagne *et al.* [82] It suggests that the Au overlayer reconstruction at 2 ML promotes the Au-Si interaction and subsequently, the Si outdiffusion. Such reconstruction just

above 2 ML influences the Au-Si interaction in two ways: (i) by providing energy for the reaction at the interface and (ii) by modifying the electronic structure of the Au, promoting the reaction at the interface.

The interface formation mechanism discussed so far also strongly related to the diffusion mechanism which will be discussed below.

2.3.2   Atomic diffusion mechanism

Diffusion can be defined as thermally activated random motion of atoms or molecules in gases, liquids and solids. This type of motion was first observed by Robert Brown in 1827 [83]. The mathematical formulation of Brownian motion was done by Albert Einstein in 1905 and 1906 [84; 85]. Understanding diffusion phenomena in elemental semiconductors is of fundamental interest, since the electrical properties of a semiconductor device can be depend on the thermal stability of a p-n junction or an ohmic contact. Diffusion can also be used as a means to incorporate dopant atoms into a semiconductor.

Diffusion: The redistribution of initially localized substance throughout a background medium due to random thermal motion. The movement of a substance due to diffusion is driven by the slope of the concentration profile. Diffusion of atom may takes place by vacancy, interstitial or a combination mechanism known as interstitialcy as shown in Fig. 2.8.

Vacancy diffusion occurs when a substitutional atom exchanges lattice positions with a vacancy - needs the presence of a vacancy. Interstitial diffusion occurs when an interstitial atom jumps to another interstitial position. It does not require a thermally generated point defect or an direct interchange. Atoms diffusing via the interstitial mechanism are usually very fast diffusers. Interstitialcy diffusion results from Si self-interstitials displacing substitutional impurities to an interstitial position - requires the presence of Si self-interstitials, the impurity interstitial may then knock a Si lattice atom into a self-interstitial position. Note in the interstitialcy
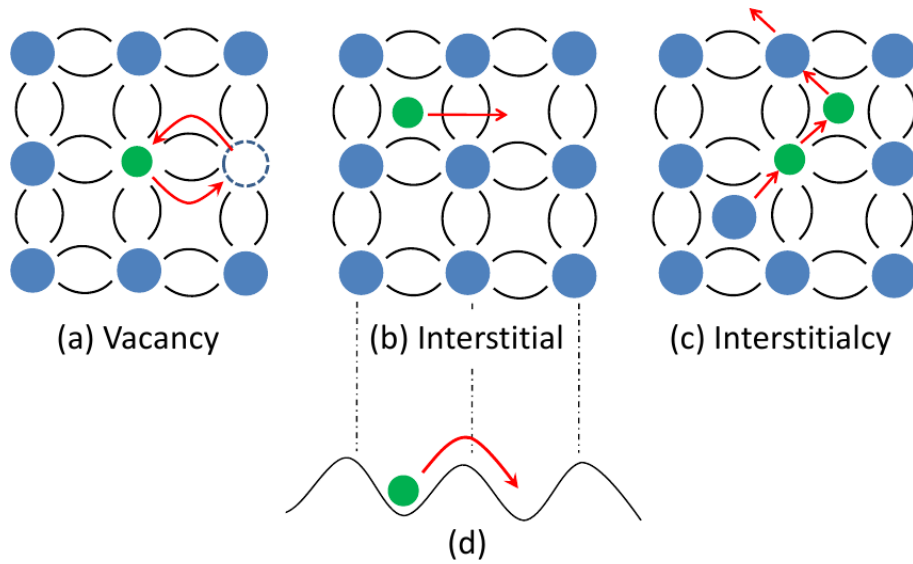
Figure 2.8: (a) Vacancy, (b) interstitial and (c) interstitialcy diffusion mechanisms. (d) Impurity atom diffusing along a periodic potential in a solid crystal.

mechanism, the diffusing atom does not directly jump from one interstitial site to another. Whether an impurity atom occupies a substitutional or interstitial position in single crystal Si, the atom is trapped in a periodic potential defined by the lattice as shown in Fig. 2.8.

A form of interstitial diffusion is also possible for substitutional impurities that are very mobile as interstitials. The impurity atom leaves a lattice site and makes several jumps as an interstitial before jumping back onto a lattice site. Such a mode of diffusion is called a kick-out mechanism [86]. For the kick-out mechanism the impurity interstitial is created by self-interstitials by the reaction:

$$A_S + I \longrightarrow A_I \tag{2.8}$$

where A_I is the impurity interstitial, A_S is the impurity substitutional and I is the self-interstitial. In the Frank-Turnbull, or dissociative mechanism [87] the substitutional impurity atom creates vacancy and an impurity interstitial by the reaction

$$A_S \longrightarrow A_I + V \tag{2.9}$$

where V is a vacancy.

Diffusivity: The diffusivity of a atom in a semiconductor defines the rate of transfer of the atom in the semiconductor under the driving force of a concentration gradient. The diffusion coefficient D, using the statistics of a random walk with a fixed jump distance λ is [88]

$$D = \gamma \lambda^2 \nu \tag{2.10}$$

where ν is the jump rate and γ is a geometric factor accounting for the crystal structure and diffusion mechanism ($\gamma = 1/2$ for the interstitial diffusion mechanism in all diamond structure).

In order to diffuse through Si, the impurity must either move around Si atoms or displace Si atoms. During interstitial diffusion the diffusing atom jumps from one interstitial position to another interstitial position, with relatively low barrier energy and a relatively high number of interstitial sites. Substitutional atoms require the presence of a vacancy or an interstitial to diffuse and must break lattice bonds. Vacancy and interstitial formation are relatively high-energy processes and so are relatively rare in equilibrium. Breaking bonds to the lattice is also a relatively high-energy process and substitutional atoms tend to diffuse at a much lower rate than the interstitial atoms.

The diffusion process can be characterized by a barrier with activation energy E_a, where E_a is the energy required to jump from one site to the next site. The probability of an atom jumping to another site is given by the product of two terms. The first term is the frequency with which the atom collides with the barrier ν_0. The second term is the probability the atom will surmount the barrier during a collision (given by the Boltzman factor $\exp(-E_a/\text{kT})$) where k is the Boltzman's constant and T is the temperature in degrees Kelvin. The rate at which atoms jump to a new position is given by

$$\nu = \nu_0 e^{-E_a/kT} \tag{2.11}$$

Each atom can move to any adjacent site, so Eq. 2.11 should be multiplied by the number of adjacent sites which is 4 for Si for both the interstitial and substitutional case. For the interstitial case Eq. 2.11 becomes

$$\nu_{\text{Inst}} = 4\nu_0 e^{-E_a/kT} \tag{2.12}$$

For substitutional atoms an additional term must be added to account for the probability of a vacancy or interstitial existing in the adjacent site (vacancies for vacancy diffusion and interstitials for interstitialcy diffusion). If E_d is the energy for point defect formation, the resulting expression is

$$\nu_{\text{Subs}} = 4\nu_0 e^{-(E_a+E_d)/kT} \tag{2.13}$$

Experimentally determined activation energy for interstitial atoms are approximately 0.5 eV and for substitutional atoms are approximately 3 eV (including defect formation) [89].

Substituting Eq. 2.12 into Eq. 2.10, the interstitial diffusivity is given by

$$D = 4\gamma\lambda^2\nu_0 e^{-E_a/kT} \tag{2.14}$$

Now taking into account that the spacing between atoms $\lambda = d/\sqrt{3}$ and $\gamma = 1/2$ for a diamond structure like Si, the diffusivity becomes

$$D = \frac{4d^2\nu_0}{6} e^{-E_a/kT} \tag{2.15}$$

Now to cover wide spectrum or general behavior of metal/silicon interface, let us briefly review three systems namely Au/Si, Ag/Si and Cu/Si, which have different interesting behavior.

2.3.3 Au/Si system

The Au/Si interface, which is probably the most studied metal-semiconductor contact [43; 79; 90–100], is a model system for investigating the Schottky-barrier formation as well as the nature of p-d hybridization process [94; 95]. Especially, Au is a

very stable, nonreactive noble metal, and yet it has been reported to be very reactive with complex behavior on a Si surface even when deposited at room temperature. The most important fact is that the melting points of Au and Si are 1063 °C and 1414 °C, respectively, while the melting point of a mixture of both at the eutectic composition is 363 °C. This deep depression has been used for over 40 years to attach a chip to its substrates. A variety of experimental methods has been applied to obtain complementary information on electronic and structural properties of Au/Si interface [91–93]. It is found that Au reacts with Si surface to form interfacial layer even at room-temperature [101] and ultra-high vacuum (UHV) condition [79], in contrary to Ag which forms a rather abrupt interface with Si. Although the thickness where the interfacial layer formed has some controversy [79; 90–100], following junction structure from the Si substrate is well accepted at least for the thicker-layer case: A diffuse and alloyed zone (about 2 nm thick); an intermediate region where only Au is detected and a thin (about 1-2 ML) superficial phase on top of the Au region [92; 94]. It is known that most of the semiconductors readily reacting with the metals are classified as covalent semiconductors with fairly large bond energy. Consequently, the above interfacial reaction may hardly occur without the presence of such an effect of metal as to induce instability in covalent bonding (or cohesive character) of the semiconductor adjacent to the metal. The possible cause of the instability (say in Si) is the ability of metal (say Au) to screen Coulomb interaction due to its mobile free electrons [92]. Such interface formation takes place through the diffusion of Au atoms into Si substrates. The diffusion of Au into Si was first studied in detail by Struthers using radiotracers [37; 38]. Diffusion of Au into Si has been extensively investigated at elevated temperature (700 °C - 1300 °C). The activation energy measured for different diffusion mechanism of Au into Si in the temperature range of 700 °C to 1300 °C. For interstitial and substitutional diffusions the activation energies are 0.39 eV and 2.04 eV, respectively [102].

2.3.4   Ag/Si system

Among the three noble metals such as Au, Ag and Cu, Ag is less reactive with the Si surface. It shows much less alloying tendency than Au and Cu when deposited on the Si surface. The eutectic temperature is around 830 °C which is relatively higher than the Au-Si and Cu-Si eutectic temperatures. Amorphous Ag-Si alloys can hardly be grown by fast quenching from the liquid phase. The Ag/Si interface is generally considered as a good example of abrupt metal/silicon junction characterized by the absence of pronounced interdiffusion between the two atomic species. The absence of strong Ag-Si interactions makes other parameters, such as Si surface conditions, mode of preparation, cleanliness, defect density, etc., highly sensitive to the growth of Ag. In general, there are three known thin film growth modes: layer-by-layer [Frank-van der Merwe (FM)], island [Volmer-Weber (VW)] and layer-plus-island [Stranski-Krastanov (SK)] growth modes [103; 104], as mentioned before. Which growth mode will be adopted in a given system will depends upon the surface free-energy terms and on the lattice mismatch. A great deal of effort has been devoted in controlling and/or altering the film growth using foreign species or 'surfactants' [6]. Introduction of a foreign atomic layer (of hydrogen, bromine, etc.) in place of clean or oxide layer, on substrate surface [7; 95; 105–111] can change its surface energy and/or roughness, which can alter the growth mode and morphology of a overlayer.

The effects of deposition conditions on the morphology of thin Ag films on Si have been investigated extensively in recent decades. Ag is found to grow epitaxially on both Si(001) and Si(111) through coincident site lattice matching, though there is a large (25%) lattice mismatch [112–116]. Epitaxial Ag films have been obtained mostly by molecular beam epitaxy (MBE) process, where the energy of depositing particles is relatively low. While, using magnetron sputtering process, Ag films usually obtained are non-epitaxial, although having <111> as preferred growth orientation [117; 118]. However, in few works, epitaxial growth of Ag on native oxide covered Si(100) has been observed by magnetron sputtering process at higher temperatures [119; 120]. Epitaxial growth of Ag on H-passivated and Br-passivated

Si(111) substrates has been observed above room temperature (RT) [36; 121–126].

2.3.5 Cu/Si system

During the last decade, an intense research has been led on the comprehension of the solid-state reaction of Cu layers with Si [127; 128] and silicides [129]. Though Cu is a key component of such interconnects, interdiffusion of Cu from the surface into the bulk of the silicon chip can adversely affect device performance [130]. It has been studied in the past years [131] and broad tendencies have been outlined. The reactions are fast and start at the temperatures much lower than the lowest eutectic temperature in the phase diagram. The second important property, which dominates the Cu-Si metallurgy, lies in the fact that Cu is among the fastest diffusers in silicon. It is generally believed that it diffuses by the interstitial-substitutional mechanism or the kick-out mechanism [132; 133], with a pre-exponential factor of 4×10^2 cm²/s and an activation energy as low as 1.0 eV. The Cu/Si system shows intermediate alloying tendency of Au/Si and Ag/Si systems. The interfacial reaction between Cu layer and clean Si or H-passivated Si takes place at lower temperature (150 °C) than when the Si substrate is covered with a native oxide layer (600 °C) of about 15 Å of thickness [134]. So, one can easily say that a very thin layer of native silicon oxide can play the role of diffusion barrier efficiently and delays the reaction therefore at the Cu/Si interface. It was reported that the Cu₃Si phase grows at 170 °C on amorphous Si, at 200 °C on monocrystalline Si and after annealing at 600 °C on oxidized substrate [29; 135]. The growth of this phase is in agreement with thermodynamics data and the prediction of Walser and Bene law [76] which is mentioned in section 2.3.1.

It is clear from the review of metal/Si system that most of the investigations have been carried out at elevated temperatures and not much studies have been made at room temperature by varying the foreign atomic layer (such as H, Br etc.) at the interfaces. Moreover, in our knowledge there is no literature studying the long-term
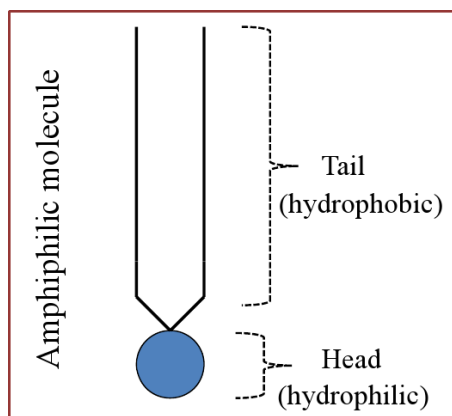
Figure 2.9: A schematic diagram of a amphiphilic molecule of two hydrocarbon tails.

stability or instability induced evolution of such films, which is of prime importance, as will be evident from our studies, presented in chapters 4, 5 and 6.

2.4 LB film/Si

The term Langmuir-Blodgett (LB) comes from the names of research scientists, Irving Langmuir and Katherine Blodgett, who discovered unique properties of thin films in early 1900s. Monomolecular insoluble layer float on the surface of liquid, known as Langmuir monolayer, is most commonly formed on the surface of water by molecules called lipids or amphiphiles, which consist of two dissimilar parts as clearly shown in Fig. 2.9. One part is hydrophilic (polar) which is referred to as the 'head' and the rest part is hydrophobic (non-polar) which is referred to as the 'tail'. By transferring monolayers of organic material from a liquid to a solid substrate, the structure of the film, known as LB film, can be controlled at the molecular level.

LB films are ideal for testing basic physics of low-dimensional systems, viz. electrical transport, magnetism, and melting in two-dimensional (2D) systems [136–138], specific growth mechanism arising from different types of observed in-plane correlations[139–142], etc. These films also show unique properties and have promising applications in the field of biosensors, catalysis, nonlinear optics, microelectron-

ics, and nanotechnology [9–16]. Such films exhibit various electrochemical and pho-
tochemical properties. This has led some researchers to pursue LB films as a possible
structure for ICs and sensing applications. Ultimately, it might be possible to con-
struct an LB-film memory chip in which each data bit is represented by a single
molecule. Complex switching networks might be fabricated onto multilayer LB-film
chip. However, physical properties of LB films strongly depend on their structure.
Defects [49], imperfection [51], and instabilities [143] in the structure are the main
obstacles behind their proper applications. Defects, which are mainly observed in
the LB films, are the 'pinhole' type defects [140; 144] and can partially be removed
by increasing pH [47; 48] of or by dissolving different metal ions [49] in the water
subphase.

Dutta *et al.* [145] have shown that the 'high pH' (> 8.5) monolayer phase of
cadmium arachidate (CdA) has more condensed and lower energy lattice structure
than that of 'normal pH' (~ 7) phase. By using imaging technique, Schwartz *et
al.* [47] have shown that the defects in the LB film can be removed substantially
by increasing pH from 7 to 8.5. Kundu *et al.* [48] have shown that the metal ion
incorporation into the head of LB film can be increased by increasing pH, which is
mainly responsible for the structural quality of the LB film. They have shown that
'high pH' (~ 9.0) LB film has very few pinhole type defects compared to that of
the 'normal pH' (~ 6.5) film. Moreover, Schwartz *et al.* [146] also have shown that
Langmuir monolayer is more ordered in presence of Pd, Cd ions rather than Ba. This
effect was explained by varying degree of ionic or covalent bonding: strong covalent
for Pd, Cd and weak ionic for Ba. These stronger metal ion-ligand interactions in
Pb salts likely help hold the monolayer together despite the large mismatch between
the fatty acid lattice and the substrate lattice. Different substrates have also been
used to understand the substrate effects in controlling LB structure [49; 143; 147–
149]. Spink [150] compared the transfer ratio (TR) of LB monolayers inferred by
the decrease in area of the trough to the actual amount of material transferred by
measuring the radioactivity of monolayers prepared from ^{14}C-labeled stearic acid.
He deposited monolayers on mica, silicon oxide, glass, Ag, Cu, Pt, and Fe and

found that in the range pH = 2 to 6, for $10 \leq \pi \leq 30$ mN/m, and for deposition speeds ranging from 2.5 to 12.5 mm/min, the TR was effectively unity. Recognizing that the attraction or 'reactivity' between the monolayer and substrate must vary dramatically over the variety of substrates used, he hypothesized that the monolayer must deposit onto the solid 'as a carpet' resulting in a TR of unity. If the monolayer is not strongly 'bonded' to the surface, he concluded, rearrangement may take place after deposition. He performed electron microscopy studies on replicas of LB films to observe this rearrangement. Zasadzinski *et al.* [151] also have shown that for a particular pH the morphology of the LB film strongly depends on different types of substrate surfaces. They have compared the structure of CdA at pH $\sim$ 5.5 on Si and mica substrate. It has been observed that LB film is uniform i.e. hole free on Si substrate whereas on mica holes of 10-100 nm in diameter are present. These differences in film quality were ascribed to the less extensive hydration of the mica at pH $\sim$ 5.5.

It is well known that substrate surface condition for a particular substrate plays important role in the growth and stability of any nanolayer on it [143]. Substrate surface condition can be modified through different ways; by passivating with foreign atomic layer (such as H, Br, Cl, etc.) or by growing self-assembled monolayer (of say silane). This essentially modifies the surface free energy or polarity of the surface and accordingly, wetting-dewetting or hydrophilic-hydrophobic nature of the surface can be tuned [72; 73; 152–154]. To modify the substrate particularly to become a hydrophobic surface prior to LB depostion scientist mainly are used to deposit a self-assembled monolayer (of say silane) on the substrate surface [51; 53] except few studies, where they have followed the wet chemical technique to make a surface hydrophobic [49; 52]. Hazra *et al.* [51] and Mukhopadhyay *et al.* [53] have deposited octadecyltrichlorosilane (OTS) in order to make the Si substrate hydrophobic before LB film deposition. Schwartz *et al.* [54] have done HF treatment to prepare a hydrophobic Si surface.

From the review of LB film/Si system it is not clear how different treatment or passivation of Si surface and their stability affect both in-plane and out-of-

plane structure of the LB film. Also how that structure modified for LB film containing different metal ions as headgroups. These are particularly important not only to get well order and stable 2D structure but also to get interesting ring-shaped nanostructures, as will be evident in chapter 7. Moreover, the LB technique has not been used before as a tool to explore the hydrophilic-hydrophobic (polar-nonpolar) nature of a surface. It is well accepted that the wetting/nonwetting i.e., hydrophilic/hydrophobic nature of a surface is better understood by contact angle (CA) measurement [155; 156], which is quite useful if the surface is homogeneous in macroscopic dimensions. However, if the surface is inhomogeneous, that is both hydrophobic and hydrophilic domains coexisted and the domain or spot size is of the order of nanometer then through conventional CA measurements it is only possible to estimate overall nature of the substrate surface and not the nature of individual spots. Such limitation of CA can be overcome by depositing LB film and determining its structure. This is shown in chaper 7, from which the nature of the substrate surface have be determined in the molecular level.

Chapter 3

Experimental details

In this chapter we will discuss in details about the sample preparation and their charaterization.

3.1 Sample preparation

Sample preparation consists of two parts: first the substrate preparation and then the nanolayer deposition.

3.1.1 Substrate preparation

Substrate preparation essentially means the preparation of the surface of Si substrate. Depending upon the treatment procedure, as discussed in details in the previous chapter, one can get differently terminated or passivated Si substrate. In the following we will discuss briefly the preparation procedure for four different types of passivated or terminated Si substrates (X-Si, where X = O, OH, H and Br), which are of our interest.

3.1.1.1 O-Si substrates

The Si substrates were cleaned in an ultrasonic bath, first using trichloroethylene solution for about 10 min and then using methyl alcohol solution for another 10 min

to remove the organic contaminants present in the substrate surface. Such substrates are labeled as O-Si, as native oxide layer is preserved in such cleaning or treatment procedure.

3.1.1.2 OH-Si substrates

The Si substrates were subjected to RCA cleaning procedure. For that, we have used SC1 solution i.e., a hot solution (approx. 100°C) of ammonium hydroxide (NH_4OH, Merck, 30%), hydrogen peroxide (H_2O_2, Merck, 30%) and Milli-Q water (H_2O), with a proportion of 1 : 1 : 2, by volume. Si substrates were kept into this hot solution for 5-10 mins. Such substrates are labeled as OH-Si, as freshly prepared oxides are terminated with OH groups.

3.1.1.3 H-Si substrates

The Si substrates were treated with HF solution after ultrasonic cleaning. It is well known that the etching of Si substrate strongly depends on the concentration of HF solution and the time of immersion into it. Here we have used 10% HF solution and 3 mins immersion time, which provides best surface, namely almost oxide-free surface with low roughness. Such substrates are labeled as H-Si, as HF treatment produce H-passivated surface after removing oxide layer.

3.1.1.4 Br-Si substrates

The Si substrates after removing oxide layer with HF solution, were further subjected to bromine-methanol solution (Br concentration is 0.05% by volume) and rinse thoroughly for 20 min. Such Br-passivated Si substrates are labeled as Br-Si.

3.1.2 Nanolayer deposition

Metal and metal-orgalic nanolayers were deposited on pretreated Si substrates using magnetron sputtering and Langmuir-Blodgett techniques, respectively. The working

principle and the instrumental specification of these two techniques are discussed first followed by actual deposition.

3.1.2.1   Magnetron sputtering technique

A. Working principle:

In 1935 Penning first studied low pressure sputtering in which a traverse magnetic field was superposed on a dc glow discharge tube. The basic sputtering process, in which materials are evaporated from the solid state by bombarding their surfaces with energetic ions, has been known and used for many years [157]. Although many materials have been successfully deposited by this process, it is limited by low deposition rates, low ionisation efficiency in the plasma, and high substrate heating effects. These limitations have been overcome by the introduction of magnetron sputtering. The magnetron sputtering is a very simple and reliable process which is used from several years for industrial deposition of thin films and coatings [157–159]. Magnetron sputtering has emerged to complement other vacuum coating techniques such as thermal evaporation and electron-beam evaporation. However these techniques show certain disadvantages. In particular, alloys and refractory metals cause problems because of differences in alloy constituent vapour pressures and their high melting points (the need to run sources very hot thereby affecting your coated articles). In addition compounds can dissociate into their chemical constituents at the low evaporation pressures used. Magnetron sputtering overcomes these problems and has many other advantages. The primary advantages are (1) high deposition rates, (2) ease of sputtering any metal, alloy or compound, (3) high-purity films, (4) extremely high adhesion of films, (5) excellent coverage of steps and small features, (6) ability to coat heat-sensitive substrates, (7) ease of automation, and (8) excellent uniformity on large-area substrates, e.g. architectural glass. These points will be discussed later but it is immediately clear that sputtering is a very powerful technique which can be used in a wide range of applications.

The schematic view of magnetron sputtering principle is shown in Fig. 3.1. Within the sputtering process gas ions out of a plasma are accelerated towards a
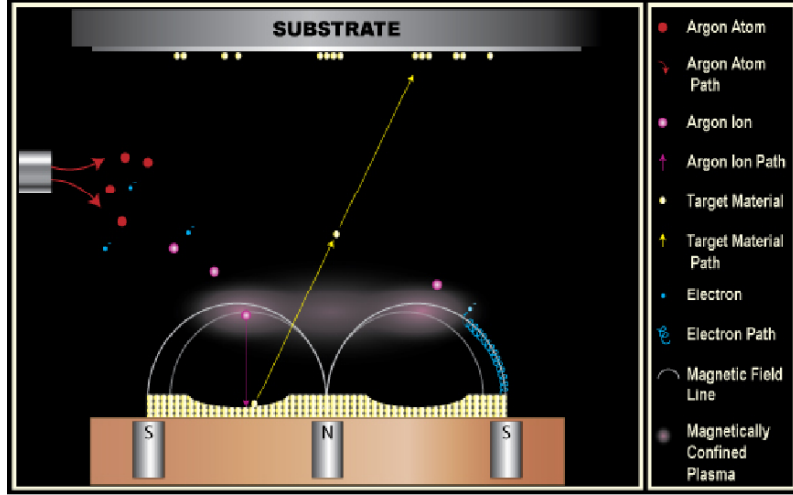
Figure 3.1: Schematic view of magnetron sputtering technique.

target consisting of the material to be deposited. Material is detached ('sputtered') from the target and afterwards deposited on a substrate in the vicinity. The process is realized in a closed recipient, which is pumped down to a vacuum base pressure before deposition starts. To enable the ignition of a plasma usually argon is feed into the chamber up to a pressure between 0 to 12 Pa. By natural cosmic radiation there are always some ionized Ar^+-ions available. In the dc-sputtering a negative potential U up to some hundred volts is applied to the target. As a result, the Ar^+-ions are accelerated towards the target and set material free, on the other hand they produce secondary electrons. These electrons cause a further ionization of the gas. The gas pressure p and the electrode distance d determine a break-through voltage U_D from which on a self sustaining glow discharge starts- following the equation

$$U_D \quad = \quad A\frac{pd}{\ln(pd) + B} \qquad (3.1)$$

with materials constants A and B. This is called Paschen's Law [160], named after Friedrich Paschen. Graphically spoken the ionization probability rises with an increase in pressure and hence the number of ions and the conductivity of the gas also increase. The break through voltage drops. For a sufficient ionization rate a

stable burning plasma results, wherefrom a sufficient amount of ions is available for sputtering of the material.

To increase the ionization rate by emitted secondary electrons even further, a ring magnet below the target is used in the magnetron sputtering. The electrons in its field are trapped in cycloids and circulate over the targets surface. By the longer dwell time in the gas they cause a higher ionization probability and hence form a plasma ignition at pressures, which can be up to one hundred times smaller than for conventional sputtering. On the one hand higher deposition rates can be realized thereby. On the other hand less collisions occur for the sputtered material on the way to the substrate because of the lower pressure and hence the kinetic energy at the impact on the substrate is higher. The electron density and hence the number of generated ions is highest, where the magnetic field is parallel to the substrate surface. The highest sputter yield happens on the target area right below this region. An erosion zone is formed which follows the form of the magnetic field.

The bombardment of a non-conducting target with positive ions would lead to a charging of the surface and subsequently to a shielding of the electrical field. The ion current would die off. Therefore the dc-sputtering is restricted to conducting materials like metals or doped semiconductors. There are now two ways to produce dielectric films: In rf-sputtering (radio frequency) an ac-voltage is applied to the target. In one phase ions are accelerated towards the target surface and sputter material. In the other phase charge neutrality is achieved. Hereby also sputtering of non-conducting materials is possible. However, the quality of the deposited film depends upon the plasma gas pressure, the potential applied, substrate-to-target distance, substrate temperature, etc [161; 162]. Another factor that plays a significant role in the film growth is reflected plasma gas atoms from the target [163; 164]. These hyperthermal atoms reach the film surface and transfer their energy to the growing surface of the film, thereby affecting its structure, crystallinity, composition, etc.

Figure 3.2: Picture of Magnetron sputtering instrument (PLS 500) shown in left side. Inside view of the deposition chamber shown in right side.

B. Instrument:

The instrument used to grow metal nanolayers is a magnetron sputtering unit (PLS 500, Pfeiffer Vacuum) shown in Fig. 3.2. The main chamber, shown in Fig. 3.2, can be evacuated to a base pressure of $\sim 1 \times 10^{-6}$ mbar with the help of a turbo-molecular pump (Pfeiffer, TMH 520) backed by a rotary pump (Pfeiffer, DUO 016 B). Different types of gases like argon, nitrogen, etc. can be introduced into the main chamber for plasma discharge. The gas flow rate is controlled by a mass flow controller (MKS Instruments, 647B). The instrument is equipped with two dc and one rf sputtering units which can be operated at different wattage. The maximum power that can be applied to the dc magnetron is 0.5 kW. The diameter of each target used in the present set-up is 2 inch. Apart from the static mode, rotation mode of the sample stage is also present. This is useful to get smooth films of uniform thickness while depositing at higher wattage and gas flow rates. In our study, as we kept at least three samples into the deposition chamber in each set of sample preparation, we have used the rotation mode to get smooth films of uniform thickness for all samples belonging to each set of sample preparation. The instrument is

also equipped with a glow discharge facility for cleaning the substrate surface prior to film deposition.

C. Deposited samples

Au, Ag and Cu nanolayers were deposited on differently passivated Si substrates (each of about 10×10 mm^2 size, n-type, resistivity 5-10 Ω-cm) mainly using PLS 500 unit at 3.5×10^{-3} mbar argon pressure and at 25 W power, and also occasionally using another sputtering unit (T4065, KVS) at 2.7×10^{-2} mbar argon pressure and at 9 W power.

I. Au/X-Si samples

Au nanolayers of thickness about 8.5 nm were first deposited simultaneously on three differently treated Si(001) substrates i.e., on O-Si(001), H-Si(001) and Br-Si(001) for 2 min using Au as target material in PLS 500 unit, which are labeled as Au/O-Si(001), Au/H-Si(001), and Au/Br-Si(001), respectively. Similar deposition were also carried out on three differently treated Si(111) substrates and are labeled as Au/O-Si(111), Au/H-Si(111), and Au/Br-Si(111), respectively.

Au nanolayers of different thickness have been deposited on H-Si(001) substrates in bith the units. Samples designated as S1 and S2, prepared together initially have thickness about 4 nm. For checking the reproducibility, samples designated as S3 and S4 of same thickness have been prepared again. To see the effect of thickness, samples designated as S5 and S6 of thickness about 9 and 13 nm, respectively, have been prepared (which also have high coverage compared to samples S1-S4). Lastly, samples designated as S7 and S8 of thickness about 4 nm have been prepared for keeping those samples at nitrogen atmosphere.

II. Ag/X-Si samples

Ag nanolayers of thickness about 11 nm were deposited on three differently treated Si(001) substrates i.e., on O-Si(001), H-Si(001) and Br-Si(001) substrates for 2 minutes, using Ag as target material in PLS 500 unit. Ag deposited nanolayers on these

three types of pretreated substrates are designated as Ag/O-Si(001), Ag/H-Si(001) and Ag/Br-Si(001), respectively.

III. Cu/X-Si samples

Cu nanolayers of thickness about 18 nm were deposited on three differently treated Si(001) substrates i.e., on O-Si(001), H-Si(001) and Br-Si(001) substrates using for 8 minutes using Cu as target material in T4065 unit. Cu deposited nanolayers on three pretreated substrates are designated as Cu/O-Si(001), Cu/H-Si(001) and Cu/Br-Si(001), respectively.

3.1.2.2 Langmuir-Blodgett (LB) technique

A. Working principle:

In order to form a Langmuir film it is necessary for a substance to be insoluble in water and its molecules to have a hydrophilic region which will preferentially reside on the water surface. A long chain carboxylic acid is an ideal example of such a substance. The long hydrocarbon 'tail' is hydrophobic and the acid head group, -COOH, is, even if un-ionized, hydrophilic. Moreover, in a Langmuir monolayer a known number of amphiphilic molecules is placed on the surface of an aqueous subphase; a measured volume of a dilute solution is deposited drop by drop. The monolayer spreads spontaneously onto the clean water surface and dissolved in a volatile organic solvent, e.g. chloroform, methanol, or benzene. Clearly different solvents are used for different materials but a common requirement is that the solvent should be poorly miscible with water as otherwise it will tend to render the amphiphilic material partially soluble. The speed at which the solvent evaporates is also important as too rapid: an evaporation can lead to defects in the film. For convenience and cleanliness, the subphase is generally contained in a Teflon container, known as a trough. In addition to possible temperature control, troughs are capable of two important operations: (1) variation of the fraction of the water surface accessible to the monolayer and (2) measurement of the surface tension (or

surface pressure). One or more movable (typically motorized) Teflon barriers placed across the trough serve to vary the area of the monolayer. Since the number of molecules added to the surface is known, the monolayer area is generally expressed as area/molecule. Measurement of the force exerted on a hydrophilic plate (made, e.g. of filter paper) passing through the water/air interface (a Wilhelmy plate) is the most common method of determining the surface tension (γ). The force measurement is made using an electrobalance or a sensitive spring with a position sensor. The surface pressure (π) is then calculated as

$$\pi \;=\; \gamma_0 - \gamma \tag{3.2}$$

where γ_0 is the surface tension of the pure liquid and γ is the surface tension of the film-covered surface.

To form a film on water surface, amphiphilic molecules are dissolved in some solvent and then the solution is spread on water. It is desirable that the solvent should be capable of dispersing the molecules of the film-forming material at the air-water interface and then evaporate completely so that the film is not contaminated. Usually, the spreading solvent chosen has lower surface tension than water, is volatile, i.e., evaporate within a reasonably short time within which the solution has covered the water surface. The solvent has also to be lighter than water and insoluble in water. If a drop of liquid (1) is placed on a solid or another liquid (2), the extent to which it spreads is given by Young's equation

$$\gamma_{1V} \cos\theta \;=\; \gamma_{2V} - \gamma_{12} \tag{3.3}$$

where the γ's are the interfacial tensions at the various interfaces between the substrate or subphase (2), liquid (1) and vapor (V) phases and θ is the contact angle between the 1 and 2 at the 1-2-V interface. For complete wetting there is no finite contact angle, i.e., the liquid spreads completely on the substrate or subphase.

A quantity called the spreading coefficient can then be defined as

$$S_{1/2} \;=\; \gamma_1 - \gamma_2 - \gamma_{12} \tag{3.4}$$
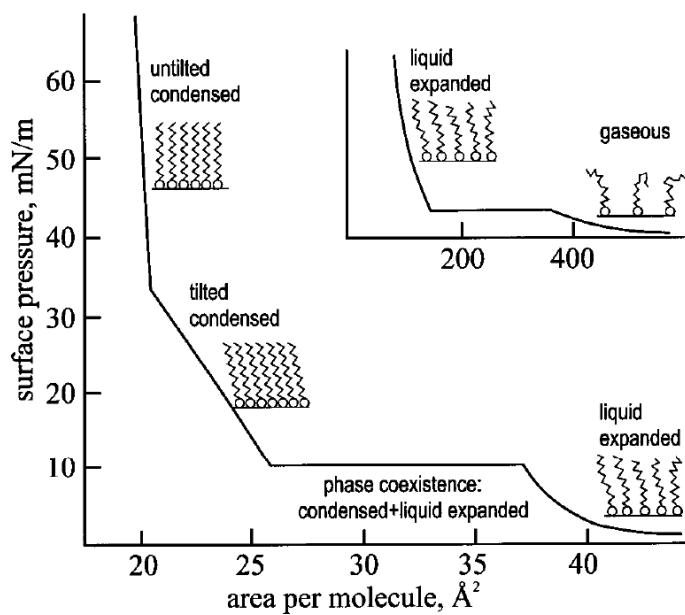
Figure 3.3: A schematic diagram of a generalized isotherm of a Langmuir mono-layer. Horizontal sections of the isotherm are phase coexistence regions at firstorder transitions, and the kink indicates a continuous transition.
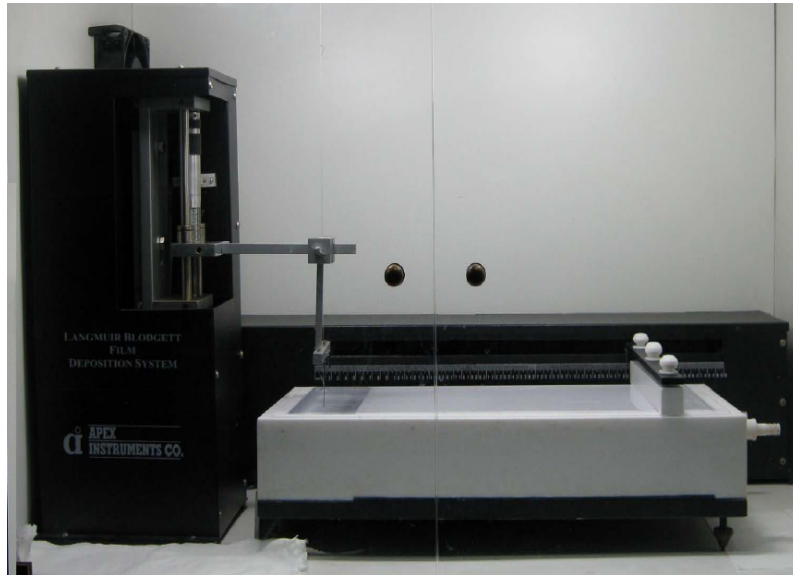
Figure 3.4: Picture of Langmuir-Blodgett film deposition instrument (Apex Instruments).

where $S_{1/2}$ is the spreading coefficient for liquid 1 on liquid 2, γ_1 and γ_2 are the respective surface tensions, and γ_{12} is the interfacial tension. If the value of $S_{1/2}$ is positive, spreading will occur, while if it is negative, 1 will dewet and hence rest as a lens on 2. Comparison of Eq. 3.2 and 3.4 gives that

$$\pi \;=\; \gamma_{0f} - S_{f/0} \qquad\qquad (3.5)$$

i.e., surface pressure of the film on water (π) is the difference between the interfacial tension of the film cover surface (γ_{0f}) and the spreading coefficient of the film on water ($S_{f/0}$).

The spreading solution is used dropwise on different parts of the surface from some micro syringe containing a desired amount of the solution and then some time is allowed for the complete evaporation of the solvent. The amount of solvent spread decides the initial average area available to each molecule in the monolayer. If M_0 is the molecular weight of the amphiphile, ρ is the concentration of the amphiphilic solution in gram/c.c., V is the volume of the solution spread in c.c. and the to-

47

tal surface area covered by the monolayer is S cm^2, then the area per molecule is $A = SM_0/\rho V N_a$ cm^2. Hence the concentration and volume of solution spread is chosen so that the area per molecule is large enough for the monolayer to be in the 'gas' phase.

The most important and basic information about a monolayer is its surface pressure (π) - specific molecular area (A) isotherm. Fig. 3.3 shows the schematic of a typical $\pi - A$ isotherm for a Langmuir monolayer. The very dilute monolayer, with an area per molecule in the range of hundreds of square angstroms, is well described as a two-dimensional gas. With decreasing area per molecule (increasing surface pressure), the monolayer proceeds into what has traditionally been called the liquid expanded phase. Further compression of the monolayer gives rise to a transition from liquid expanded to a condensed phase, with (usually) a plateau indicating a first-order transition. The monolayer is less compressible in the condensed state than in the liquid expanded state. Upon further compression one typically observes a kink on the isotherm, with the compressibility decreasing further after the kink. The two regions of the isotherm possessing different compressibilities are frequently referred to as "liquid condensed" and "solid" states. The hydrocarbon chains of the molecules are aligned parallel to each other in both sections of the isotherm; the difference is in the orientation of the chains, which are either tilted with respect to the water surface or perpendicular to it. The monolayer is relatively easily compressible in the tilted state, where decrease of the surface area can be achieved by decreasing the tilt angle. In the untitled state, the distance between close-packed vertical molecules determines the areal density, and so such phases are much less compressible.

In LB deposition, a layer is deposited during each pass, but the molecules deposited on the upward pass have their polar headgroups oriented towards the substrate (shown in Fig. 3.5a) while the molecules deposited on the downward pass are oriented with the hydrophobic tails towards the substrate (shown in Fig. 3.5b). The result is that the headgroups adhere to the headgroups of the previous layer
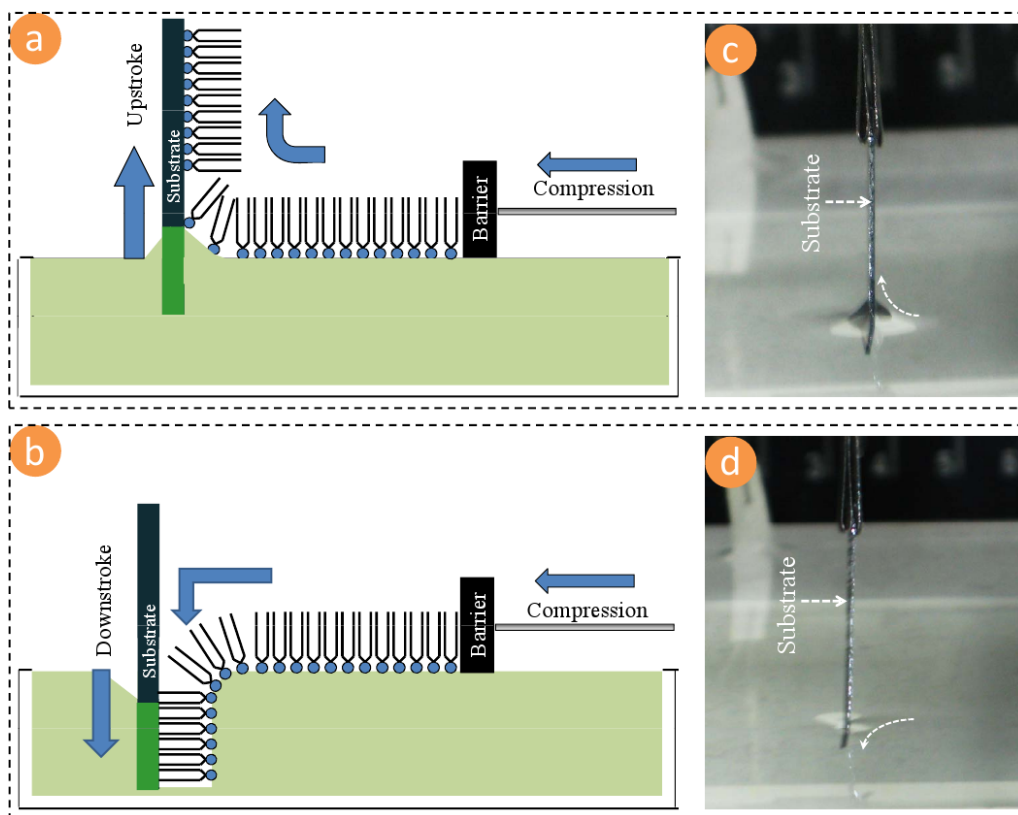
Figure 3.5: A schematic presentation of LB film deposition on (a) a hydrophilic and (b) a hydrophobic substrate. The real images of water meniscus at the time of LB film deposition on (c) a RCA cleaned hydrophilic Si and (d) H-passivated hydrophobic Si substrates in my experiments.

during the upstroke and the tails attach to the tails of the previous layer during the downstroke, in accord with what we expect from amphiphilic molecules. There are several consequences of dependence of molecular orientation on the dipping direction. First, the basic unit of an ideal LB multilayer is a bi-layer. Second, the first layer can be deposited only on the upward pass on hydrophilic substrates and on the downward pass on hydrophobic substrates as shown in Fig. 3.5a,c and b,d respectively. Third, in air hydrophobic tails will be at the topmost layer while in water hydrophilic headgroups will be at the outermost layer.

B. Instrument:

The Langmuir trough (Apex Instruments) used to prepare Langmuir monolayers and LB films is shown in Fig. 3.4. The essential elements of that trough are (a) the bath, usually made of a hydrophobic material like teflon (b) the mobile barriers for controlling the surface area (c) a balance for measuring the surface pressure and (d) a dipper for dipping the substrate through the monolayer. This trough has one bath having a maximum area 19.1×44 cm^2. The bath has independent hydrophilic barrier settings. The barriers can move with desired speed from 0.5 to 85 mm/min by stepper motors.

C. Deposited samples

NiA and CdA nanolayers or LB films were deposited on differently passivated Si substrates (each of about 15×10 mm^2 size, n-type, resistivity 5-10 Ω-cm) using this Langmuir trough. Immediately after the chemical treatment, all the substrates were kept inside the Milli-Q water until LB deposition. Prior to deposition, $\pi - A$ isotherm of Langmuir monolayers on water surface were recorded. The monolayers were compressed at a constant rate of 3 mm/min. All depositions were done at $\pi = 30$ mN/m and at room temperature (22°C). Depositions were carried out at a speed of 2 mm/min and the drying time allowed after each up stroke was 10 min.

I. NiA/X-Si samples

Arachidic acid [CH$_3$(CH$_2$)$_{18}$COOH, Sigma, 99%] molecules were spread from a 0.5

mg/ml chloroform (Aldrich, 99%) solution on Milli-Q water (resistivity 18.2 MΩ-cm) containing nickel sulphate ($NiSO_4.2H_2O$, Merck, 99%) in the Langmuir trough. The pH of the water subphase containing 0.2 mM nickel sulphate was maintained at 8.5-9.0 using sodium hydroxide (NaOH, Merck, 98%). No buffers were used to maintain the pH of the subphase. Nearly 8 h were spent for pH stabilization including initial magnetic stirring.

LB films on differently-terminated Si(001) substrates were deposited using different numbers of down and/or up strokes of substrates through Langmuir monolayers. On OH-Si surfaces, two NiA LB films were deposited, one by 1 (up) stroke and another by 3 (up-down-up) strokes, referred as 1s-NiA/OH-Si and 3s-NiA/OH-Si, respectively. On H-Si surface, one NiA LB film was deposited by 2 (down-up) strokes and referred as 2s-NiA/H-Si. On Br-Si surfaces, three NiA LB films were deposited, first by 1 (up) stroke, second by 2 (down-up) strokes, and third by 3 (up-down-up) strokes, referred as 1s-NiA/Br-Si, 2s-NiA/Br-Si, and 3s-NiA/Br-Si, respectively. Films have been checked for reproducibility.

On H-Si substrate first two NiA LB films were deposited in the 'high pH' condition (similar to that of 2s-NiA/H-Si sample prepared earlier), one by single (up) stroke and another by three (up-down-up) strokes, referred as 1s-NiA/H-Si and 3s-NiA/H-Si, respectively. Two more samples were prepared in 'normal pH' condition (i.e. pH ≈ 6), one by single (up) stroke and another by three (up-down-up) strokes, referred as 1s-NiA/H-Si(NpH) and 3s-NiA/H-Si(NpH), respectively. Then one film was prepared by single up stroke in 'high pH' condition after keeping the substrate in the subphase of water for longer time (about 90 min), referred as 1s-NiA/H-Si(LT). One further sample was prepared by three (up-down-up) strokes in 'high pH' condition, however, arachidic acid molecules were spread on the trough only before final up stroke, referred as 1s-NiA/H-Si(2sNi).

II. CdA/X-Si samples

The preparation of CdA LB films is similar to that of NiA LB films. In brief, arachidic acid ($CH_3(CH_2)_{18}COOH$, Sigma, 99%) molecules were spread from a 0.5

mg/ml chloroform (Aldrich, 99%) solution on Milli-Q water (resistivity 18.2 MΩ cm) containing 0.2 mM cadmium chloride ($CdCl_2.2H_2O$, Merck, 99%) in the Langmuir trough. The pH of the subphase water was maintained at 8.5-9.0.

CdA LB films were deposited on OH-Si, H-Si and Br-Si substrates using different numbers of down and/or up strokes of substrates through CdA Langmuir monolayers. On OH-Si substrate, one CdA LB film was deposited by three strokes (up-down-up) and labeled as 3s-CdA/OH-Si. On H-Si substrate, one CdA LB film was deposited by two strokes (down-up) and labeled as 2s-CdA/H-Si. Finally on Br-Si subtrates, three CdA LB films were deposited, first by one stroke (up), second by two strokes (down-up) and third by three strokes (up-down-up), labeled as 1s-CdA/Br-Si, 2s-CdA/Br-Si and 3s-CdA/Br-Si, respectively. Films were checked for reproducibility.

3.2   Characterization

The characterization of the samples were carried out using complementary techniques. X-ray scattering in general and x-ray reflectivity (XRR) in particular are used extensively to get the information about the samples from the reciprocal space mapping. On the other hand, scanning electron microscopy (SEM) and scanning probe microscopy (SPM) are also used extensively to get large area average information and small area details information, respectively, in real space. The working principle of all such techniques along with the instruments are described in details.

It is necessary to mention that, apart from the above mentioned experimental techniques, there are few techniques namely secondary ion mass spectrometry (SIMS), x-ray photoelectron spectroscopy (XPS) and contact angle (CA) measurement, which we have used occasionally for further verification. Such techniques will be described in relevant places.

3.2.1   X-ray scattering

A. Working principle:

X-rays can interact with matter through different mechanisms [41; 165]. However, in this discussion, we shall consider only Thomson scattering, where a charged particle is accelerated by the oscillating electric field of the incident radiation and then the particle re-radiates the energy gained. The scattering is more efficient for the light electrons than the heavy nuclei (actually it is proportional to inverse of mass). When the frequency of the electromagnetic radiation is much larger than the characteristic atomic frequencies, which is the general case for x-rays and the light atoms of soft materials, the electrons can be considered as free electrons [166; 167] and the materials can be simply characterized by its electron density ρ. Thus, on being irradiated by x-rays, the electron undergoes an acceleration, which is due to the force exterted by the incident oscillating electric field

$$E(r,t) \quad = \quad E(r)e^{-i\omega t} \tag{3.6}$$

where $\omega = \frac{2\pi c}{\lambda}$ is the angular frequency and λ is the wavelength of x-rays, and c of course, is the free space velocity. Let v be the electron velocity and ($-e$) its charge, then for electron mass m

$$m\dot{v} \quad = \quad (-e)E(r)e^{-i\omega t} \tag{3.7}$$

Hence the instantaneous position of the electron is given by

$$r \quad = \quad \frac{e}{m\omega^2}E(r)e^{-i\omega t} \tag{3.8}$$

For electron density ρ, the dipole moment per unit volume or the polarisation is then

$$P \quad = \quad \rho \times (-er) = -\frac{\rho e^2}{m\omega^2}E(r)e^{i\omega t} \tag{3.9}$$

Lorentz classical radius of the electron is

$$r_e \quad = \quad \frac{e^2}{4\pi\epsilon_0 mc^2} \simeq 2.818 \times 10^{-15} \tag{3.10}$$

In terms of r_e, the polarisation is

$$P(r,t) = -\frac{\epsilon_0 r_e \lambda^2 \rho(r)}{\pi} E(r) e^{i\omega t} \qquad (3.11)$$

The electric displacement vector D = ϵ_0E + P and it is also related to electric field through refractive index $n(r)$ by the relation D = ϵ_0 n^2(r)E. Hence

$$P(r,t) = \epsilon_0 [n^2(r) - 1] E(r) \qquad (3.12)$$

From the above two equations (4.8) and (4.9) we get the refractive index

$$n = 1 - \delta \qquad (3.13)$$

where $\delta = \frac{\lambda^2 r_e \rho}{2\pi}$. The refractive index of the medium considering absorption can be written as [166; 167]

$$n = 1 - \delta - i\beta \qquad (3.14)$$

where $\beta = \frac{\mu\lambda}{4\pi}$ is much smaller than δ, μ being the linear absorption coefficient. The imaginary part is due to the absorption of the material.

From Eq. 3.14 it can be seen that for any material medium, the refractive index is slightly ($\delta \sim 10^{-6}$ to 10^{-5}) less than 1. This is a specific property of x-rays (and neutrons). Thus air or vacuum has a refractive index of unity, greater than, any material and a beam impinging on a flat surface can be totally reflected. The condition for this is that the angle of incidence θ (angle between incident ray and surface) must be less than a critical angle θ_c. This angle can be obtained by applying Snell-Descartes' law with $\cos\theta_{tr} = 1$ (the subscript standing for the transmitted radiation), yielding in absence of absorption:

$$\cos\theta_c = n = 1 - \delta \qquad (3.15)$$

Since δ is of the order of 10^5, the critical angle for total external reflection is extremely small. At small angles, $\cos\theta_c$ can be approximated as 1 - $\theta_c^2/2$ and Eq. 3.15 reduces to

$$\theta_c = \sqrt{2\delta} \qquad (3.16)$$
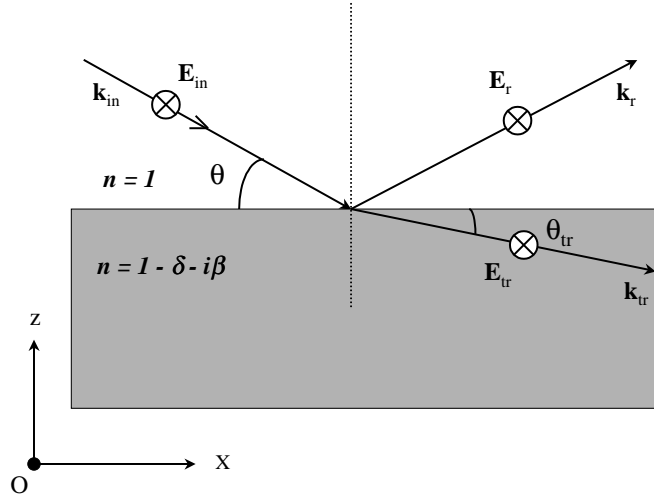
Figure 3.6: Reflection and refraction of an incident wave polarised along Y axis and travelling in the XOZ plane of incidence.

The total external reflection of an x-ray (or neutron) beam is therefore only observed at grazing angles of incidence below about $\theta < 0.5$. At large angles, the reflectivity decreases very rapidly.

3.2.1.1   X-ray reflectivity

The theory of XRR is valid under the assumption that electron density is continuous. Under this approximation, the reflection is treated like in optics, and the reflection and transmission coefficients can be derived by writing the conditions of continuity of the electric and magnetic fields at the interface. For a flat surface the reflected intensity will be confined in a direction symmetric to the incident one and will be labeled as specular. Specular reflectivity, which is the square of the modulus of reflection coefficient, is the quantity measured in an experiment. It is conventionally defined as the ratio

55

$$R(\theta) = \frac{I(\theta)}{I_0} \tag{3.17}$$

or

$$R(q) = \frac{I(q)}{I_0} \tag{3.18}$$

where $I(\theta)$ or $I(q)$ is the reflected intensity for an angle of incidence θ (or wavevector transfer q), and I_0 is the intensity of the incident beam. The magnitude of this wavevector transfer $|q| = |k_{sc} - k_{in}| = (4\pi/\lambda)\sin\theta$. The expression for the electric field in a homogeneous medium is derived from Maxwell's equations which when combined, lead to the propagation equation of the electric field known as Helmholtz's equation

$$\Delta E + k_j^2 E = 0 \tag{3.19}$$

where k_j is the wavevector in medium j.

The electric field which is the solution of Helmholtz's equation is given for the incident (in), reflected (r) and transmitted (tr) plane waves by

$$\mathbf{E}_j = A_j e^{i(wt - \mathbf{k}_j \cdot \mathbf{r})} \hat{y} \tag{3.20}$$

with $j = in$, r or tr, $k_0 = |k_{in}| = |k_r| = 2\pi/\lambda = |k_{tr}|/n$, and $\hat{y}$ is a unit vector along the y-axis [shown in Fig. 3.6]. The above solution of the Helmholtz's equation is for an electromagnetic plane wave propagating in the XOZ plane of incidence, with its electric field polarised normal to this plane along the OY direction.

Also it is obvious that for the incident wave the z component of the incident and reflected wave-vectors have opposite directions with same magnitude whereas for parallel component all incident, reflected and transmitted wave-vectors have same magnitude and value, i.e., $k_{r,z}^{in} = -k_{i,z}^{in}$ and $\mathbf{k}_{i\parallel}^{in} = \mathbf{k}_{r\parallel}^{in} = \mathbf{k}_{t\parallel}^{in}$. If r_{12} and t_{12} are the reflection and transmission coefficients then according to definition $\mathbf{E}_r = r_{12}^{in}\mathbf{E}_i$ and $\mathbf{E}_t = t_{12}^{in}\mathbf{E}_i$.

Solving the boundary conditions for electric and magnetic fields at the interface $(z = 0)$ we obtain

$$1 + r_{12} = t_{12} \tag{3.21}$$

$$1 - r_{12} = nt_{12}\frac{\sin\theta_{tr}}{\sin\theta} \tag{3.22}$$

Combining these two equations we obtain the reflection coefficient

$$r_{12} = \frac{\sin\theta - n\sin\theta_{tr}}{\sin\theta + n\sin\theta_{tr}} \tag{3.23}$$

Again applying Snell-Descarte's law

$$\cos\theta = n\cos\theta_{tr} \tag{3.24}$$

the reflection coefficient becomes

$$r_{12}(\theta) = \frac{\sin\theta - \sqrt{n^2 - \cos^2\theta}}{\sin\theta + \sqrt{n^2 - \cos^2\theta}} = \frac{k_{z,1} - k_{z,2}}{k_{z,1} + k_{z,2}} \tag{3.25}$$

For small incident angles and considering the absorption of x-ray beam by the material the Fresnel reflectivity becomes

$$R(\theta) = r(\theta)r^*(\theta) = \left|\frac{\theta - \sqrt{\theta^2 - \theta_c^2 - 2i\beta}}{\theta + \sqrt{\theta^2 - \theta_c^2 - 2i\beta}}\right|^2 \tag{3.26}$$

or in terms of wavevector transfer

$$R(q) = \left|\frac{q_z - \sqrt{q_z^2 - q_c^2 - \frac{32i\pi^2\beta}{\lambda^2}}}{q_z + \sqrt{q_z^2 - q_c^2 - \frac{32i\pi^2\beta}{\lambda^2}}}\right|^2 \tag{3.27}$$

The transmission coefficient $t(\theta)$ is obtained from the relation $1 + r = t$, and it becomes

$$t_{12}(\theta) = \frac{\sin\theta}{\sin\theta + \sqrt{n^2 - \cos^2\theta}} = \frac{2k_{z,1}}{k_{z,1} + k_{z,2}} \tag{3.28}$$

The transmitted intensity, for small incident angle and absorbing material, is

$$T(\theta) = t(\theta)t^*(\theta) = \left|\frac{2\theta}{\theta + \sqrt{\theta^2 - \theta_c^2 - 2i\beta}}\right|^2 \tag{3.29}$$

or

$$T(q_z) = tt^* = \left| \frac{2q_z}{q_z + \sqrt{q_z^2 - q_c^2 - \frac{32i\pi^2\beta}{\lambda^2}}} \right|^2 \tag{3.30}$$

The transmitted intensity has a maximum at $\theta = \theta_c$ and is the origin of the so-called Yoneda wings which are observed in transverse off-specular scans. It can be shown that the z-component of the wavevector in medium j, i.e., $k_{z,j}$ is

$$k_{z,j} = k_j \sin\theta_j = \sqrt{k_j^2 - k_{x,j}^2} \tag{3.31}$$

But as $k_{x,j}$ is conserved and is equal to $k_0 cos\theta$, the z-component of k_0 in medium j is

$$k_{z,j} = \sqrt{k_0^2 n_j^2 - k_0^2 \cos^2\theta} = k_0 \sqrt{\theta^2 - 2\delta_j - 2i\beta_j} \tag{3.32}$$

In case of stratified media or multilayers, the reflectivity is calculated by applying the boundary conditions for electric and magnetic fields at each of the interfaces between the slabs of constant electron density. For example, in the case of a thin film of finite thickness d, there are two interfaces, namely film-air (at $z = 0$) and film-substrate (at $z = d$) interfaces. Applying boundary conditions at these two interfaces we obtain the reflection coefficient for the film-substrate interface as

$$r_{2,3} = \frac{k_{z,2} - k_{z,3}}{k_{z,2} + k_{z,3}} e^{(-2ik_{z,2}d)} \tag{3.33}$$

where the extra phase factor comes from the applying boundary condition at $z = d$. Now using matrix method [41] or by solving the simple algebra noting the fact that $r_{21} = -r_{12}$ we can write the reflectance from this thin film-substrate system as

$$r = \frac{r_{12} + r_{23}}{1 + r_{12}r_{23}} \tag{3.34}$$

Extending the above approach for a multilayered system having N number of thin layers (stratified homogeneous media) of thickness d and solving simultaneously a set of equations like Eq. 3.33 one can arrive at a recursive formula given by

$$r_{n-1,n} = \frac{r_{n,n+1} + F_{n-1,n}}{1 + r_{n,n+1}F_{n-1,n}} e^{(-2ik_{z,n-1}d_{n-1})} \tag{3.35}$$

where

$$F_{n-1,n} = \frac{k_{z,n+1} - k_{z,n}}{k_{z,n+1} + k_{z,n}} \qquad (3.36)$$

To obtain the reflectivity of this system, one solves this recursive relation given by Eq. 3.35 from the bottom layer with the knowledge that $r_{n,n+1} = 0$, since the thickness of this medium (substrate thickness) can be taken as infinite and also the thickness d_0 of vacuum or air is infinite.

For rough surfaces or interfaces it is known that reflectivity is smaller than the smooth surface and this deviation increases with q_z. Assuming the independence of the different interface roughness the reflectance can be written as

$$r_{n-1,n} = r^F_{n-1,n} e^{(-2ik_{z,n-1}k_{z,n}\sigma^2)} \qquad (3.37)$$

or

$$r_{n-1,n} = r^F_{n-1,n} e^{(-\frac{1}{2}iq_{z,n-1}q_{z,n}\sigma^2)} \qquad (3.38)$$

The parameter σ_n is the measure of the roughness between $(n-1)^{th}$ and $(n)^{th}$ interfaces, and it is seen that roughness acts as a Debye-Waller like factor. As in diffraction the Debye-Waller factor accounts for the thermal vibrations reducing the diffracted intensity, here roughness reduces the reflectance from $r^F_{n-1,n}$, the reflectance for the smooth surface, i.e., Fresnel reflectance. Thus for rough surfaces, the specular reflectivity falls faster with increasing roughness value σ and the amplitude of the fringes reduces significantly at high wave-vector transfers. For multilayers, reduction in the reflectivity may also happen due to the interdiffusion of the atoms or molecules at the interfaces, forming a finite interfacial width. These finite widths are also treated as roughnesses of these interfaces.

B. Instrument:

For XRR measurements we have used versatile x-ray diffractometer (VXRD) (D8 Discover, Bruker AXS) which is shown in Fig. 3.7. In the VXRD a Cu sealed tube

generates x-rays of the required radiation energy, focal spot and intensity. The focal spot (also called focal spot on target) and takeoff angle are critical features in the production of x-rays by sealed tube. Sealed tube, of course, produce x-rays by bombarding the target sample with electrons generated from the filament (cathode). The area bombarded by electrons is called focal spot on target and the angle between the primary x-ray beam and the surface is called takeoff angle. The takeoff angle can be set from 3° to 7°. In this system the normal emission angle is 5°. Sealed tube normally has 2 to 4 beryllium windows through which x-rays exit. The focal spot is typically rectangular with a length-to-width ratio is of 10 to 1. The projection along the length of the focal spot at a takeoff angle from the anode surface is called spot focus. For fine focus the focal spot size at anode is 0.4×8 mm^2 and spot focus size is 0.4×0.8 mm^2. The emerging primary x-rays then passes through a parabolic multilayer mirror which is called Göbel mirror. The Göbel mirror is the bent gradient multilayer optics. The standard lengths of the multilayer optics are 40 mm and 60 mm. This mirror converts the divergent beam emitted from the x-ray source into a intense parallel beam. These special diffractive properties are valid for the $K\alpha$ radiation of the source, so that the mirror is mainly diffracting the $K\alpha$ part of the spectrum.

In VXRD setup, goniometer is a high-precision, two-circle goniometer with independent stepper motors and optical encoders for θ and 2θ circles. The sample stage is usually mounted on the inner θ circle of the goniometer. The goniometer can be used in horizontal θ-2θ, vertical θ-2θ and vertical θ-θ geometries. In θ-2θ mode, the sample rotation is defined as ω rotation, so a sample stage directly mounted on the goniometer inner circle is also called ω-stage. The used sample stage is a 1/4-circle Eulerian cradle. This cradle has two rotational (χ and ϕ) and three translational (X, Y and Z) motions. The corresponding θ, ϕ and χ motors movement have been shown in Fig. 3.8.

In this setup, the scattered beam is detected using NaI scintillation (point) detector. The detector interface board generates the high-voltage required for the operation of scintillation and proportional counters. It contains a high speed pulse

Figure 3.7: Picture of VXRD instrument used in x-ray reflectivity measurements.
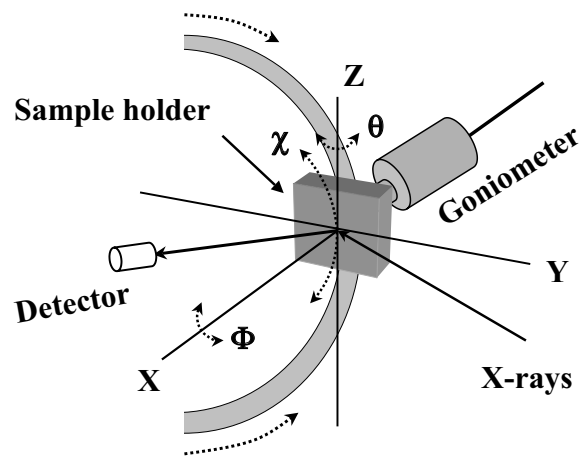
Figure 3.8: Rotation geometry of the θ, ϕ and χ motors in VXRD setup with 1/4-circle Eulerian cradle.

amplifier with a pulse shaping stage, line shift correction and baseline restoration unit and also two discriminator windows including complete pulse counting unit. In addition there is a digital count input for various kinds of detectors having a digital pulse output.

The VXRD unit is kept in a radiation protection housing shown in Fig. 3.7. A lead glass window at the front of the radiation protection housing enables the samples to be changed and or the diffractometer mounts to be modified. The window shutter of the x-ray tube stand closes automatically when this window is opened. Two red LEDs light up when the window shutter is open and a green LED lights up when the window shutter is closed.

In our study data were taken in specular condition, i.e., the incident angle (θ) is equal to the reflected angle (θ) and both are in a scattering plane. Under such condition, a non-vanishing wave vector component, q_z, is given by $(4\pi/\lambda)\sin\theta$ with resolution 0.0014 Å^{-1}. The qualitative idea about the samples has been obtained from the Kiessig fringes of the XRR profiles. To get a quantitative information i.e., electron density profile (EDP) along depth of the samples, all XRR profiles have been analyzed using Parratt's formalism [168]. For the analysis, each film has been divided a into number of layers and roughness has been incorporated at each interface [169]. The thickness, electron density, and roughness associated with each layer were then set as fitting parameters.

3.2.2 Scanning probe microscopy

A. Working principle:

Within the past decade, a family of powerful surface imaging techniques, known collectively as SPM [170; 171], has developed in the wake of the invention of the scanning tunneling microscope (STM). Each scanned probe technique relies on a very sharp probe positioned within a few nanometers above the surface of interest. The movement of the tip (probe) or the sample is performed by an extremely precise positioning device known as scanner made using the concept of piezo-electric effect.
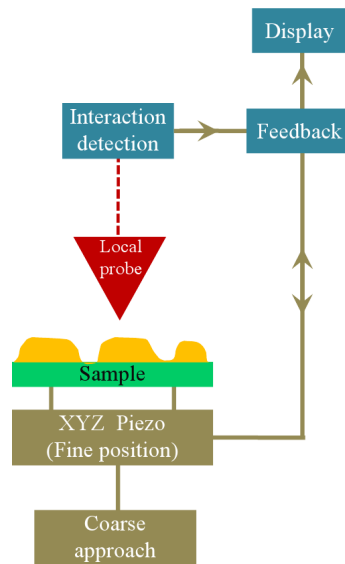
Figure 3.9: Generalized schematic of a SPM.

The scanner is capable of providing subangstrom resolution in x, y, and z-directions. The generalized schematic of SPM is shown in Fig. 3.9. When the probe translates laterally (horizontally) relative to the sample, any change in the height of the surface causes the detected probe signal to change. In general, if the probe signal decreases, this means that the point on the surface directly beneath the probe is farther from the probe than the previous point was. Conversely, if the probe signal increases, then the point on the surface is closer to the probe than the previous point. The electronic circuit that controls the vertical position of the probe relative to the sample uses these changes in the probe signal as sensory feedback to decide which direction (up or down) to move the probe to maintain a constant probe signal. When the probe signal decreases, the circuit realizes that the surface is now farther away, so it moves the probe down until the signal increases to the same level that was measured at the previous point. Similarly, the circuit responds to increases in probe signal by moving the probe up, away from the surface, until the signal decreases back to the desired level. The distance that the probe is moved up or down to return the probe signal to the desired value is therefore related to the height at each point. To create

a 3D map of surface height, the probe is scanned horizontally (let's say parallel to the x-axis) along a series of parallel lines, while the height at each point along each line is recorded. Each scan line is displaced laterally from the previous line by a small distance along the y axis, so that, after several hundred lines have been scanned, the total displacement in the y direction is equal to the length of each line in the x direction, and a square region of the sample has been measured. We now have a measure of height at each point in a 2D region of the sample, or $z(x, y)$, which is exactly analogous to a topographic map of (if the surface is very rough, for example) the Grand Canyon, except that the dimensions are scaled down by a factor of a trillion (10^{12}) or so! Probe signals that have been used to sense surfaces include electron tunneling current, interatomic forces, photons, capacitive coupling, electrostatic force, magnetic force, and frictional force. In two prominent cases [STM and atomic force microscopy (AFM)], the probe signals depend so strongly on the probe-substrate interaction that changes in substrate height of as little as 0.01 nm can be detected. In addition, the STM and AFM probes can interact with regions of the substrate that are of atomic-scale lateral dimensions, which allows the substrate height to be measured with sub-nm lateral resolution as well. It was the ability of the STM to image individual atoms on surfaces that won the inventors of the STM (Gerd Binnig and Heinie Rohrer of IBM Research in Zurich) the Nobel Prize for Physics in 1986. For resolving individual atoms on insulating surfaces, Binnig, Quate, and Gerber (1986) introduced a method similar to STM, AFM.

3.2.2.1   Atomic force microscopy

In AFM a probing tip is attached to a flexible cantilever which is deflected in response to the forces between the tip and the sample. Forces between the tip and the sample surface cause the cantilever to bend, or deflect. The deflection of the cantilever is measured by detecting the deflection of a light beam reflected from the back of the cantilever onto a position sensitive detector (PSD) as shown in Fig. 3.10. The measured cantilever deflections, as a function of the lateral sample
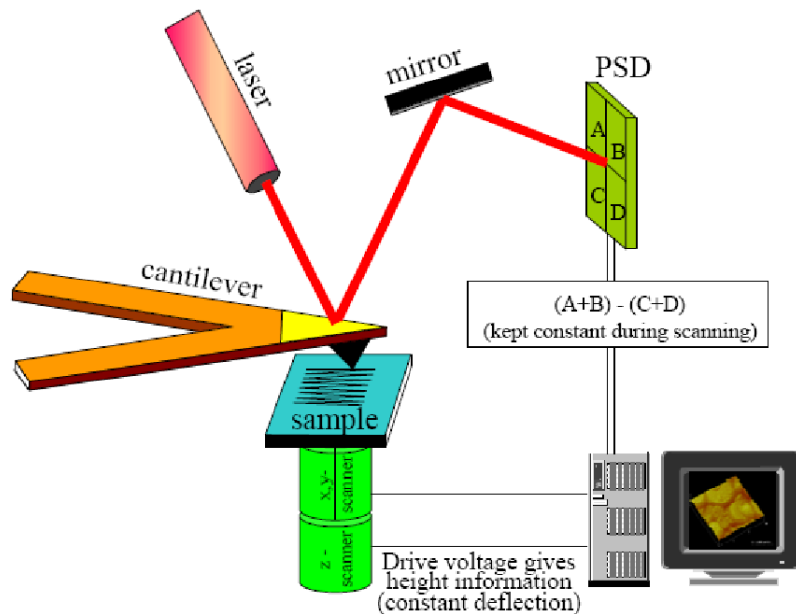
Figure 3.10: Schematic showing the working principle of AFM.

position, allows a computer to generate a map of surface topography. Although several forces contribute to the cantilever the dominant contribution usually comes from van der Waals force. The dependence of this force on tip-sample distance is shown in Fig. 3.11. As the atoms are gradually brought together, the attractive force between them increases until they are so close together that their electron clouds begin to repel each other electrostatically. This electrostatic repulsion progressively weakens the attractive force as the interatomic separation continues to decrease and when the distance between the atoms reaches a couple of angstroms, the total van der Waals force becomes repulsive. In AFM, the local variation of the force acting between the tip and the sample surface is measured in order to generate the 3D images of the surface. The force, $F(r)$ can be derived from the Lennard-Jones potential $V(r)$ [171], which combines the attractive van der Waals and repulsive atomic potentials. The Lennard-Jones potential can be written as

$$V(r) \quad \propto \quad \left(\frac{\sigma}{r^{12}} - \frac{\sigma}{r^6} \right) \tag{3.39}$$
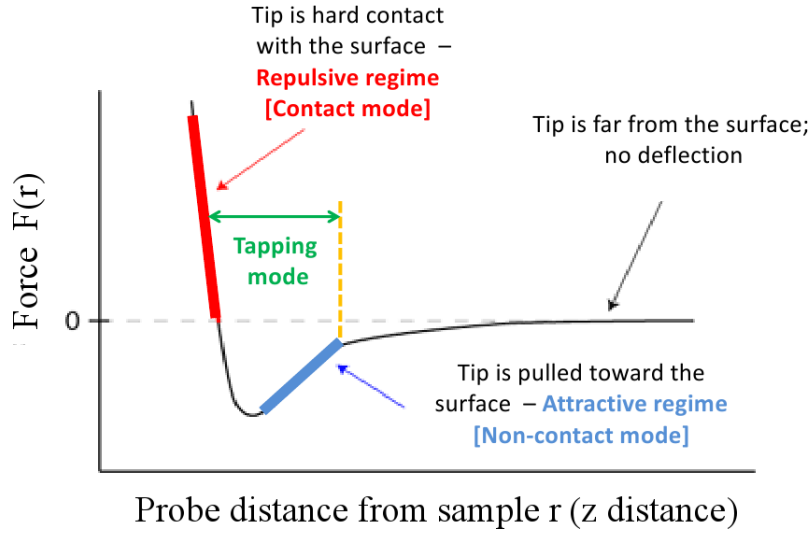
Figure 3.11: Interatomic force vs distance curve. Typical regions of operation of different modes of AFM are indicated.

Using the relation $F(r) = -\partial V/\partial r$ the force can be written as

$$F(r) \quad \propto \quad \left(\frac{\sigma}{r^{13}} - \frac{\sigma}{r^7} \right) \tag{3.40}$$

This force is exerted on the cantilever causing its deflection according to the Hooke's law:

$$F(r) \quad = \quad -kx \tag{3.41}$$

where, k is the spring constant of the cantilever and x is the cantilever deflection. A 3D image of the surface is finally constructed by recording the cantilever motion in the z-direction for different values of x and y. Depending upon the requirement, AFM can be operated in following three modes.

(a) Contact mode: In contact-AFM mode, also known as repulsive mode, an AFM tip makes soft 'physical contact' with the sample. The force between the cantilever and the sample surface is repulsive in this mode which is shown in Fig. 3.11. As the scanner gently traces the tip across the sample (or the sample under the tip), the

contact force causes the cantilever to bend to accommodate changes in topography. The slope of the force-distance curve in this region is very steep, which means that in AFM, when the cantilever pushes the tip against the sample, the cantilever bends rather than forcing the tip atoms closer to the sample atoms.

When AFM detects a cantilever defection, it can operate in any of two modes to produce a topographic data: constant force mode and constant height mode. In constant force mode, the deflection of the cantilever is fed to feedback circuit that moves the scanner up and down in z-direction in response to the topography by keeping the cantilever deflection constant. The voltage that the feedback amplifier applies to the piezo is a measure of the height of features on the sample surface. Thus the image is generated from the scanner motion. In constant height mode, the height of the scanner is kept fixed during scans. Here, the spatial variation of the cantilever deflection, can be used directly to obtain the topographic information. Constant height mode is used for taking atomic scale images of atomically flat surfaces, where the cantilever deflections and associated variations on applied forces are small. Constant force mode is more preferred and widely used in various applications.

(b) Intermittent-contact or tapping mode: In intermittent-contact AFM (IC-AFM) or tapping mode the vibrating cantilever tip is brought closer to the sample so that at the bottom of its travel it just barely hits, or 'taps' the sample. The IC-AFM operating region is indicated on the force-distance curve. For IC-AFM mode operation, the cantilever oscillation amplitude is maintained constant by a feedback loop, which adjusts the tip-sample separation to maintain constant amplitude and force on the sample. In tapping mode those sample surfaces are used that can be easily damaged, loosely hold to their substrate, or difficult to image by other AFM techniques. This mode also overcomes problems associated with friction, adhesion, and other difficulties often present in conventional AFM scanning methods. This is the mode generally used for liquid surfaces.

(c) Non-contact mode: Non-contact AFM (NC-AFM) is a vibrating cantilever techniques in which an AFM cantilever is vibrated near the surface sample. The stiff cantilever vibrates near its resonant frequency (typically from 100 to 400 kHz) with an amplitude of a few tens to hundreds of angstroms. The spacing between tip and sample is also of the same order. In this mode there is little or no contact between tip and the sample. The changes in the resonant frequency or the vibration amplitude as the tip comes near the sample surface is detected. This NC-AFM mode is mainly used for very soft or elastic samples.

3.2.2.2 Scanning tunneling microscopy

STM [172] has permitted surfaces of materials to be imaged on an atomic scale and has also been used in cross section to study device physics directly. STM is well known for its morphological capabilities within the atomic regime when examining conducting surfaces. However, it is worth commenting on the care required when interpreting images as STM experiments produce a map of the electron density across a surface which is therefore a mixture of both topography and local electronic effects. Hence it is clear that care must be taken when inferring structural information. This issue can become even more important when delocalization occurs in the bonding at the surface, as a correlation between atomic positions and regions of high charge density is difficult to infer. Under such conditions, the electronic information must be decoupled from the topography using a combination of bias dependent imaging and theoretical modeling. The nature of the STM tip is also important. For example, even if the tip is atomically sharp permitting the maximum spatial resolution, features in the image, and also the image contrast, can be dependent on the presence of contaminants or adsorbates at the tip apex. The finite size of the tip apex (radius of curvature) can also influence the STM images. Tersoff and Hamann (TH) made an assumption that the tunnel current is dominated by a single s state of the tip, which leads to a simple expression involving only the local density of states (LDOS) of the surface.

(a)

(b)
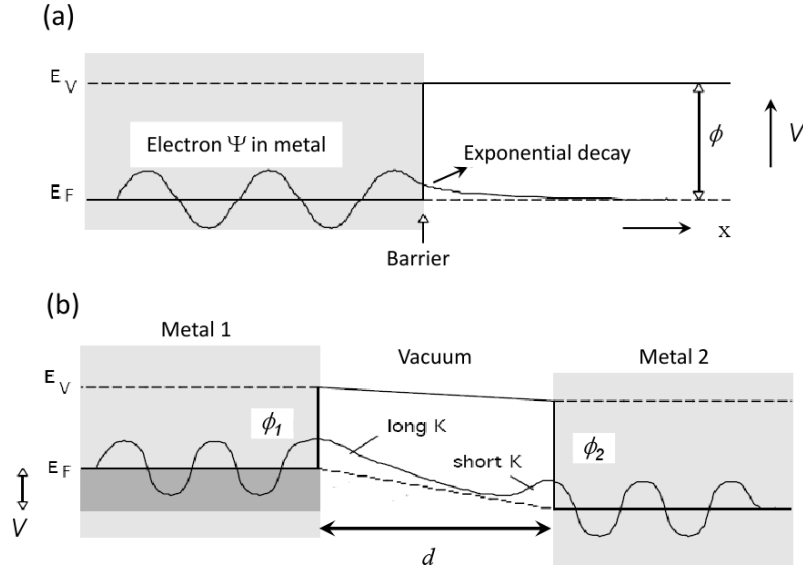
Figure 3.12: Schematic of quantum mechanical effect of tunneling , (a) exponential leakage of the wave functions from a metal into vacuum, (b) application of a voltage and tunneling between two metals because of the overlap of the wave function tails.

Scanning tunneling microscopy is based on the quantum mechanical effect of tunneling illustrated in the Fig. 3.12 the wave functions at the Fermi level exponentially leak out of the metal with an inverse decay length of

$$k \quad = \quad \frac{\sqrt{2m\phi}}{\hbar} \tag{3.42}$$

where m is the mass and ϕ is the local work function. If now two metals are brought in close contact and a small voltage (V) is applied between them, a tunneling current $I(x, y; V)$ can be measured which is expressed by

$$I(x, y; V) \quad \propto \quad f(x, y; V) \exp[-2k(V)d(x, y)] \tag{3.43}$$

where $d(x, y)$ is the tip-sample distance, and $f(x, y; V)$ is the tip-sample joint DOS at the position (x, y). The important message here, and the reason why STM works, is the exponential dependence of the tunneling current on the distance between the conductors.

An atomically sharp tip (ideally with only one atom at the tip) is brought up to a distance d ($\sim$ 0.5 - 1 nm) from a surface. If a voltage V ($\sim$ 10V) is applied across the tip and surface, and if the distance d is small enough, a current I ($\sim$ nA to pA) will flow between tip and surface. The current is able to flow because of the wave functions of the orbital associated with the surface and the tip in a quantum mechanical tunneling process. It is obvious that if the distance between surface and tip is decreased, the orbital overlap will increase and thus the tunneling current will increase. If the voltage across surface/tip is held constant, then as the tip is moved across the surface, the STM operator can keep the current constant such that the tip follows the surface contours and a topographic image can be constructed by computer. By applying a potential difference so that the surface is positive with respect to the tip, the filled states are studied, while a negative potential of the surface with respect to the tip gives an image due to the empty states. Imaging of the surface topography may be carried out in one of two ways: in *constant height mode* (in which the tunneling current is monitored as the tip is scanned parallel to the surface) and in *constant current mode* (in which the tunneling current is maintained constant as the tip is scanned across the surface).

B. Instrument:

UHV-SPM (beam deflection AFM, Omicron NanoTechnology) used for imaging the sample surface in UHV condition is shown in Fig. 3.13. This instrument uses a single tube scanner with a maximum scan range of about 10 μm$\times$10 μm and a z-travel of about 1.5 μm. A z-resolution of better than 0.01 nm can be achieved. The scanner is positioned with a 3-axes linear piezo motor. It uses slip/stick effects related to inertia forces when a piezo is driven in a fast/slow sequence. The sliders are magnetically coupled to three shear piezos which are driven with a sawtooth voltage input. The sliders are transported during the slow movement of the piezo and slip during the fast piezo motion due to their inert mass. For successful high-resolution scanning probe microscopy a high quality vibration decoupling system is essential. The sample stage is suspended by four soft springs which are protected
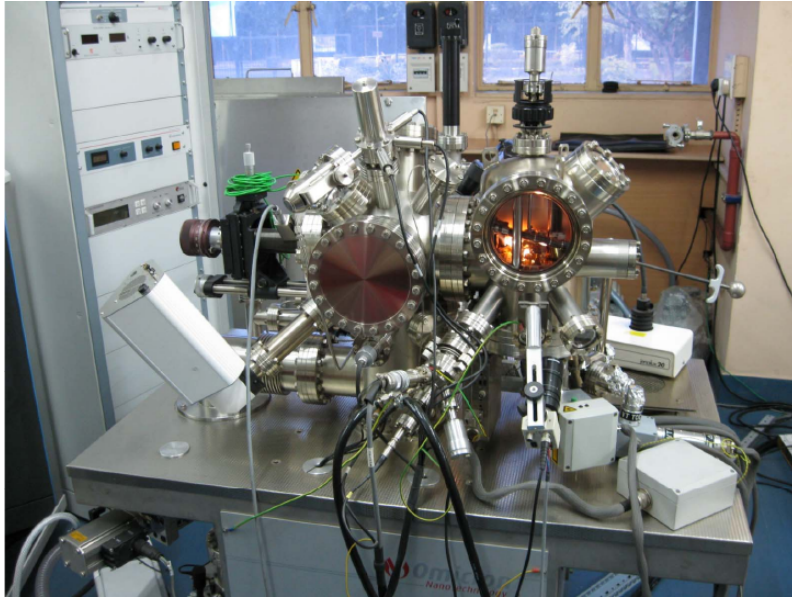
Figure 3.13: Picture of UHV-SPM instrument (beam deflection AFM, Omicron NanoTechnology).

Figure 3.14: Picture of AFM tip stage of UHV-SPM
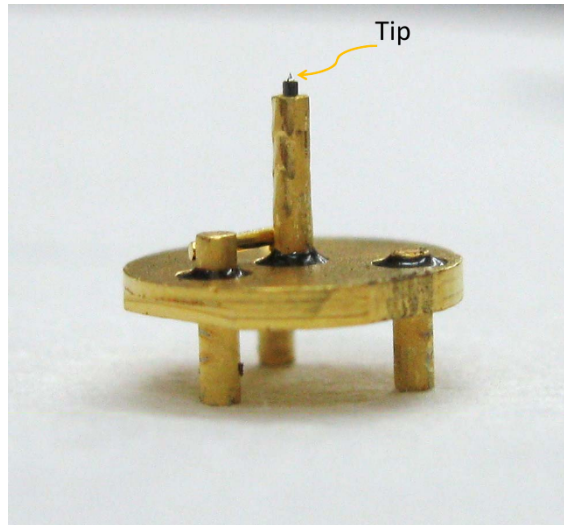
Figure 3.15: Picture of STM tip stage of UHV-SPM.

by surrounding columns. The resonance frequency of the spring suspension system is about 2 Hz. Vibrations of the suspension system are interpreted using a nearly non-periodic eddy current damping mechanism. For this reason the sample stage is surrounded by a ring of copper plates which come down between permanent magnets. The spring suspension system can be blocked to allow tip or sample exchange, adjustments, etc. by means wobblestick. Blocking is achieved using a push-pull motion feedthrough. For STM measurement only we have to change the tip. The tip stage is shown in Fig. 3.15. This tip is made of Pt/Ir material.

Ambient SPM (Nanoscope-IV, Veeco) used for mapping the sample surface in ambient conditions is shown in Fig. 3.16. In this case the scanner is attached to the sample holder. Two types of scanners - 10 μm $\times$ 10 μm with a vertical range of 2.5 μm and 0.4 μm $\times$ 0.4 μm with a vertical range of 0.4 μm are used. In tapping mode, the topographic images are taken using Si tip with a nominal tip radius of curvature of 5-10 nm. The resonant frequency and spring constant of the cantilever attached to the tip for tapping mode measurements are 200-400 kHz and 20-60 N/m, respectively.

Figure 3.16: Picture of ambient AFM instrument (Nanoscope-IV, Veeco).

WSxM software [173] has been used for AFM and STM image processing and analysis. The height difference correlation function $g(r)$, given in chapter 4, extracted from these image analysis, gives detail statistical information about the surface of nanolayer deposited on substrate from which growth mechanism can be extracted.

3.2.3 Scanning electron microscopy

A. Working principle:

SEM comes under the category of electron microscopes, which were developed due to the limitations associated with the light microscopes such as the magnification and resolution. The electron microscopes are scientific instruments that use a beam of highly energetic electrons to image the specimen on a very fine scale and to gain information about its structure and composition. The analysis of images obtained form the electron microscope can provide information on the topography, morphology, composition and the crystallographic orientation of the sample. There are two kinds of electron microscope namely transmission electron microscope (TEM) and SEM that are commonly used in the surface science. In our work, we have used SEM to characterize the surface morphology of the metal nanolayers.
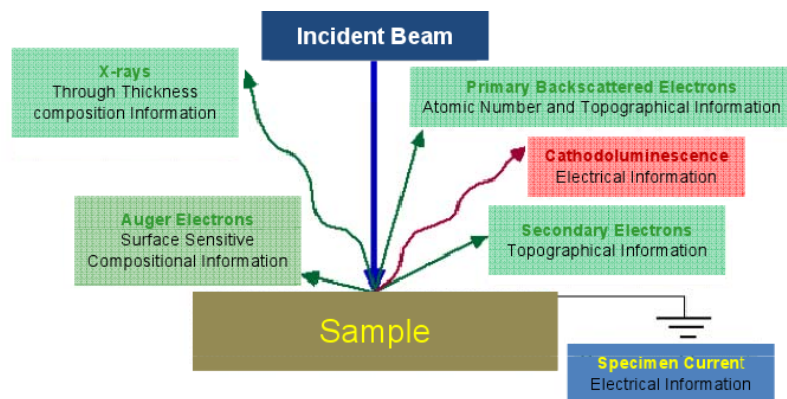
Figure 3.17: Schematic representation of electron beam-specimen interactions.
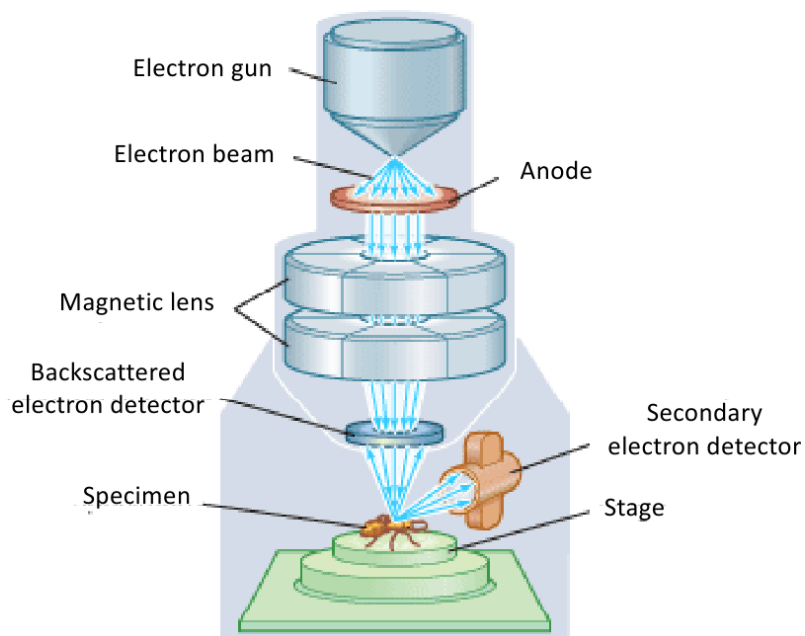
Figure 3.18: Schematic representation of the working principle of a SEM.

The first SEM was introduced in the year 1942 to study the structural aspects of the surface on a very fine scale. SEM uses the electron beam rather than light to form an image. The electromagnets are used to bend the electron beam to produce the image on a screen. By using the electromagnets, we can have more control over the magnification and the use of electron beam provides a greater clarity in the image produced. There are many advantages of using the SEM instead of a light microscope. The SEM has a large depth of field, which allows a large amount of the sample to be in focus at one time. The SEM also produces images of high resolution, which means that closely spaced features can be examined at a very high magnification. The combination of higher magnification, larger depth of focus, greater resolution, and ease of sample preparation makes the SEM one of the most extensively used instruments in research areas today. A beam of electrons is generated from the electron gun using tungsten tip located at the top of the column. This beam is attracted through the anode, condensed by a magnetic lens and focused as a very fine point on the sample by the objective lens. The scan coils are energized (by varying the voltage produced by the scan generator) and create a magnetic field, which deflects the beam back and forth in a controlled pattern. Once the beam hits the sample surface there are many possibilities that can occur by the interaction of electron beam with the surface, which are shown in the Fig. 3.17. As for as the SEM is concerned, when the electron beam hits the sample surface, the secondary electrons produced from the sample are collected by the secondary electron detector or the backscatter detector, which has been converted into a signal resulting in an image in the viewing screen. The working principle of a SEM is schematically shown in Fig. 3.18.

B. Instrument:

For imaging the sample surface 30 keV SEM (Quanta 200 FEG) was used as shown in Fig. 3.19. The range of accelerating voltage that can be applied varies from 200 V - 30 kV. Equipped with schottky emitter based field emission gun assembly which is optimized for high bright/high current a magnification of $12\times$ to $10^6\times$ can achieved.

Figure 3.19: Picture of a SEM instrument.

The Quanta 200 FEG can be operated in three vacuum modes for probing different types of samples:

(a) High vacuum (HV) mode (typically 10^{-5} mbar) for imaging and microanalysis of conductive and/or conventionally prepared metal coated specimens.

(b) Low vacuum (LV) mode (< 2 mbar) which can be used for imaging and microanalysis of non-conductive specimens without preparations.

(c) Environmental SEM (ESEM) mode (< 40 mbar), which is a typical mode for high vacuum incompatible specimens like biological samples.

In this setup four different detectors are deployed for imaging which includes a conventional Everhart-Thornley detector (ETD) with variable grid bias for HV mode, a third generation large-field gaseous secondary electron detector (LFD) for LV as well as ESEM mode which is mounted off-axis with enhanced gain preamplifier suitable also for use at low voltages and standard gaseous secondary electron detector (GSED) which is axially mounted and containing integrated second 500 μm pressure-

limiting aperture for operation up to 40 mbar for ESEM mode and the solid state detector (SSD). SSD is used to find out the material contrast i.e., Z (Z is the atomic number) contrast. In our study ETD is used to find out the morphology of all the samples and SSD is used in cross-sectional imaging of Au/Si system.

The sample mounting stage can be moved of 50 mm (max.) along X and Y directions and 25 mm (max.) along direction, with a sample tilt of $+75^o$ to -15° eccentric at analytical working distance of 10 mm. There is two types of sample holder, one is horizontal and another is vertical. Former one is used for the study of the top surface of the sample and the later one is to study the cross-section of the different interfaces of the sample.

Chapter 4

Au on passivated Si surface: Observation of interdiffusion

4.1 Introduction

The study of diffusion of Au into Si substrate has long standing interest in device fabrications [90]. Extensive work has been carried out at elevated temperatures [32; 33], mainly to enhance the diffusion, from which diffusion dynamics in the micron length scale is well established [132; 174; 175]. Also, a lot of work is on going to understand the role of surface binding and surface structure in the diffusion process. It is known that the presence of a native-oxide layer or the growth of an oxide layer [176; 177] at the interface strongly influences the interdiffusion behavior across a metal-semiconductor interface [94; 178]. It is also known that the oxide growth on Si surface could be hindered under non-UHV conditions by passivating the surface dangling bonds. The passivation of Si surface effectively blocks the oxide layer growth and accordingly helps in diffusion of overlayer Au film into Si substrate. These suggest that by doing the passivation, diffusion of Au into Si can

---

The work presented in this chapter is published in: Phys. Rev. B, **75**, 205411 (2007), Phys. Rev. B, **79**, 155405 (2009), Defect Diffus. Forum, **297**, 1133 (2010).

be controlled, which can also be used in the formation of control interdiffused layer. However, not much work has been carried out in this direction to study the initial interfacial role in the formation of thin Au-Si diffuse layer at room temperature, which is of immense interest not only to produce control diffused junctions in silicon at very shallow depth from the surface for the newly developed devices but also for the understanding of the morphological stability of the grown low-dimensional structures due to the diffusion even at room temperature [99; 172; 179; 180].

In this chapter, we have systematically investigated the role of passivating elements (such as H, Br and O) and the substrate surface crystallinity (such as $< 001 >$ and $< 111 >$) on the interdiffusion of Au overlayer into Si and also try to understand the main driving force behind the room temperature diffusion of Au into Si single crystal.

4.2 Passivation and crystalline orientation dependent interdiffusion

The stability of the Si surface after passivation with different materials (such as H, Br, O, etc.) can be different depending upon their bond strength and relative electronegativity. It indicates that the oxide growth rate of differently passivated Si surface can be different. Accordingly the diffusion of Au into Si passivated by different elements may be different.

Again the behavior of the interdiffusion of Au, may be different depending upon whether substrate is Si(001) or Si (111), as the stability of the passivated Si(111) surface may differ from that of Si(001) surface. Indeed, in some work, it have been shown that Br-passivated Si(111) surface is more stable compared to HF treated Si(111) surface [29; 30]. Also, the effects of passivation on Si(001) and Si(111) surfaces [29; 71; 75; 181] are likely to be different due to the difference in number of surface dangling bonds associated with each Si atom. So, what exactly happens,

when Au is deposited on differently passivated Si(001) and Si(111) surfaces, needs to be looked out properly.

4.2.1 Results and discussion

4.2.1.1 Interdiffused layer

XRR measurements of differently pretreated Si substrates as well as Au deposited films were carried out using the versatile x-ray diffractometer (VXRD) setup. X-ray reflectivity measurements of the Au deposited films were carried out as a function of time to see the interfacial evolution due to diffusion, which have been presented first, followed by the analysis. The time-dependent diffusion behavior is then predicted from the interdiffused layer estimated from the analyzed EDP.

I. X-ray reflectivity and electron density profile

Time evolution XRR data of three Au thin films deposited on Si(001) substrates are shown in Fig. 4.1, while that of three Au thin films deposited on Si(111) substrates are shown in Fig. 4.2. Kiessig fringes are evident in all the films, which are the signature of the total film thickness. Along with the Kiessig fringes, a modulation is also observed in the XRR profiles. Such modulation and their evolution with time are different for the films deposited on differently pretreated Si substrates. By monitoring the Kiessig fringes and the modulation one can readily get an idea about the changes in the film with time. There is very little change in the overall XRR profile of the Au/O-Si sample with time, which indicates that the film structure, especially the Au/Si interface structure of this sample, is stable, while changes in the reflectivity curves with time for the Au/Br-Si sample are slightly more obvious and that for the Au/H-Si) sample are significant. These give initial indication of large change in the Au/H-Si sample with time.

Best fit XRR profile along with the corresponding EDP are shown in Fig. 4.1 and Fig. 4.2. It is evident from the EDPs that all samples can be visualized as the composition of three regions, namely, top Au layer, interdiffused Au-Si layer, and
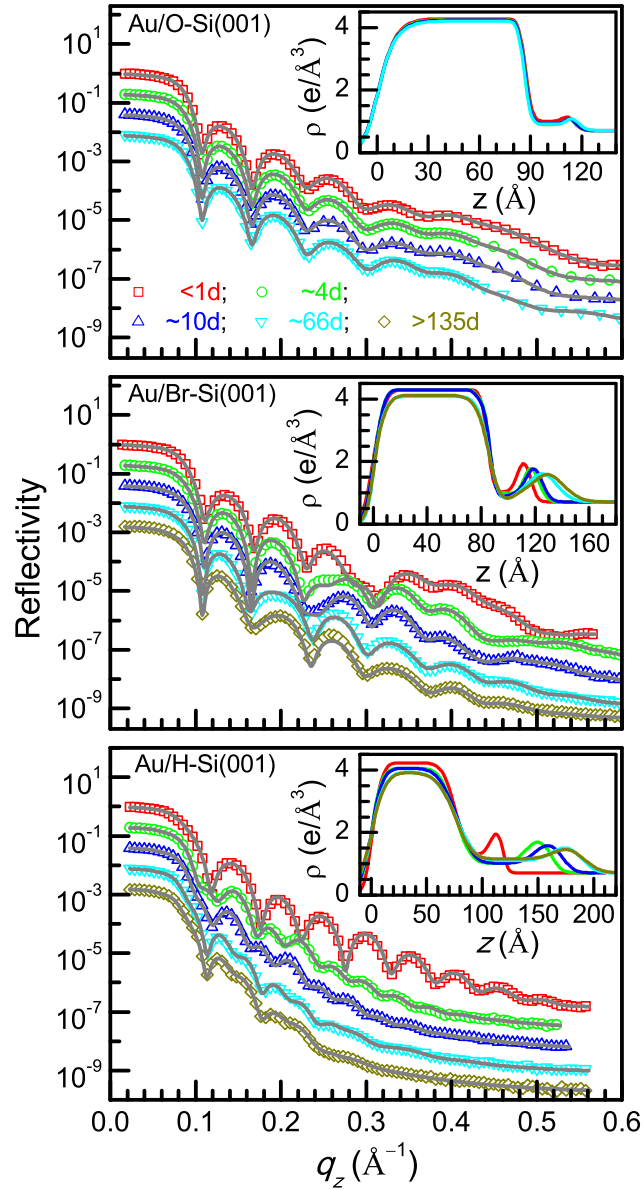
Figure 4.1: Time evolution XRR data (symbol) and analyzed curves (solid line) of Au thin films on three differently pretreated Si(001) substrates in three panels. In each panel, curves are shifted vertically for clarity. Inset: corresponding analyzed EDP. In legends, d indicates the time in day.
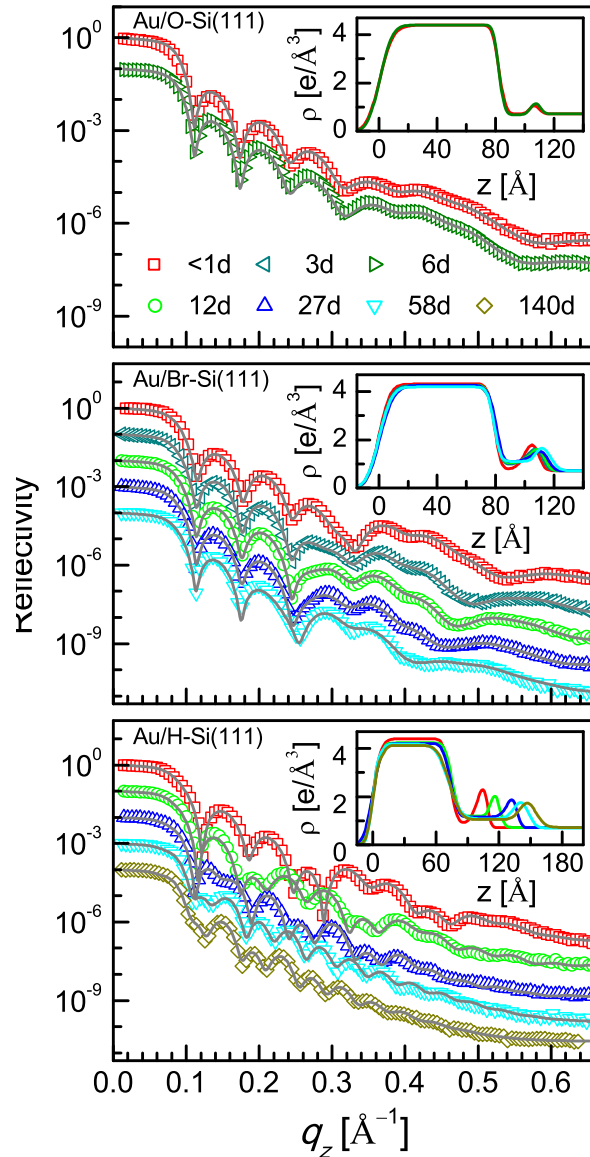
Figure 4.2: Time evolution normalized XRR data (different symbols and colors) and analyzed curves (solid line) of Au thin films on three differently pretreated Si(111) substrates in three panels. In each panel, curves are shifted vertically for clarity. Inset: corresponding analyzed EDP. In legends, d indicates the time in day.

Table 4.1: Parameters, such as the thickness (d), the electron density (ρ) and the top surface roughness (σ) of the Au thin films; the thickness (L) of the interdiffused layer and the decay time (τ), its distribution (β) and the fraction (f) of the active area through which diffusion takes place, for Au thin films on differently pretreated Si(001) substrates obtained from the analysis of the time evolution x-ray reflectivity data. Suffixs i and f represent parameters corresponding to the initial and final time of measurements, respectively.

Sample	d (nm)	ρ_i (e/Å³)	ρ_f (e/Å³)	σ_i (nm)	σ_f (nm)	L_i (nm)	L_f (nm)	τ (days)	β	f
Au/O-Si(001)	8.7±0.2	4.28±0.01	4.20±0.01	0.73	0.73	3.4	3.7	0.0[1]		1.0[1]
Au/Br-Si(001)	8.7±0.2	4.29±0.01	4.12±0.01	0.68	0.71	3.8	7.4	0.2±0.1	0.9	0.8±0.08
Au/H-Si(001)	8.0±0.2	4.24±0.01	3.92±0.01	0.65	0.96	4.8	13.5	4.5±0.5	0.9	0.9±0.05

[a]Nearly covered oxide layer in this Si surface is present from the beginning.

Table 4.2: Parameters, such as the thickness (d), the electron density (ρ), the top surface roughness (σ) and the interface roughness (σ_{in}) of the Au thin films; the thickness (L) of the interdiffused layer; the growth time (τ) and its distribution (β) for the interface of fraction (f) where oxide grow with time, for Au thin films on differently pretreated Si(111) substrates obtained from the analysis of the time evolution x-ray reflectivity data. Suffixs i and f represent parameters corresponding to the initial and final time of measurements, respectively.

Sample	d [nm]	ρ_i [$e.\text{Å}^{-3}$]	ρ_f [$e.\text{Å}^{-3}$]	σ [nm]	$\sigma_{in,i}$ [nm]	$\sigma_{in,f}$ [nm]	L_i [nm]	L_f [nm]	M_0 [$e.\text{Å}^{-2}$]	τ [day]	β	f
Au/O-Si(111)	8.0±0.2	4.40±0.03	4.40±0.03	0.7	0.3	0.3	2.9	3.0	9			
Au/Br-Si(111)	8.0±0.2	4.32±0.03	4.19±0.03	0.6	0.4	0.4	3.6	4.6	18	2±0.3	0.7	0.8±0.1
Au/H-Si(111)	8.0±0.2	4.39±0.03	4.13±0.03	0.6	0.5	0.8	4.0	9.4	31	5±0.5	0.7	0.8±0.1

unmodified Si substrate. The thickness of the top layer (d) of each film remains almost the same with time, while that of the interdiffused layer (L) is different for different samples. The change in the interdiffused layer is compensated by the change in the electron density (ρ) and/or surface roughness (σ) of the top Au layer. The parameters obtained from the reflectivity analysis are listed in Table 4.1 and Table 4.2, where subscripts i and f represent parameters corresponding to the initial and final time of measurements, respectively. It can be noted from the EDP that, for the Au/O-Si(001) and Au/O-Si(111) samples, there is very small diffusion of Au at the beginning, which is likely to be through the porous oxide region (the slightly low electron density of the oxide layer usually observed raised the possibility) and then remains almost unchanged (L changes from 3.4 to 3.7 nm for Au/O-Si(001) and from 2.9 to 3.0 nm for Au/O-Si(111)). For the Au/Br-Si(001) and Au/Br-Si(111) samples, the diffusion is more evident (L changes from 3.8 to 7.4 nm for Au/O-Si(001) and from 3.6 to 4.6 nm for Au/O-Si(111)) compared to that for the Au/O-Si(001) and Au/O-Si(111) samples, while for the Au/H-Si(001) and Au/H-Si(111) samples, the diffusion seems to be appreciable (L changes from 4.8 to 13.5 nm for Au/O-Si(001) and from 4.0 to 9.4 nm for Au/O-Si(111)).

II. Interdiffusion: Time dependence

In order to understand the time-dependent diffusion of Au, the diffused amount (M) has been calculated from the interdiffused layer, subtracting the Si contribution. Parameters M and L are then plotted as a function of time (t) in Fig. 4.3 for the Au/Br-Si(001) and Au/H-Si(001) samples. Similar type of time dependence is observed for both parameters. The variation of M with time (t) for the Au/Br-Si(111) and Au/H-Si(111) samples are shown in Fig. 4.4 along with the Au/Br-Si(001) and Au/H-Si(001) samples for comparison. It is known that for random symmetric diffusion, the diffused amount follows

$$M(t) = M_0 + \Delta M t^{1/2} \tag{4.1}$$
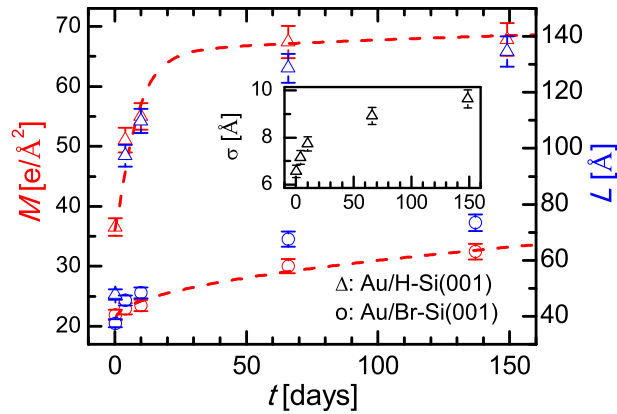
Figure 4.3: The diffused amount (M) and the diffusion length (L) of Au in the differently pretreated Si(001) substrates as a function of time. Dashed lines through M data are the analyzed curves using Eq. 4.2. Inset: evolution of the surface roughness (σ) with time for the Au/H-Si(001) sample. An error bar has been incorporated for each data.
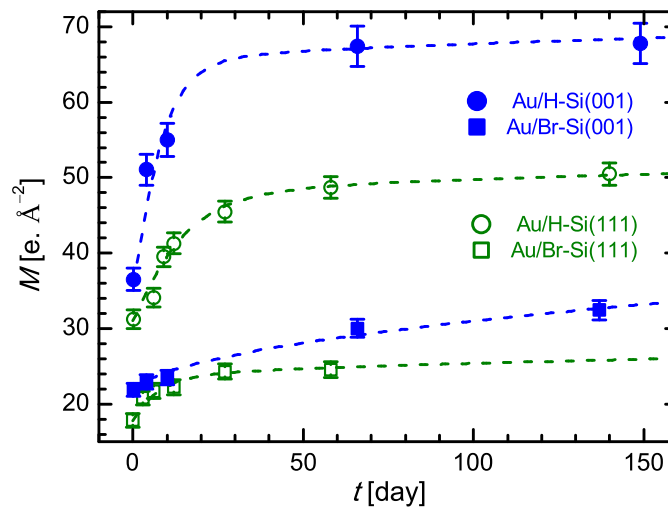
Figure 4.4: The diffused amount of Au into the differently pretreated Si(111) and Si(001) substrates as a function of time. Dashed lines through the data are the analyzed curves using Eq. 4.2. An error bar has been incorporated for each data.

where M_0 and ΔM are time independent constants. Strong deviation from the Fickian $t^{1/2}$ dependence is observed in Fig. 4.3 for M. This dependency becomes gradually weaker with time, which is similar to that of jamming or entanglement effect as observed in soft materials (such as polymer) for asymmetric diffusion [182–184]. Such asymmetric diffusion is quite unlikely in our present system, while it is likely that due to the instability of the passivated Si surface some layer (presumably oxide layer) will grow with time through which further diffusion will be blocked. This essentially means that ΔM ($\propto D$, where $D = D_0 e^{-E/kT}$) is not independent of time. The dependency has been incorporated in the following way. First, we have divided the interfacial area into two fractions: f, where oxide will grow with time, and the rest, $(1\text{-}f)$, where oxide will never grow; that is, where Si surface will remain passivated. The contribution from $(1\text{-}f)$ fraction is simple Fickian type through constant area, while that from f fraction changes continuously. If we assume that due to the growth of this oxide layer, the active area, through which diffusion takes place, decreases exponentially as $e^{-(t/\tau)^\beta}$, then the contribution needs to be calculated by considering the average effective area responsible for diffusion up to a certain time, that is, through integration. The diffused amount, in total, can be expressed as

$$M(t) = M_0 + \Delta M' \left[f \int_0^t e^{-(t'/\tau)^\beta} t'^{1/2} dt' + (1 - f)\, t^{1/2} \right] \tag{4.2}$$

where $\Delta M'$ is now a time-independent constant, τ is a measure of growth time of the blocking layer, which is also related to the stability of the passivated surface, and β is a stretched exponent. β becomes 1 for single growth time, while deviation from 1 indicates the distribution of growth time. It can be noted here that Eq. 4.2 is quite general in the sense that for $f = 0$, it becomes Fickian-type diffusion, while it can be used equally well for $f = 1$, when all the interface acts as a blocking layer. Also, it gives good insight about the growth of the blocking (oxide) layer through τ.

Eq. 4.2 has been used to analyze the time-dependent M for the Au/Br-Si(001) and Au/H-Si(001) samples. The analyzed curves are shown in Fig. 4.3 and the corresponding parameters are listed in Table 4.1. It can be noted that for both samples,

the blocking layer grows in the major portion (large f value) of the Si surface. Also, for both samples, small but similar distribution ($\beta = 0.9$) of τ exists. The value of τ, on the other hand, differs considerably. Even though a large error is possible in the estimation of τ, there is no doubt that $\tau_{Au/O-Si(001)} \ll \tau_{Au/Br-Si(001)} \ll \tau_{Au/H-Si(001)}$; that is, the strong role of surface pretreatment conditions in the growth of the blocking layer even in the presence of Au at room temperature. Large value of τ, for the Au/H-Si(001) sample, indicates that the Si surface for this sample remains passivated for a longer time, for which large diffusion takes place. It is quite evident that the changes in the density (which is proportional to the electron density) of the Au film and the top surface roughness are due to this diffusion. The variation of the top surface roughness with time is presented in the inset of Fig. 4.3, which shows a monotonic increase similar to that of the mass diffusion.

The time-dependent interdiffusion for the Au/Br-Si(111) and Au/H-Si(111) samples has been analyzed using Eq. 4.2. The analyzed curves are shown in Fig. 4.4 and the corresponding parameters are listed in Table 4.2. Analysis suggests that the blocking layer grows in the major portion ($f \approx 0.8$) of the Si surface having distribution ($\beta \approx 0.7$) of growth time for both the samples. While, the value of τ for the Au/Br-Si(111) sample is found less than that for the Au/H-Si(111) sample indicating that the Si surface for the latter sample remains passivated for a longer time, for which large diffusion takes place. Values of M_0, suggest that large diffusion during deposition in the Au/H-Si(111) sample compared to that of the Au/Br-Si(111) sample. This is likely to be related to the higher stability of the H-Si(111) surface compared to that of the Br-Si(111) surface and/or also to the smaller size of H atom compared to that of Br atom. Similar effect is also observed in the Au/Si(001) system. The value of τ for the Au/Br-Si(111) sample is large (about one order) compared to that for the Au/Br-Si(001) sample, while those for the Au/H-Si(111) and Au/H-Si(001) samples are almost same. The possible mechanism behind such dependence has been discussed later.
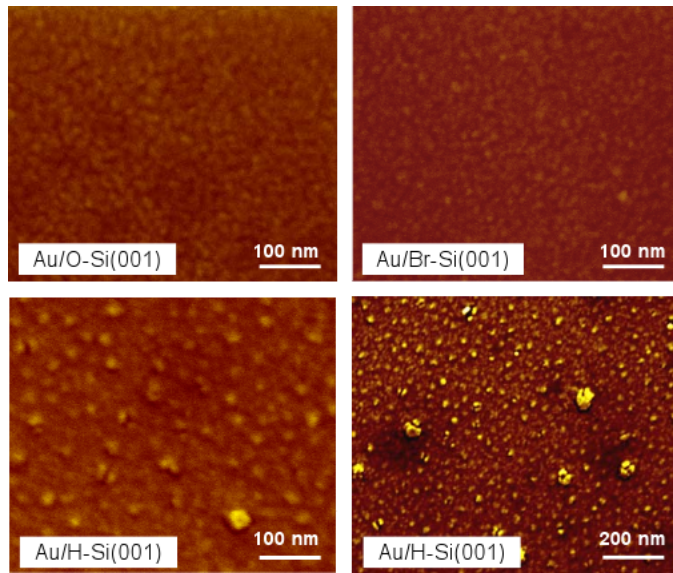
Figure 4.5: SEM images of Au thin films on differently pretreated Si(001) substrates after prolonged diffusion.

4.2.1.2 Topography

So far, we have discussed the time evolution of the density profiles, which provide changes in the interfacial region due to diffusion. Now, we present SEM and AFM results and discuss about the topography after diffusion. Large-scale near-top surface features of the Au films on differently pretreated Si substrates, evolved after prolonged diffusion at room temperature, were first imaged by SEM. The detailed top surface morphology of the same films were then mapped through AFM in different length scales (50-1000 nm) and in different portions of the samples. AFM images were collected in non-contact mode and in UHV (10^{-9} mbar) conditions to get less disturbed and clean images, respectively.

I. Scanning electron microscopy:

SEM images of three Au thin films, after prolonged diffusion, are shown in Fig. 4.5.
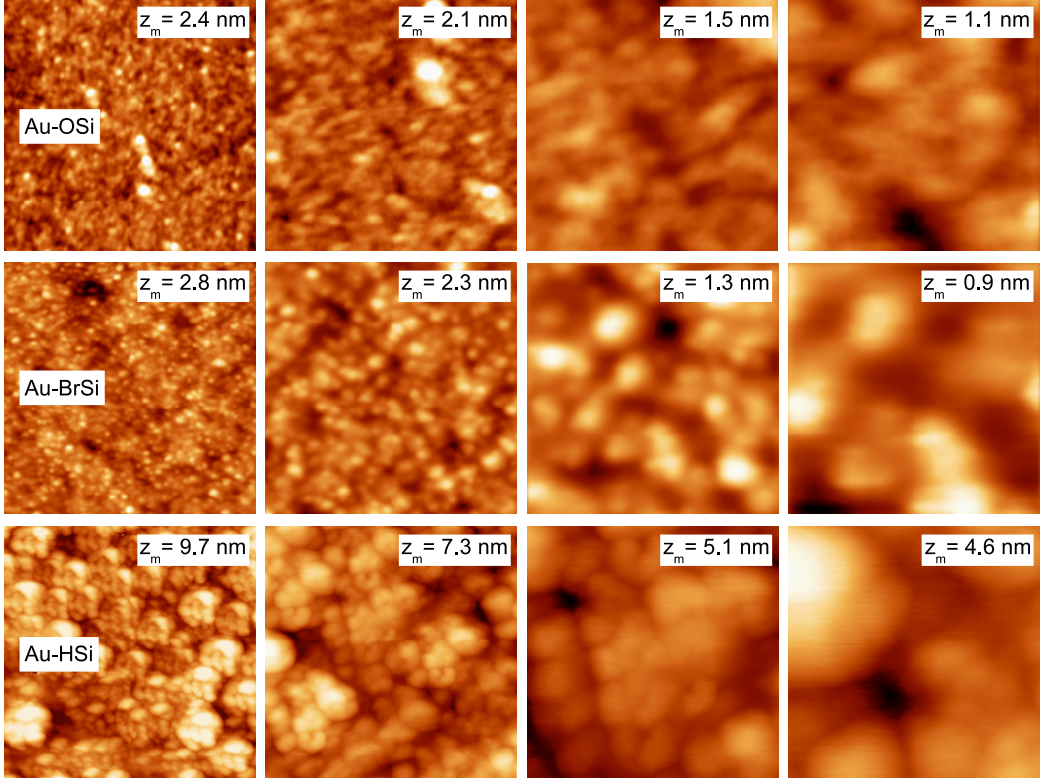
Figure 4.6: AFM images of Au thin films on differently pretreated Si substrates after prolonged diffusion, in four length scales (1000, 500, 200, and 100 nm from left to right). Maximum height variation is indicated by z_m.

Compact domain like features have been observed in all sample surfaces. However, for the Au/O-Si(001) and Au/Br-Si(001) samples, the contrast is low, while for the Au/H-Si(001) sample, the contrast is strong, which is also evident from the additional low magnification image presented in Fig. 4.5. Considering a single material (Au), such contrast can be primarily associated with the topography and correspondingly, it can be inferred that the height variation of the surface of the first two samples is quite less compared to that of the latter one. The height variation has been verified by actual topography measurements through AFM, as will be discussed in the next section.
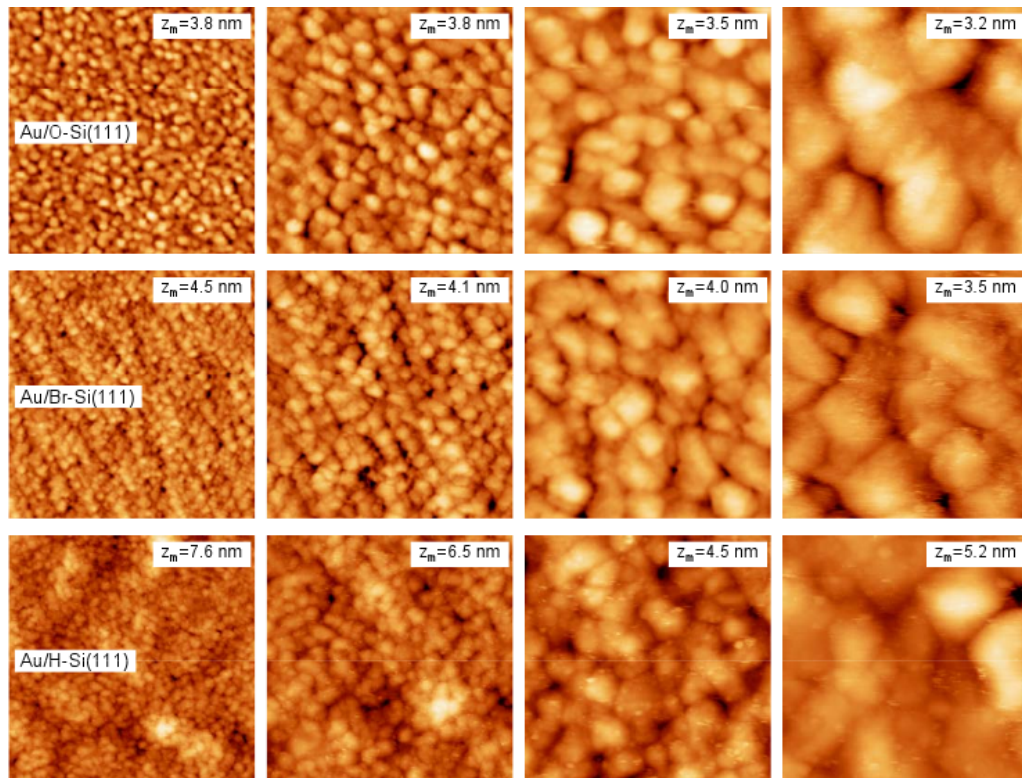
Figure 4.7: STM images showing topography (z_m indicates maximum height variation) of Au thin films on differently pretreated Si(111) substrates after prolonged diffusion, in four (560, 320, 160, and 80 nm from left to right) length scales.

Table 4.3: Parameters, such as the domain size (R_D), the surface height variation (h_{pv}), the saturation surface roughness (σ_0), the correlation length (ξ) and the scaling exponent (α), of the Au thin films on differently pretreated Si(001) substrates obtained from the analysis of the AFM images.

Sample	h_{pv} (nm)	σ_0 (nm)	R_D (nm)	ξ (nm)	α
Au/O-Si(001)	2.4±0.2	0.21	25±4	26±3	0.86
Au/Br-Si(001)	2.8±0.2	0.30	25±3	25±3	0.91
Au/H-Si(001)	9.8±0.3	2.00	27±4	40±4	0.91

II. Atomic force microscopy and height-height correlation:

The AFM images of the same Au thin films are shown in Fig. 4.6. Domain-like structures of similar size (R_D) are evident on the top surface, which is the basic nature of the Au film growth on Si surface [55]. However, the height variation (h_{pv}) is different in different films, which is listed in Table 4.3 along with R_D. Height fluctuation of the Au/H-Si(001) sample is very high compared to other samples, which can be associated with the fluctuation between accumulated domains due to large diffusion. Typical STM images, showing topography of Au/O-Si(111), Au/Br-Si(111) and Au/H-Si(111) samples after prolonged diffusion are shown in Fig. 4.7. It can be noted that all films are composed of small islands of similar size. Additional modulation is observed above that, which is prominent for the Au/H-Si(111) sample. The size (R_D) of the islands and the height-variation (h_{pv}) in different films are listed in Table 4.4. It can be noted that the island-like topography of the Au/Si(111) system in general and prominent modulation above it for the H-passivated sample are similar to those of the Au/Si(001) system.

A surface can be analyzed quantitatively by height-height (difference) correlation function of the following form [55; 185; 186]:

$$g(r) = \left\langle (h(r_0 + r) - h(r_0))^2 \right\rangle , \tag{4.3}$$
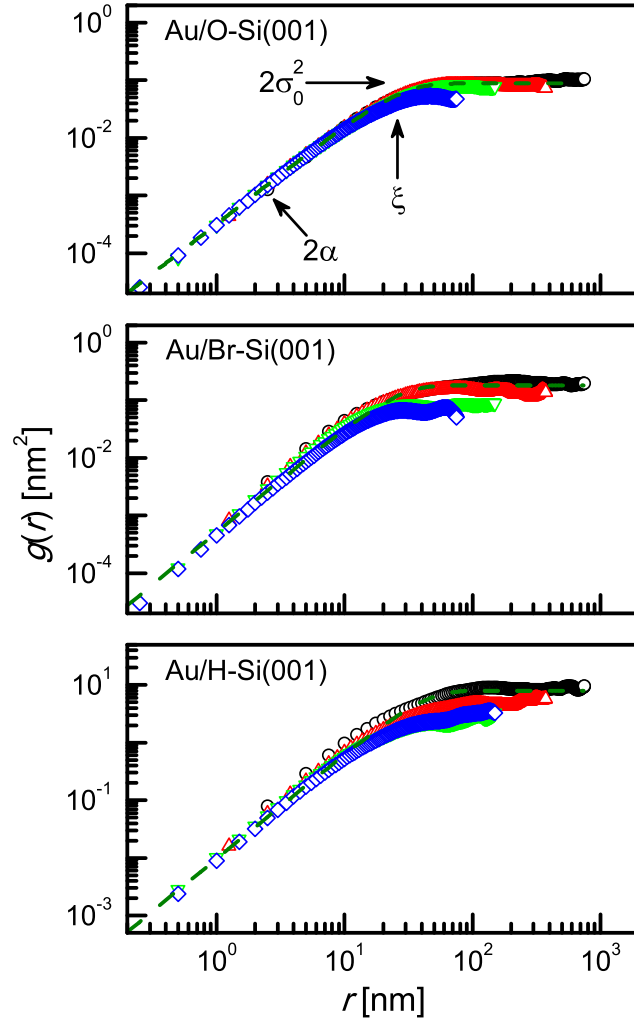
Figure 4.8: Height-height correlation obtained from AFM images of Au films on differently pretreated Si substrates after prolonged diffusion in different panels. The symbols represent the data estimated from AFM images of different scan sizes, while the dashed lines are the fits corresponding to Eq. 4.4. Different parameters associated with the height-height correlation function are indicated by arrows for clarity.

93
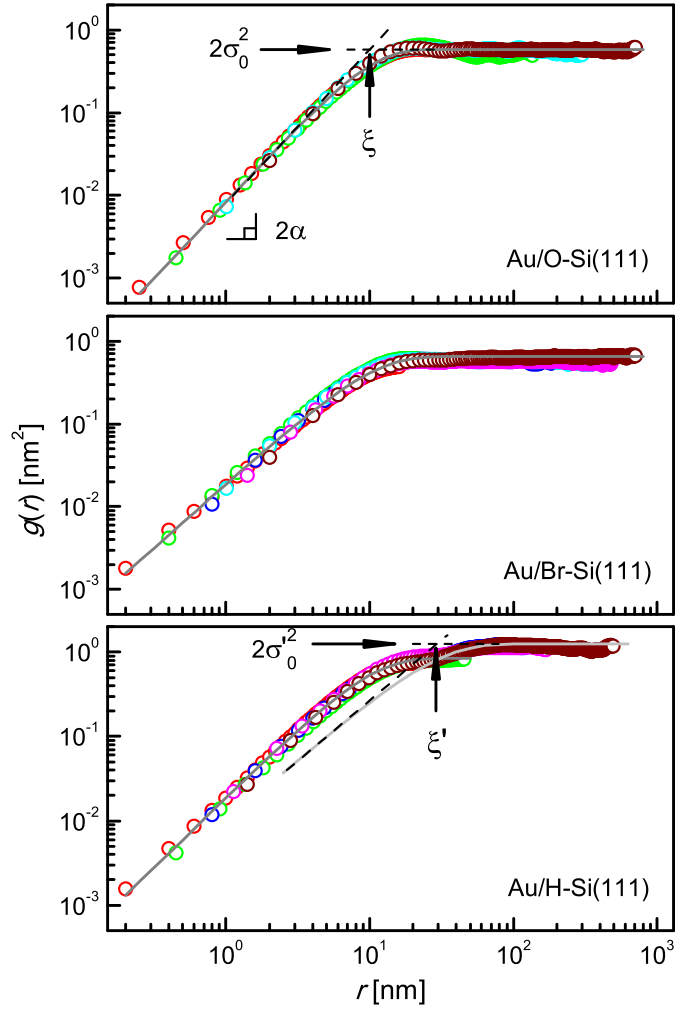
Figure 4.9: Height-height correlation obtained from STM images of Au films on differently pretreated Si(111) substrates after prolonged diffusion in different panels. The symbols represent the data estimated from STM images of different scan sizes, while the solid lines are the fits corresponding to Eq. 4.4. Different parameters associated with the height-height correlation function are indicated by arrows for clarity.

Table 4.4: Parameters, such as the island size (R_D), the surface height variation (h_{pv}), the saturation surface roughness (σ_0), the correlation length (ξ) and the scaling exponent (α), of the Au thin films on differently pretreated Si(111) substrates obtained from the analysis of the STM images.

Sample	h_{pv} [nm]	R_D [nm]	ξ (ξ') [nm]	σ_0 (σ_0') [nm]	α (α')
Au/O-Si(111)	3.9±0.3	18±3	10	0.54	0.92
Au/Br-Si(111)	4.8±0.4	17±4	10	0.57	0.77
Au/H-Si(111)	7.8±0.5	16±4	10 (28)	0.65 (0.79)	0.82 (0.73)

where $h(r_0 + r)$ is the height of the surface at relative position r and $h(r_0)$ is the mean surface height. Eq. 4.3 has been used to calculate statistically meaningful $g(r)$ from the AFM images. Nearly linear increase up to a certain length scale followed by saturation is observed in all the curves. The length scale where the bending is observed, the slope, and the saturation value are the measures of the surface and need to be estimated quantitatively.

It is known that the height-height correlation function, for the kinetic rough surface, follows [55; 185]:

$$g(r) = 2\sigma_0^2 \left[1 - e^{-(r/\xi)^{2\alpha}}\right], \tag{4.4}$$

where σ_0 is the saturation roughness, ξ is the correlation length and α is the scaling exponent of the surface. The height-height correlation data of the different modified surfaces have been fitted using Eq. 4.4 and are presented in Fig. 4.8 and Fig. 4.9. The different parameters obtained from the analysis are listed in Table 4.3 and Table 4.4. It can be noted that the scaling exponent is quite high for all the films even after diffusion for a prolonged time, indicative of in-plane diffusion dominated growth as has been observed before in the initial stage [55]. On the other hand, the values of other parameters listed in Table 4.3 for the Au/H-Si(001) sample are large
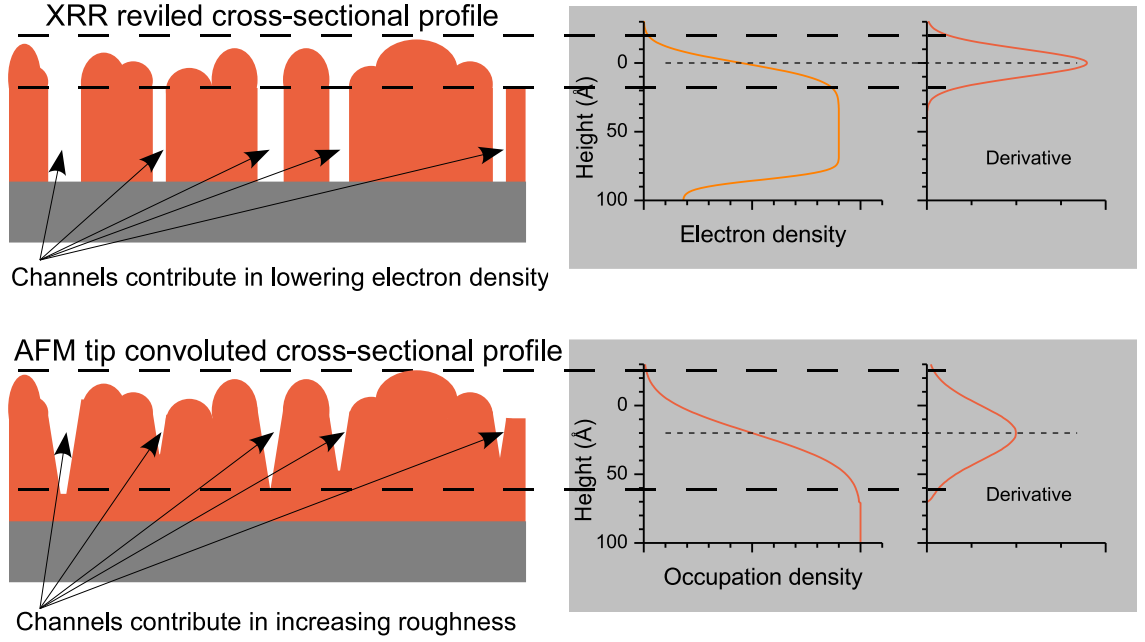
Figure 4.10: Schematic presentation of the discrepancy between the XRR and AFM results of Au films deposited on the Si substrates.

compared to other samples. This can be understood in the following way. In the Au/H-Si(001) sample, there are some portions (channels) regularly distributed from where the entire Au layer has been diffused. The distribution of channels is reflected in ξ value, while the fact that almost the entire layer has been diffused in some portion is reflected in the values of h_{pv} and σ_0. In can also be noted that the value of σ_0 of this film is quite high when compared to the value of σ_f of Table 4.1. This is because of those channels in the film shown in Fig. 4.10, which mostly appear as a decrease in the electron density in the x-ray reflectivity data analysis, while appearing as high roughness in the AFM measurements due to the convolution with the tip.

For the Au/H-Si(111) sample, fitting has been made, considering two separate regions (length-scales), as shown in Fig. 4.8. Each region has been fitted with a set of parameters. The different parameters obtained from the analysis are listed in Table 4.4. The parameters obtained from the large length-scale data, for the

Au/H-Si(111) sample, are indicated by prime ($'$). It can be noted that the value of ξ for all samples are almost same and is less than that of R_D. This implies that the value of ξ is determined by the height-fluctuation within islands. On the other hand, the value of ξ', for the Au/H-Si(111) sample, is larger than that of R_D and is related to the island-island fluctuation due to strong interdiffusion through interface having non-uniform blocking layer (as considered in Eq. 4.2 through β and f parameters), which is also evident directly from the topography. Small, but similar value of σ_0 for all samples and slightly larger value of σ_0' for the Au/H-Si(111) sample are also consistent with the previous argument. Large value of the scaling exponent ($\alpha \approx 0.9$), for the Au/O-Si(111) sample, indicates in-plane diffusion dominated growth [55]. However, slight lower value of that parameter, for the Au/Br-Si(111) sample, can be attributed to the small interdiffusion. For the Au/H-Si(111) sample, both effects can be seen separately. Large value of α is associated with the normal in-plane diffusion dominated growth, while comparatively small value of α' is associated with the strong interdiffusion. It is clear from the analysis that the behavior of Au/Si(111) system is similar to that of Au/Si(001) system. However, for the Au/Si(111) system, the values of R_D and ξ for all the samples are relatively small, while the values of h_{pv} and σ_0 for Au/O-Si(111) and Au/Br-Si(111) samples are relatively large. These can be attributed to the high-resolution of STM mode over AFM. Also, due to this high-resolution, two distinct correlation lengths (ξ and ξ') are observed in the Au/H-Si(111) sample, which was however, smeared out in the Au/H-Si(001) sample, to give one large value.

4.2.1.3 Role of passivation in interdiffusion

Let us now try to understand the reason behind the observed difference in the diffused amount of Au in three differently passivated Si substrates and the mechanism for the formation of a controlled interdiffused layer. For the Au/O-Si samples, a native-oxide layer was present from the beginning, which prevents Au diffusion into Si. The very small amount of Au that is observed in Si is diffused through the pores,

which are likely to be present in the oxide layer. For the Au/H-Si samples, the initial oxide layer of the Si surface was etched off by HF (strong electronegativity of F helps in such process) and makes surface H-passivated [71]. It is known that the Si surface passivated with H is not stable, and the oxide layer tried to grow with time. In this case, the strong electronegativity of largely available O (listed in Table 2.1), helps in replacing the passivating elements. To overcome that, Si surface was further passivated with Br in the Au/Br-Si samples. Relatively strong electronegativity (tabulated in Table 2.1) of Br helps to replace the H. However, it has been observed that the surface passivated with Br is less stable compared to that passivated with H only. Although it is apparently surprising, it is known that for Si(001) surface, there are two dangling bonds on each Si atom which need to be saturated [71]. For Br passivation, two Br atoms try to saturate two adjacent dangling bonds of a Si atom, inclined toward each other. However, the size of the Br atom is big such that it is difficult to accommodate both Br atoms in adjacent positions (shown in Fig. 2.7), which makes such a structure unstable. On the other hand, for the small size of H atom such spacial problem does not arise, which makes the H-passivated Si(001) surface more stable than the Br-passivated Si(001) surface. It is then quite evident that the simple passivation in different ways (as demonstrated here) can tune the growth of the oxide layer on the Si surface even in the presence of a thin Au film, which in turn can control the formation of an interdiffused nanolayer. This, in general, implies that by changing the surface stability, the interdiffusion can be controlled at room temperature.

4.2.1.4   Role of crystalline orientation of the substrate in interdiffusion

The fact that the results of the present Au/Si(111) system are qualitatively similar to those of the Au/Si(001) system, is something not expected. Our understanding from the literature [29; 30] was that the Br-treated Si(111) surface is stable compared to that of the HF-treated Si(111) surface. However, present study clearly suggest otherwise, which is interesting and needs justification. In order to understand the
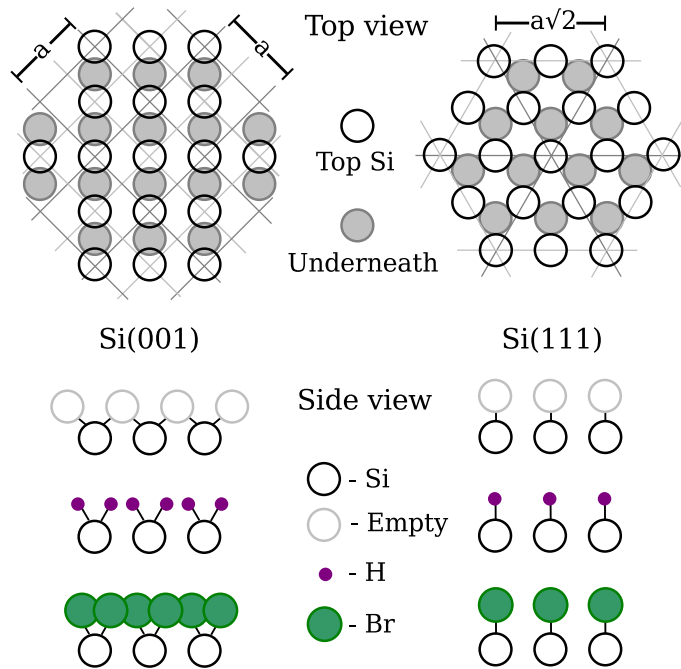
Figure 4.11: Schematic view of bulk terminated Si(001) and Si(111) surfaces with 'a' as lattice constant. Top view: In-plane positon of Si atoms and open space on the surface. Side view: Dangling bonds on the Si surface after removable of Si atoms (empty) and passivation of those with H and Br atoms, considering one to one saturation.

observed differences (both qualitative and quantitative) in the interfacial stability and the interdiffusion of the Au/X-Si(111) samples for different passivated materials X (such as O, Br and H) and compared those with the Au/X-Si(001) samples, schematic view of the bulk terminated Si(001) and Si(111) surfaces have been shown in Fig. 4.11. Top view shows the in-plane positions of the top Si atoms and just underneath [187]. This gives an idea about the open space in the top layer. As the density of atoms on the Si(111) surface is more ($2/\sqrt{3}$ times) than that on the Si(001) surface [188], the open space in the latter is more which can provide larger diffusion. On the other hand, side view shows that the number of dangling bonds associated with each surface atoms are different in two Si surfaces. Passivation of those dangling bonds with different materials and their stability not only depends on the relative electronegativity and bond-energy (D) with Si, but also on the atomic size (R_a). Values of such parameters, obtained from the online sites [69; 70], are listed in Table 2.1. Small size H atoms can passivate both the surfaces without facing any spatial problem. However, same is not true for the passivation with Br. Big size Br atoms are impossible to accommodate side-by-side to saturate two dangling bonds of each Si atom on the Si(001) surface. For the Si(111) surface, where one dangling bond is associated with each Si atom, such size is not a problem.

The size of Br atoms hinder such passivation (steric hindrance) on Si(001) surface making it unstable, as observed in low τ value. Such problem do not arise for Si(111) surface, which provide comparatively large τ value. However, if we consider the value of bond-energy and bond-length of H and Br with Si then it is obvious that dissociation of H is difficult compared to Br, which is clearly evident from the corresponding τ values. Large diffusion, as obtained from both initial and final value of M, into the Si(001) sample compared to that into the Si(111) sample, especially through the H-passivated surface, is related to the openness in their surface structure. While for both Au/Si(001) and Au/Si(111) systems, the values of M_0 in the H-passivated samples are more (about 1.7 times) than those in the Br-passivated one and can be attributed to the large barrier against diffusion of the Br-passivated surface, arising from large-size Br atoms and larger instability of the surface.

4.3 Driving force of room-temperature diffusion

So far we have seen that the interdiffused Au nanolayer is moving into the Si as a whole. The question is - do we understand the process responsible for that observed wave-like diffusion behavior? In order to find out the reason behind such peculiar behavior we have performed further studies using H-Si surface where enhanced interdiffusion has been observed.

To see the evolution of EDP, XRR data for one set of samples were collected as a function of time after keeping that set at ambient conditions, while for other set of samples; XRR data have been collected just before and after the samples were in UHV condition. It is necessary to mention that some time is always required to attend the UHV condition from ambient condition or visa-a-visa, during transfer into the chamber or when taking out of it. Also to separate out the effect of oxygen and atmospheric pressure on diffusion, XRR measurements have been carried out for another set of samples after keeping those samples for different duration in nitrogen environment having similar atmospheric pressure. Slightly enhanced diffusion in nitrogen environment has been observed compared to ambient conditions.

The topography of the Au nanolayers at different stages of interdiffusion at ambient conditions, were mapped through AFM in different length scales (50-1000 nm) to get statistically meaningful information. AFM images were collected in non-contact mode and in UHV conditions to get high-resolution stable and clean images.

4.3.1 Results and discussion

The evolution of XRR data for the Au/Si system under ambient and UHV conditions are shown in Fig. 4.12(a). Corresponding EDP are shown in Fig. 4.12(b). Formation of broad diffused nanolayer is evident from the EDP. Such layer shows movement with time when it is in ambient condition, while remains almost static when it is in UHV condition. The evolution of topography due to strong interdiffusion has been observed from AFM images. Typical time-evolution AFM images are shown in Fig. 4.13(a) and (b). Corresponding height-histogram and coverage as a function
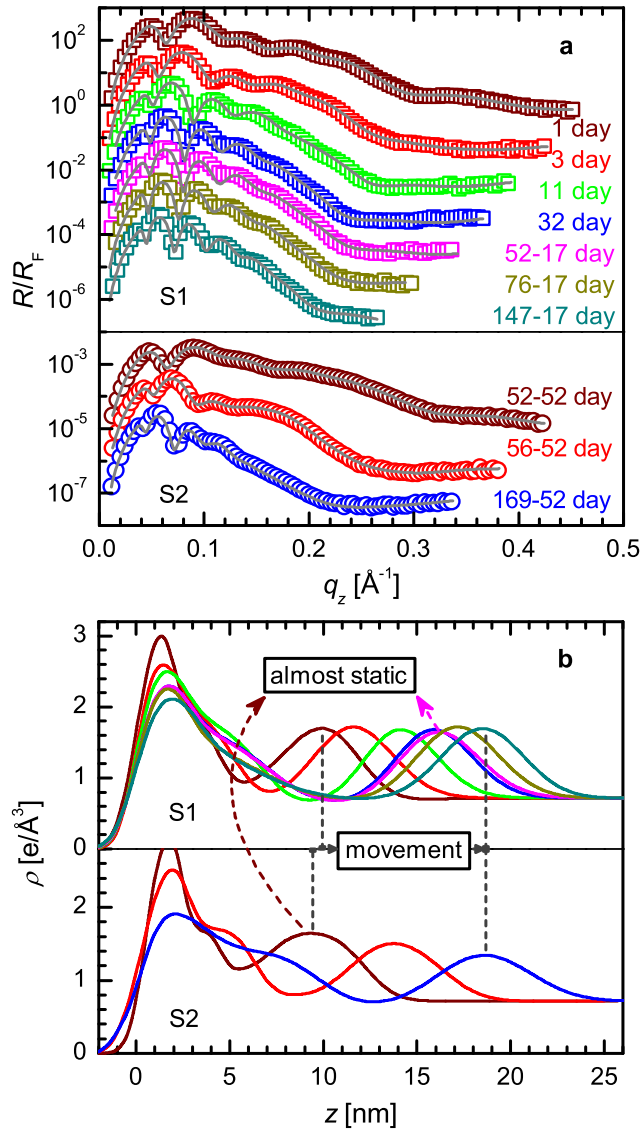
Figure 4.12: (a) Time-evolution (in different colors) normalized XRR data (in symbols) and analyzed curves (in solid lines) for two similar samples (S1 and S2). Both samples were mostly in ambient conditions (namely, in atmospheric pressure), except, sample S1 was in UHV for about 17 days (from day 35 to day 52), while sample S2 was in UHV for about 52 days (from day 0 to day 52). Curves are shifted vertically for clarity. Kiessig fringes in the curves move towards left with time in presence of atmospheric pressure, indicative of increase of thickness. (b) Corresponding time-evolution (indicated through same color) EDPs for two samples. Movement of the diffused layer inside silicon with time is evident in presence of atmospheric pressure.
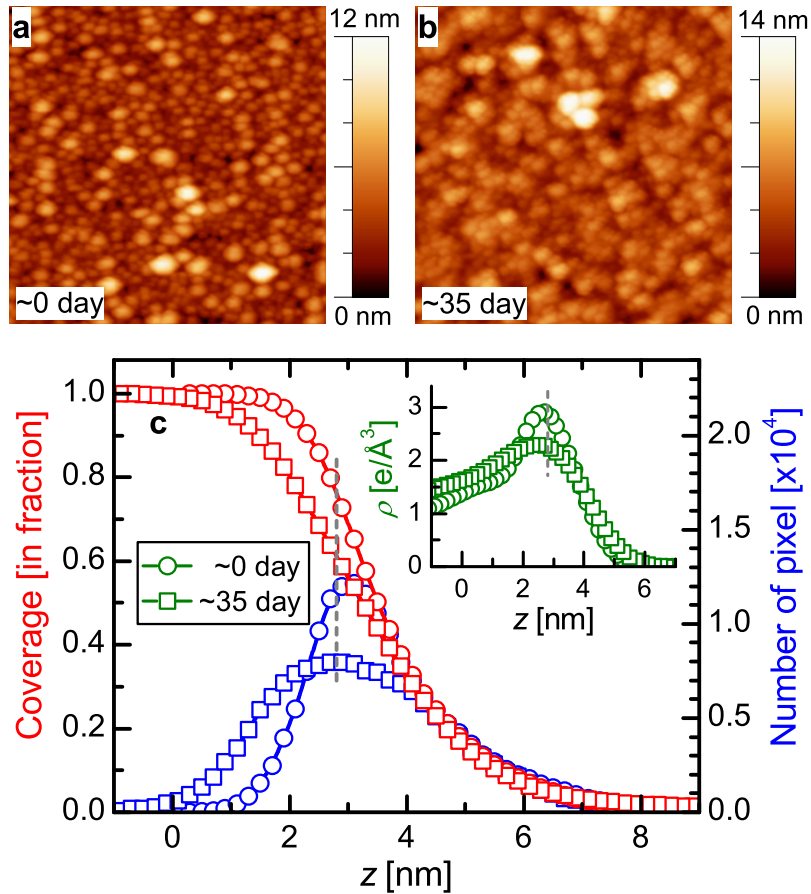
Figure 4.13: Typical AFM images (of scan size 800×800 nm^2) showing topography (a) almost after deposition and (b) after diffusion at atmospheric pressure for about 35 days. (c) Corresponding height-histogram and coverage as a function of height. Coverage at a given height (indicated by a dashed line, for example) decreases with time due to diffusion of gold into silicon, consistent with the EDP (and corresponding dashed line) shown in the inset.

of height are shown in Fig. 4.13(c). Variation of coverage with time obtained from AFM images is consistent with the change in the corresponding EDP shown in the inset of Fig. 4.13(c).

In order to understand the diffusion behavior, diffusion length (L), obtained from the EDP, is plotted in Fig. 4.14(a) as a function of time. It is clear from Fig. 4.14(a) that L changes with time monotonically when it is under ambient condition and deviates from that behavior when it is under UHV condition. It is also clear that if we ignore the time during which the sample is under UHV condition, then considering modified time, the value of L almost falls into that ambient condition curve. The monotonic variation of L, however, does not follow $t^{1/2}$ dependence, which is clearly evident from Fig. 4.14(b). Also the diffusivity (D) plotted against L in the inset of Fig. 4.14(b) shows that D deviates from constant value. In fact, D decreases with length.

The relation between D and the activation energy for a particular diffusion process is expressed in Eq. 2.15. If the value of D is sufficient then it is expected to observe diffusion and considering random symmetric diffusion (i.e. D is independent of both time and space), the diffused amount should follow Fick's law. However, strong deviation from the Fickian $t^{1/2}$ dependence [189] is observed in the Au/Si system [43]. The deviation has been well understood considering the growth of blocking oxide layer at the interface with time, assuming D is sufficiently large to observe the diffusion. The growth of oxide layer at the interface, which takes place due to the presence of oxygen at ambient condition, blocks the diffusion. Accordingly, it was expected that, if one can prevent or slow down the oxide growth at the interface (namely by placing the system at UHV condition) then diffusion should enhance. However, with surprise we observed quite contrary, namely, diffusion and/or movement of diffused layer when the system is in ambient condition, while almost no diffusion or stagnation of diffused layer, when it is in UHV condition (Figs. 4.12 and 4.14). These simple observations suggest that the assumption, D is sufficiently large to observe the diffusion, is not correct and open up fundamental question regarding
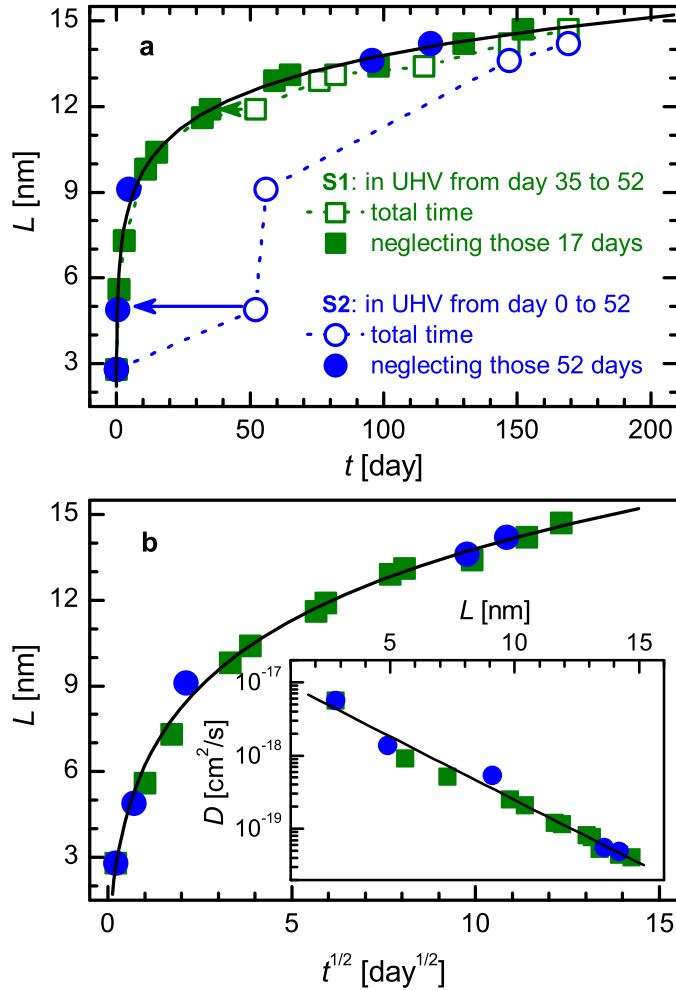
Figure 4.14: (a) Diffusion length (L) as a function of time for two samples (S1 and S2). L (in symbols) has been derived from the EDP. The total time (partly in atmospheric pressure and partly in UHV) as well as the time only in atmospheric pressure (neglecting the time that was inside UHV condition) were used for the plotting to get the clear idea that there is no change in L when the sample is in UHV and the clear evidence of atmospheric pressure induced atomic diffusion into solid. (b) Diffusion length as a function of square root of time (that it was in atmospheric pressure) to show the deviation from normal $t^{1/2}$ dependence (which should be a straight line). Inset: Diffusivity as a function of length. All solid lines represent analyzed curves considering the effective diffusivity, arising mainly due to atmospheric pressure and its exponential dependence on length.
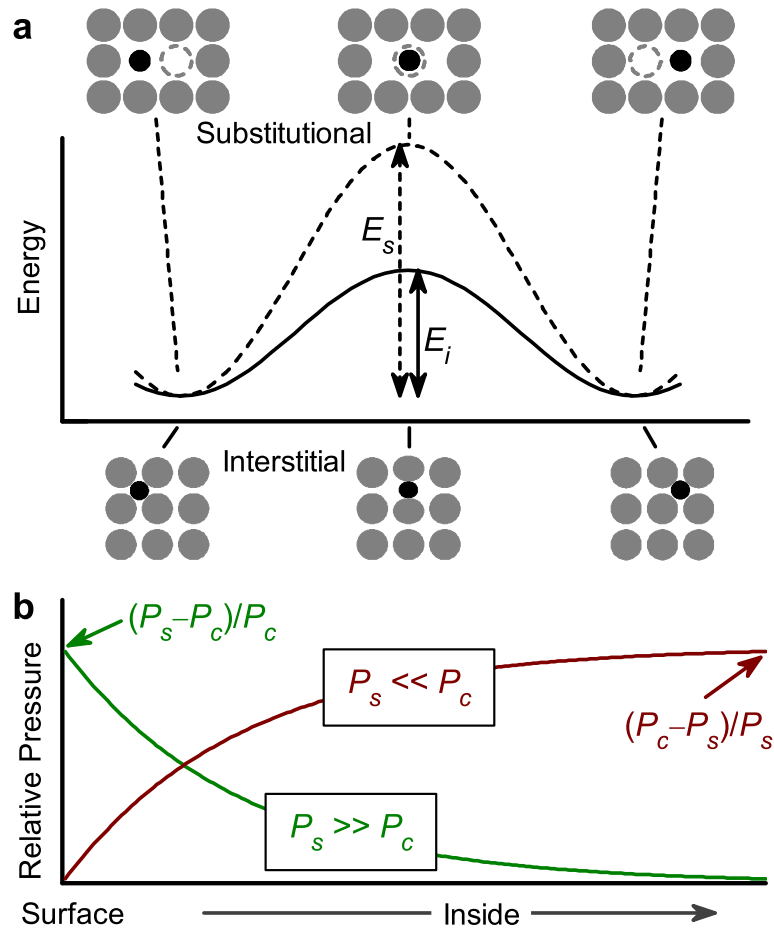
Figure 4.15: Schematic of diffusion and pressure gradient in solid crystal. (a) Two types of diffusion having different barrier energy. The activation energy required for the interstitial diffusion (E_i) is quite small compared to that for the substitutional diffusion (E_s). Still, the room-temperature (kT) is not sufficient to supply that small activation energy (E_i), while the atmospheric pressure, creating a pressure gradient, can supply that energy. (b) Relative pressure variation from surface to inside bulk for two extreme cases. Depending upon the value of the surface pressure (P_s) relative to the inherent-pressure (P_c), interdiffused nanolayer not only form but also moves inside (for $P_s \gg P_c$) or remains static (for $P_s \approx P_c$), or even diffuses outward (for $P_s \ll P_c$) with time.
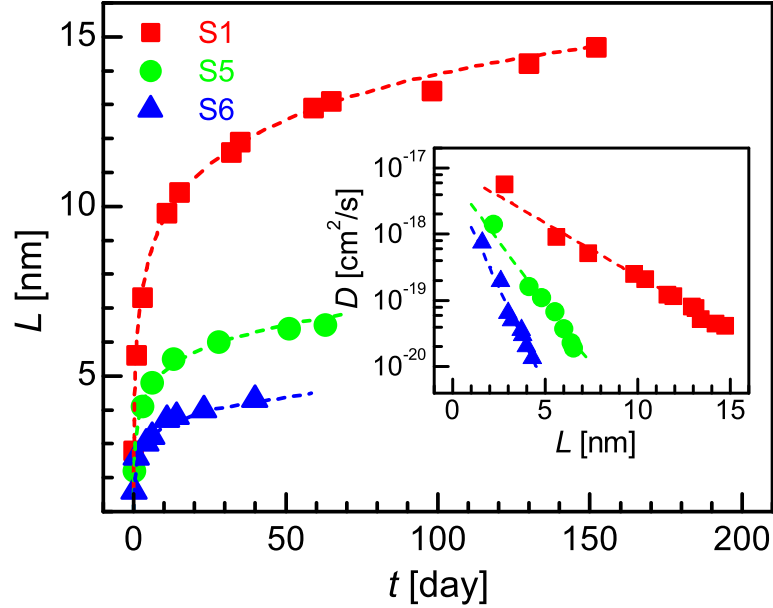
Figure 4.16: Time-evolution diffusion length and length dependent diffusivity (in the inset) for three samples (S1, S5 and S6) having different film thickness (d) and/or film coverage (C), such that $d_{S1} < d_{S5} < d_{S6}$ and/or $C_{S1} < C_{S5} < C_{S6}$. All dashed lines represent analyzed curves considering the effective diffusivity, where c_P and c_L are different for three samples. Preliminary analysis of the data clearly suggests that the value of c_P and c_L decreases as the thickness and/or the coverage of the film increases.

diffusion in such system, in particular and atomic diffusion in solid system [190], in general.

In silicon, gold atoms can either move around or displace silicon atoms (Fig. 4.15 (a)). First one is the interstitial diffusion, which requires relatively low activation energy (E_i), while later one is the substitutional diffusion, which requires relatively high activation energy (E_s). So, the question is that even we consider interstitial diffusion, does the room-temperature is sufficient to supply required activation energy ($E_a = E_i \approx 0.5$ eV)? If not, how does diffusion take place? In the following we will argue that this can be understood considering the strong role of atmospheric pressure in diffusion. The results suggest that when the system is in ambient condition,

the atmospheric pressure is helping to overcome the diffusion barrier [191], while when the system is in UHV condition no such driving force is there. The blocking of diffusion due to the growth of oxide layer comes into picture only when diffusion can take place. Also, this clearly indicates that the pressure inside a crystal (P_c), particularly in silicon is intermediate between atmospheric pressure to UHV. So in general, if we consider P_0 is the outside pressure that acts on the surface of the film and P_s ($= c_P P_0$) is the pressure that acts on the crystal surface, where c_P is a fraction that depends on the thickness and the effective density of the film, then $P_s - P_c$ is the effective pressure difference and $(P_s - P_c)/P_c$ is the normalized term that acts on the surface, which should decay gradually inside the crystal (for $P_s >> P_c$ in Fig. 4.15(b)). Considering exponential decay (along z-direction) with decay length λ_c, which can be considered as a characteristic length scale of that crystal structure, the effective diffusivity (D_{eff}) can be written as

$$D_{eff} = D(1 + \frac{P_s - P_c}{P_c} e^{-z/L_c}) \ , \tag{4.5}$$

where L_c ($= c_L \lambda_c$) is the effective decay length and c_L is a fraction that decides the initial freeness of the diffusing atoms [192]. $c_L \approx 1$ indicates $L_c \approx \lambda_c$, that means the diffusing atoms are almost free, while deviation from 1 indicates $L_c < \lambda_c$, that means the decay is fast and the diffusing atoms are not so free. The second term within the bracket in Eq. 4.5 arising entirely from the effect of pressure, in absence of which, the effective diffusivity becomes normal diffusivity. At room-temperature, the value of normal diffusivity is very small, so to observe appreciable diffusion, the second term must be very large compared to the first one. Considering effective diffusivity, the diffusion length can be expressed as

$$L = \sqrt{4D_{eff}t} \ . \tag{4.6}$$

Expression 4.6 is obtained from Fick's second law of diffusion, which can also be obtained from Einstein-Smoluchowski equation, considering Brownian motion as a fluctuation phenomenon [189]. The diffusivity and the diffusion length in Fig. 4.14 have been analyzed using Eqs. 4.5 and 4.6. The analyzed curves (solid lines in

Fig. 4.14) agree well with the experimental data. It is necessary to mention that for the present analysis, not all the parameters are independently very sensitive, as it mainly provides the value of L_c and combined value of $D \times (P_s - P_c)/P_c$, which are 2.5 nm and 1.3×10^{-17} cm^2/s, respectively. Also the analysis only suggests that $D \approx 10^{-21}$ cm^2/s, which implies $(P_s - P_c)/P_c \geq 10^4$ or $P_c \leq 10^{-4} \times c_P P_0$. In our present experiment, P_0 is the atmospheric pressure that acts on the gold surface. So the value of P_c is less by more than four orders of magnitude compared to the atmospheric pressure. This means, for the present system, we get definite value of L_c only, while for other parameter, like P_c, we get value within some range.

It is now imperative to discuss more about the two major parameters, namely P_c, the inherent-pressure inside a solid crystal structure and λ_c, the characteristic length scale. Although, the value of P_c for a particular crystalline material should be unique, the problem is to determine that value. It is very clear from Eqs. 4.5 and 4.6 that if we perform similar experiments for different value of P_0, which are lower than that of the atmospheric pressure, then the value of P_0 will come when there will be no diffusion or no change of diffusion length at all. From that value of P_0 there is a chance to predict the value of P_c more definitely. However, the problem may be that, no detectable or measurable diffusion is there for a range of outside pressure, then that will restrict the prediction of P_c beyond certain range. Nonetheless, in-situ experiments under precise pressure-controlled environments, after growing gold thin films on clean silicon surfaces, need to be carried out for getting best possible value. At the same time, estimation of P_c from theoretical point of view is required.

Unlike normal diffusion, which depends on concentration gradient and enhanced due to increase in temperature; the concept of P_c suggests that depending upon the relative pressure difference or the direction of pressure gradient (Fig. 4.15(b)), one can not only able to form the interdiffused nanolayer but also able to move that layer inside or keep that layer static, or even diffuse that layer outward with time. This observation is also completely new in comparison to the effect of pressure (mainly high pressure) on diffusion, which has been studied for quite long time [193–197]. The change in diffusion on those studies has been analyzed in terms of change in the

effective free volume in the crystal structure. That means, due to the application of the pressure, the crystal structure as a whole compressed or decompressed, and accordingly diffusion decreased or increased [193–197], which is not the case here. It is well known that the out diffusion of Si is enhanced in oxygen environment, which appear at the top of Au layer [92; 94]. This however can not explain the shock-wave-like diffusion behavior observed here. It is likely that due to the diffusion of Au into Si, some of the Si atoms are displaced outwards (compared to diffused layer) to release the extra stress. That displacement, if any, is enhanced not due to oxygen environment, rather due to pressure, which we have verified keeping samples in nitrogen environment of same pressure (where slightly more diffusion has been observed). It is necessary to mention that there are also other possible effects or mechanisms, namely, effect of Fermi-level, effect of concentration of interstitials and vacancies in surface region (e.g. due to native Si oxidation), influence of contamination with gas atoms and atomic collisions (energy transfer from gas atoms), etc. which can explain slight enhancement of atomic diffusion near Si surface [94; 198–200], but can not explain such pushing and stopping of the diffused layer inside Si. Coming to the parameter λ_c, it is clear from the analysis that we can only get the value of L_c and that $L_c \to \lambda_c$ when $c_L \to 1$. Although, it is difficult to know when c_L becomes 1, it is evident from the preliminary data (Fig. 4.16) that as the thickness and/or the coverage of the film decreases the value of c_L (also c_P) increases, i.e. the freeness of atoms increases, which is consistent with the earlier observation that the melting temperature of metal nanoparticles decreases [201]. Further experiments are require to understand the actual relationship of c_L and c_P with the thickness and/or the coverage of the film, which then can be utilized to estimate the value of λ_c.

4.4 Interdiffused layer: Direct evidences

It is known that, due to the loss of the phase information in the XRR data, the uniqueness of the derived EDP is always questionable. Verification of the right
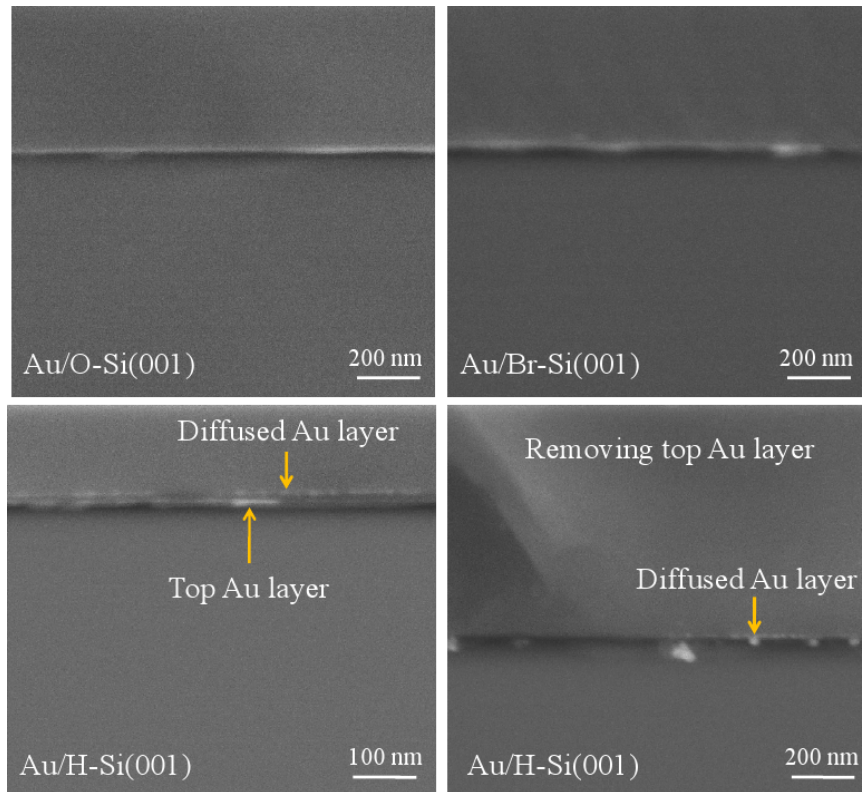
Figure 4.17: Cross-sectional SEM images of the three samples.

solution, through direct probe, remove that doubt and also provide additional confidence, which is helpful for data analysis. To verify the existence of the Gaussian-shape interdiffused nanolayer as predicted from XRR measurements, cross-sectional scanning electron microscopy and SIMS measurements have been performed after prolong interdiffusion.

4.4.1 Cross sectional SEM

Cross sectional SEM images of the three samples after prolonged interdiffusion are shown in Fig. 4.17. No distinct diffused Au nanolayer into Si is observed in Au/O-Si(001) and Au/Br-Si(001) samples though it is expected to observe in the later case as predicted by the EDP of Au/Br-Si(001) sample which is shown in Fig. 4.1. This

Figure 4.18: Cross-sectional SEM images of one of the diffusion samples, (a) with or (b) without top Au layer. Presence of diffused layer is clearly evident. (c) XRR data (symbols) and analyzed curves (solid lines) just after removing the top Au layer using aqua regia and also after removing the subsequent SiO_2/Si layer by HF etching of one of the diffused samples. Inset: Corresponding EDPs, which also confirm the presence of diffused layer.

Figure 4.19: SIMS line profiles of Au, Si and AuSi elements for the Au/H-Si(111) sample after prolonged diffusion. Positions of top Au layer and interdiffused Au-Si layer are indicated by arrows.

is due to the limitation of resolving power of SEM. It could not imaged the lower density region between top Au layer and diffused Au layer and consequently it shows a Au layer of higher thickness compared to of Au/O-Si(001) sample. But in case of Au/H-Si(001) sample a distinct well separated diffused Au layer has been observed. Only diffused Au layer, after removing the top Au layer, is shown in Fig. 4.17. For better observation a higher resolution image of this sample with or without top Au layer, are shown in Fig. 4.18(a) and (b). Also XRR measurements have been carried out, with similar samples having prolonged interdiffusion, just after removing the top Au layer by simple rubbing or by using aqua regia and also after removing the subsequent SiO_2/Si layer by HF etching. Typical XRR data along with the analyzed curves are shown in Fig. 4.18(c). It can be noted that SEM images and the EDP [shown in the inset of Fig. 4.18(c)] confirm the presence of diffused nanolayer.

4.4.2 SIMS

The Au/H-Si(111) sample after prolonged interdiffusion has been probed using SIMS, where strong and well separated interdiffused layer is expected. Figure 4.19 shows the SIMS line profiles of Au, Si and AuSi elements for that sample. The Si signal starts from certain point, indicative of substrate position and becomes constant as expected. Strong Au signal in the initial part is due to the top Au layer, which decays to zero inside the substrate. However, small-hump in the Au signal, indicated by arrow, seems to be there, which is well evident from the AuSi signal. This is the interdiffused layer, which is inside the substrate and well separated from the interface as expected from the XRR analysis.

4.5 Conclusions

The diffusion of Au into Si substrate has been studied at room temperature by changing the passivating elements like O, H, Br and also by changing the crystalline orientation of the Si substrate like Si(001), Si(111). Time-evolution x-ray reflectivity

measurements suggest strong diffusion of Au into Si(001) substrate when surface is pretreated with HF and, subsequently, large variation in the topography. While Au deposited on Si(001) surface further pretreated with Br shows small diffusion, that on untreated Si surface shows negligible diffusion with relatively smooth topography. The evolution of the Au/Si(001) interdiffused layer with time has been attributed to the diffusion of Au through unblocked Si surface. The unblocked area through which diffusion takes place decreases exponentially with time. The growth of the blocking layer is related to the surface stability due to surface passivation. The nature of the diffusion in Au/Si(111) system is similar to that of the Au/Si(001) system. Though they are qualitatively similar but there is large quantitative differences. The diffused amount of Au into Si is greater in each passivation for Si(001) surface compared to Si(111) surface and the growth-time of oxide i.e. (τ) value is one order greater in case of Br-passivated Si(111) surface compared to Si(001) which indicates Br-passivated Si(111) is more stable compared to Br-passivated Si(001). The size, electronegativity, bond-energy etc. of the passivating materials and the number of dangling bonds on the Si surface determined the stability or instability of the Si surface. This instability, parameterized by growth-time (τ) alone, can control the amount of diffusion, apart from the openness of the Si surface structure. However, distribution of τ, as observed from stretched exponent ($\beta < 1$), fractional passivated area and large in-plane correlation length ($\xi' > R_D > \xi$) in the topography are against such control.

This work shows clear signature of atmospheric pressure induced atomic diffusion into solid crystal and provides unique concept of inherent-pressure inside a crystal structure. It also provides a characteristic length scale, which is a measure of quantitative extent of pressure gradient, from the surface to the bulk of that solid crystal. The atomic diffusion observed here is more like a fluid flow, where relative pressure acts as a regulating valve, which not only controls the speed but also controls the direction of the flow. Apart from the pressure-gradient, such diffusion depends on the crystal structure and freeness of the diffusing atoms. The analysis suggests that

the freeness of the diffusing atoms increases with decreasing thickness and/or coverage of gold layer. We claim that by changing the surface passivation, stability of the surface can be changed, which then can be used to control the layer of interdiffusion in nanometer length scale. Moreover the position of the diffused Au layer into Si can be tuned by varying the pressure acting on the Au film.

Chapter 5

Ag on passivated Si surface: Observation of dewetting

5.1 Introduction

Ag (compared to Al) has been recognized as a potential interconnection material for ultralarge-scale integration (ULSI) technology because of its high electrical conductivity and high electromigration resistance. As the dimensions of electronic devices decrease with increasing packing density, the thickness of metal layers decreases continuously. Accordingly, understanding of growth of metal thin film on a semiconductor become important both from fundamental and practical point of view [202]. In general, there are three known thin film growth modes: layer-by-layer [Frank-van der Merwe (FM)], island [Volmer-Weber (VW)] and layer-plus-island [Stranski-Krastanov (SK)] growth modes [103; 104]. Which growth mode will be adopted in a given system will depends upon the surface free-energy terms and on the lattice mismatch. A great deal of effort has been devoted in controlling and/or altering the film growth using foreign species or 'surfactants' [6]. Introduction of a foreign atomic

---

layer (of hydrogen, bromine, etc.) in place of clean or oxide layer, on substrate surface [7; 95; 105–111] can change its surface energy and/or roughness, which can alter the growth mode and morphology of a overlayer. The morphology and structure of that thin overlayer, plays significant role in its electrical [203] and other physical properties.

The effects of deposition conditions on the morphology of thin Ag films on Si have been investigated extensively in recent decades. Ag is found to grow epitaxially on both Si(001) and Si(111) through coincident site lattice matching, though there is a large (25%) lattice mismatch [112–116]. Epitaxial Ag films have been obtained mostly by molecular beam epitaxy (MBE) process, where the energy of depositing particles is relatively low. While, using magnetron sputtering process, Ag films usually obtained are non-epitaxial, although having <111> as preferred growth orientation [117; 118]. However, in few works, epitaxial growth of Ag on native oxide covered Si(100) has been observed by magnetron sputtering process at higher temperatures [119; 120]. Epitaxial growth of Ag on H-passivated and Br-passivated Si(111) substrates has been observed above room temperature (RT) [36; 121–126]. But there is no such report on epitaxial growth of Ag on H-Si(001) at RT.

It is clear from the large number of studies of Ag film on Si that Ag dewets the native oxide covered Si (O-Si) surface [169; 204] and wets the clean Si surface [7]. If γ_m and γ_s are the surface free energies of metal and substrate, respectively and γ_{in} is the metal-substrate interface free energy then to satisfy dewetting condition for Ag on O-Si is $\gamma_m + \gamma_{in} > \gamma_s$ and to satisfy wetting condition for Ag on clean Si is $\gamma_m + \gamma_{in} < \gamma_s$ [104]. These can be well understood considering the surface energies ($\gamma_m \sim$ 1.1-1.2 J/m^2 for Ag, $\gamma_s \sim$ 1.2 J/m^2 for clean Si and $\gamma_s \sim$ 0.3-0.6 J/m^2 for O-Si) [160; 205; 206] and simply neglecting the interfacial energies. Although, Ag on clean Si satisfies wetting condition, it is not necessary that it always form epitaxial film. Studies suggest that epitaxy can be achieved either by slow deposition (like MBE) or by enhanced surface migration. Enhanced surface migration or in-plane diffusion can be achieved by raising the growth temperature [119; 120] or by introducing foreign atoms [7; 106]. Better epitaxial film has been obtained on H-passivated Si surface,

which has been attributed to enhanced surface migration and increased nucleation site density. In general, it is accepted that by passivating the surface differently, one can grow thin films of different morphology and epitaxy. It is also known that this passivation is not stable for longer time in open air, even in presence of overlayer such as Au, which is presented in the chapter 4. With time, passivated layer desorbs [105] and native oxide layer grows at the metal-semiconductor interface [43], which can change the surface and interface energies leading to a modification in the film growth. No study have been made so far, to monitor such later stages of growth of Ag on Si, which is very important from the stability point of view and give rise the possibility to study interesting growth transition. Understanding of associated physical phenomena will help to control the growth.

In this study, using complementary techniques, we have monitored both in-plane and out-of-plane evolution of Ag nanolayers deposited on differently passivated Si(001) substrates. It has been observed that the interfacial instability *at ambient conditions* induces the wetting to dewetting transition in the Ag nanolayers, which then provides interesting nanostructures having different size, number density and even crystallinity and/or epitaxy, depending upon initial Si(001) surface passivation conditions. An attempt has been made to understand such transition considering change in interfacial energies.

To see the evolution of EDP, XRR data for one set of samples were collected as a function of time after keeping that set *at ambient conditions*, while for other set of samples, XRR data have been collected just before and after the samples were in UHV conditions. XRD data around Ag(111) and Ag(200) peaks were collected as a function of time for the same set of samples that kept *at ambient conditions* for monitoring the evolution of crystallinity and/or epitaxy. Prior to XRD measurements, x-ray beam was aligned parallel to the Si(004) plane. Also to find out the major crystalline directions of Ag(111) and Ag(200) planes, rocking scans across those peaks were performed.

The topography of the Ag nanolayers on differently passivated Si(001) substrates in small scales but in great details were mapped through AFM technique
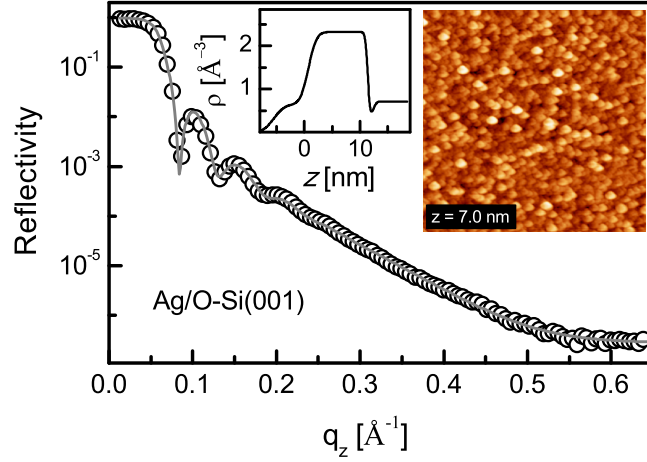
Figure 5.1: XRR data (symbol) and analyzed curve (solid line) of Ag nanolayers on oxide covered Si(001) substrate. Inset: corresponding analyzed EDP and AFM image (of scan size 2000×2000 nm^2). z indicates the maximum height-variation (in nm).

at ambient conditions and also mapped through STM technique at UHV condition ($\sim 10^{-10}$ mbar) to separate out the effect of ambient conditions on the evolution of sample topography. The evolution of topography in large area and in greater statistics of the Ag nanolayers on differently passivated Si(001) substrates *at ambient conditions* were mapped through SEM technique.

5.2 Results and discussion

5.2.1 Growth and evolution at ambient condition

5.2.1.1 Electron density profile and its evolution

Time-evolution XRR data of Ag nanolayers on differently passivated Si(001) substrates at ambient conditions are shown in Fig. 5.1 and Fig. 5.2. Oscillations are evident in all the curves. The shift of these oscillations towards lower q_z value with time however, depends strongly on the initial passivation conditions. Very rapid
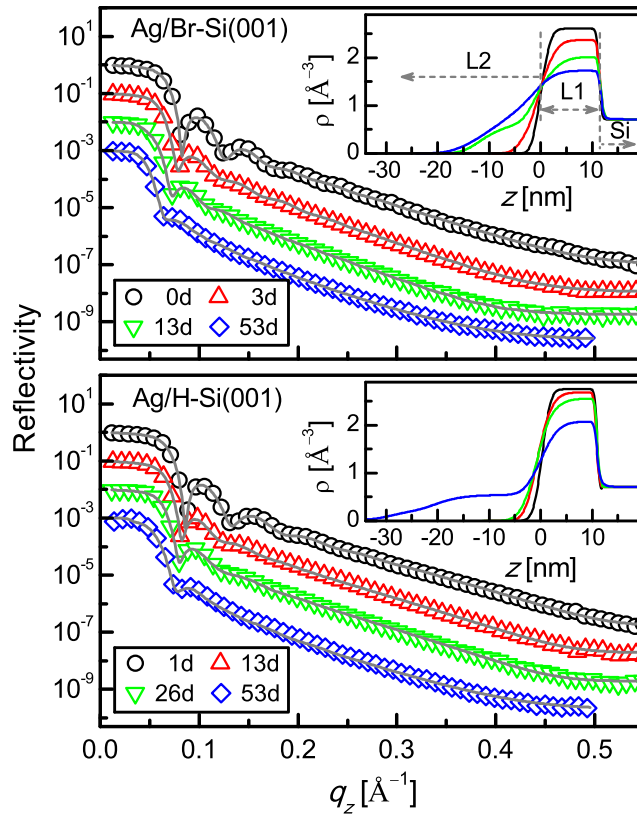
Figure 5.2: Time-evolution XRR data (different symbols) and analyzed curves (solid line) of Ag nanolayers on two differently pretreated Si(001) substrates *at ambient conditions* in two panels. In each panel, data and curves are shifted vertically for clarity. In legends, 'd' indicates the time in day. Inset: corresponding analyzed EDPs, which consist of two layers (L1 and L2) above Si substrate as indicated.

shift is observed in the XRR profile of Ag/Br-Si(001) sample compared to Ag/H-Si(001) sample. No significant change in the XRR profiles (shown in Fig. 5.1) for the Ag/O-Si(001) sample has been detected and excluded from further discussion. The corresponding EDPs are shown in the inset of Fig. 5.2. It can be noted that all EDPs can be divided into three parts: first part is the Si substrate of constant electron density; second part is L1, the original deposited Ag layer (of fixed thickness about 11 nm) at the bottom, electron density of which decreases with time and third part is L2, the top Ag layer that forms due to migration of Ag from original layer, both thickness and electron density of which increase with time. However, the initial values of different parameters and their variation with time are different for different samples. The peak value of ρ of the L1 layer for the Ag/Br-Si(001) sample changes from 2.6 to 1.8 $e/\text{Å}^3$, whereas that for the Ag/H-Si(001) sample changes from 2.75 to 2 $e/\text{Å}^3$.

5.2.1.2 Topography and its evolution

Typical AFM images of Ag nanolayers, taken just after deposition on different passivated Si(001) substrates, are shown in Fig. 5.3. Initial topography, obtained from the AFM images, suggests that all films are composed of islands. However, the height-variation of the Ag/Br-Si(001) sample is large compared to that of the Ag/H-Si(001) sample. Correspondingly, compactness of the latter nanolayer is more, which is also consistent with the EDP. This indicates that the wetting of Ag nanolayer on the H-Si(001) substrate is comparatively better, while dewetting of Ag nanolayer on the Br-Si(001) substrate starts even in the initial stage. It is necessary to mention that the formation of nearly dewetted structure of Ag nanolayer on the O-Si(001) substrate (shown in the inset of Fig. 5.1) is observed. The evolution of topography, monitored using SEM images, are shown in same Fig. 5.3. Growth of large size islands with time are clearly evident. The large size islands that grow in the Ag/Br-Si(001) sample has large number-density and size distribution having size less than 1 μm. On the other hand, for the Ag/H-Si(001) sample, number-density and size
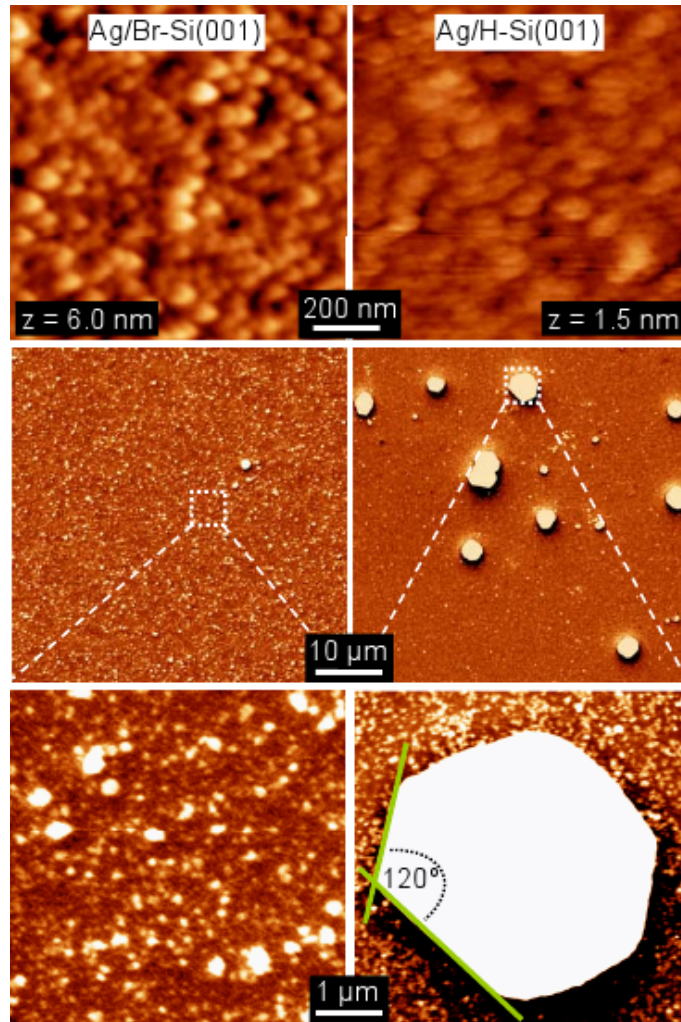
Figure 5.3: Topography of Ag nanolayers on two differently pretreated Si(001) substrates in two columns. Top panel: AFM images showing initial topography. z indicates maximum height variation. Middle and bottom panels: SEM images in two length scales showing time-evolution topography *at ambient conditions*. Well faceted planes and angle between them are indicated for the dewetted Ag island on the H-passivated Si(001) surface.
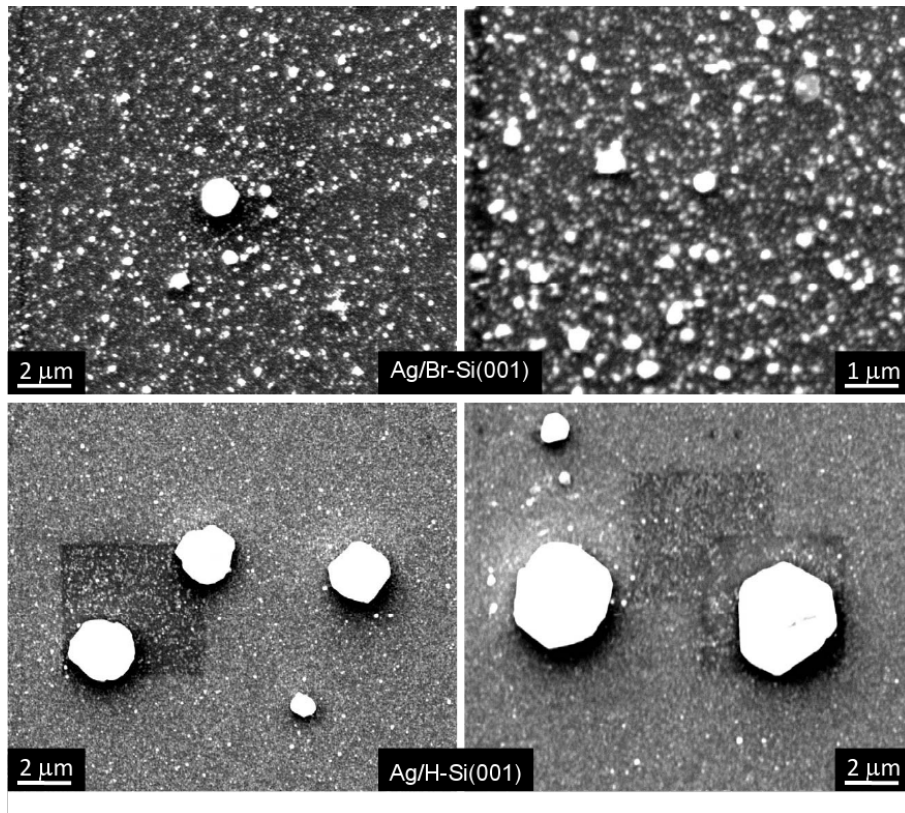
Figure 5.4: SEM images showing morphology after prolonged dewetting of Ag nanolayers on two differently pretreated Si(001) substrates in two panels. Top panel: Ag nanolayers on Br-passivated Si(001). Lower panel: Ag nanolayers on H-passivated Si(001).

distribution of large size islands are found to be small having size in the range 1-8 μm. The shape of the islands on the latter sample show faceting nature similar to that observed for directed crystalline or epitaxial growth. More images of these samples are shown in Fig. 5.4 where such 3D crystalline islands are well evident in Ag/H-Si(001) sample. We made an attempt to do AFM measurement (It is very difficult to obtain a stable image) which is shown in Fig. 5.5 to get an idea about the height of such big 3D island. The height of one such 3D island is about 850 nm.
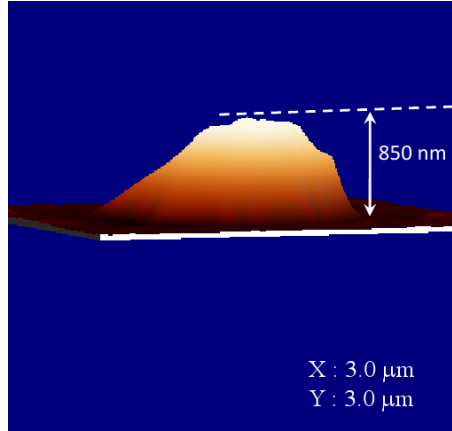
Figure 5.5: AFM image (3D view) of a 3D big Ag island on H-passivated Si(001).

5.2.1.3   Dewetting: Time dependence

In order to understand the evolution of Ag nanolayer at ambient conditions, the variation of its coverage on different passivated surfaces are plotted as a function of time in Fig. 5.6. The coverage (C in fraction) of the nanolayer is calculated from the EDP by considering the peak value of ρ at L1 layer in a particular time, normalized with the corresponding bulk value ($2.77\ e/\text{Å}^3$). It is evident from Fig. 5.6 that the nature variation of C for two samples are very much different. For the Ag/Br-Si(001) sample, coverage decays very rapidly from the beginning in exponential nature, while for the Ag/H-Si(001) sample, two different types of decay (classified in two regions) have been observed. In region-I, i.e upto about 32 days, the decay of coverage is very slow and linear in fashion, while in region-II, i.e beyond 32 days, the decay of coverage is similar in nature to that of Ag/Br-Si(001) sample. The variation of coverage can be quantitatively analyzed using following general relations

$$C(t) = \begin{cases} 1 - \frac{1-C_c}{t_c}t & \text{for } t \leq t_c \\ (C_c - C_\infty)e^{-(t-t_c)/\tau} + C_\infty & \text{for } t \geq t_c \end{cases}, \tag{5.1}$$

where t_c is the critical time (for transition from linear to exponential nature) and C_c is the corresponding value of the coverage, C_∞ is the final coverage and τ is the decay time. Analysis of the time-evolution coverage data using Eq. 5.1 are shown
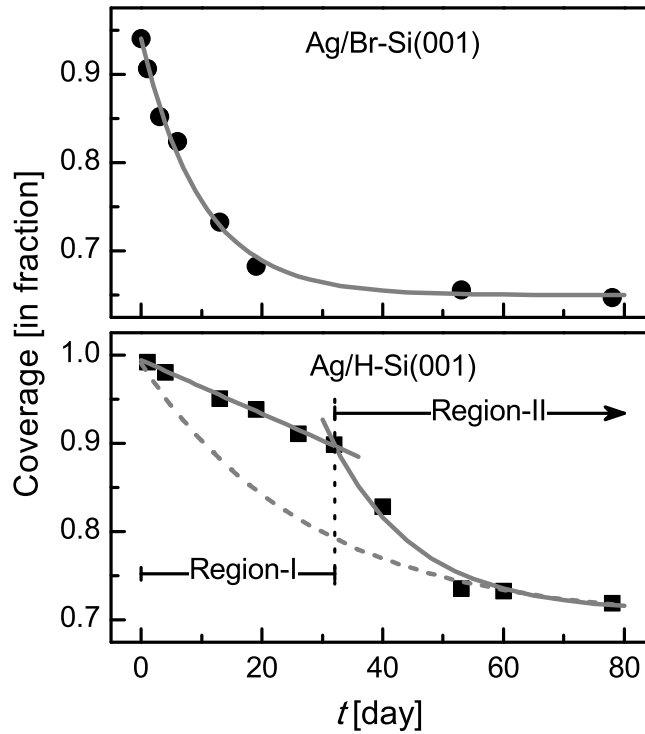
Figure 5.6: Variation in coverage of Ag (from original L1 layer) with time on two differently pretreated Si(001) substrates *at ambient conditions* in two panels. In top panel, solid line represents simple exponential decay. In bottom panel, two regions exist (separated by dotted line). Solid line in region-I corresponds to linear decay, while solid line in region-II corresponds to exponential decay. Dashed line indicates possible exponential decay considering whole range.

in Fig. 5.6. Parameters obtained from the analysis are $t_c \approx 0$ day, $C_c \approx 0.94$, $C_\infty \approx 0.65$ and $\tau \approx 10$ days for the Ag/Br-Si(001) sample; while $t_c \approx 32$ days, $C_c \approx 0.9$, $C_\infty \approx 0.7$ and $\tau \approx 14$ days for the Ag/H-Si(001) sample. Considering slow linear decays in region-I, the value of τ for the latter sample is quite large. This can also be realized (from $\tau \approx 28$ days) if we analyze the whole range of data with exponential function (dashed curve in Fig. 5.6) for comparison. The decay of Ag coverage can be related to the growth of oxide layer on the passivated Si(001) surface, which takes place even in presence of metal layer [43]. However, the oxide growth in the Ag/Si(001) system is very slow compared to that in the Au/Si(001) system [43] and covers only about 30% of the surface area. It is known that Ag/Si interface is less reactive compared to Au/Si interface [94]. which makes the former interface abrupt and slow down the diffusion of oxygen at the interface through Ag layer.

5.2.1.4 Towards crystallinity and/or epitaxy

Crystalline or epitaxial nature of the samples at ambient conditions have been verified monitoring time-evolution XRD data, mainly Ag(111) and Ag(002) Bragg peaks, as shown in Fig. 5.7. For the Ag/Br-Si(001) sample, the intensity of Ag(002) peak is almost negligible, while the intensity of Ag(111) peak increases slightly with time. On the other hand, for the Ag/H-Si(001) sample, the intensity of Ag(002) peak increases appreciably with time, while the intensity of Ag(111) peak remains almost negligible. It can be noted that Ag(111) peak is the 100% peak of the bulk crystal structure and expected to observe [117; 118] even if films are composed of randomly oriented Ag nanocrystals. The fact that, no Ag(111) peak has been observed in the initial stage may be related to the low thickness (about 11 nm) of the film. The intensity of different peaks become observable with time as 3D-islands grow from more thin 2D structures (as evident from EDP and topography). The slight increase of the Ag(111) peak intensity having no preferred direction (as confirmed from rocking curve) for the Ag/Br-Si(001) sample is a clear signature of non-textured
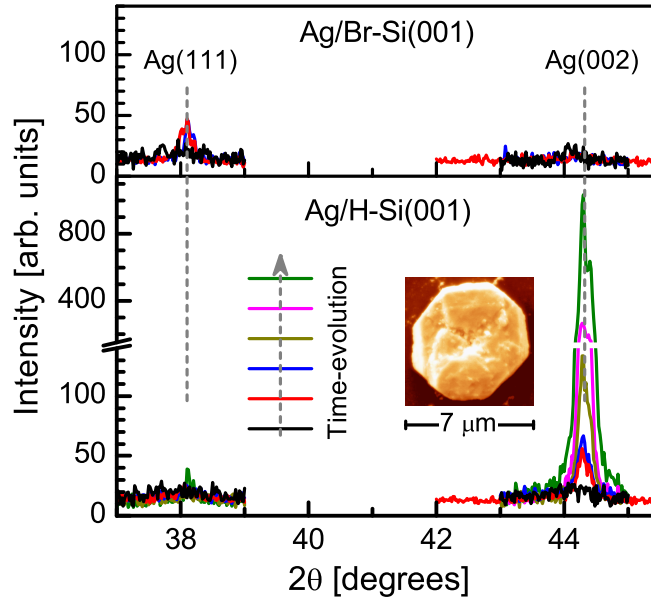
Figure 5.7: Time-evolution XRD data (around two Bragg peaks as indicated) of Ag nanolayers on two differently pretreated Si(001) substrates *at ambient conditions* in two panels. Inset: SEM image showing typical island structure of Ag that evolved with time on H-passivated Si(001) surface.

growth of 3D-islands of Ag on Br-Si(001) surface. On the other hand, appreciable increase of the Ag(002) peak intensity having preferred direction (<001> direction of Si substrate as obtained from rocking curve) for the Ag/H-Si(001) sample suggests epitaxial [Ag(001)/Si(001)] growth of 3D islands of Ag on H-Si(001) surface with time.

5.2.2 Growth and evolution at UHV condition

Time-evolution XRR data of Ag thin films on differently passivated Si(001) substrates at UHV conditions are shown in Fig. 5.8. EDPs obtained from the analysis of XRR data are shown in the inset of same Fig. 5.8. It can be noted from the XRR profiles that there is almost no changes in the samples with time as long as
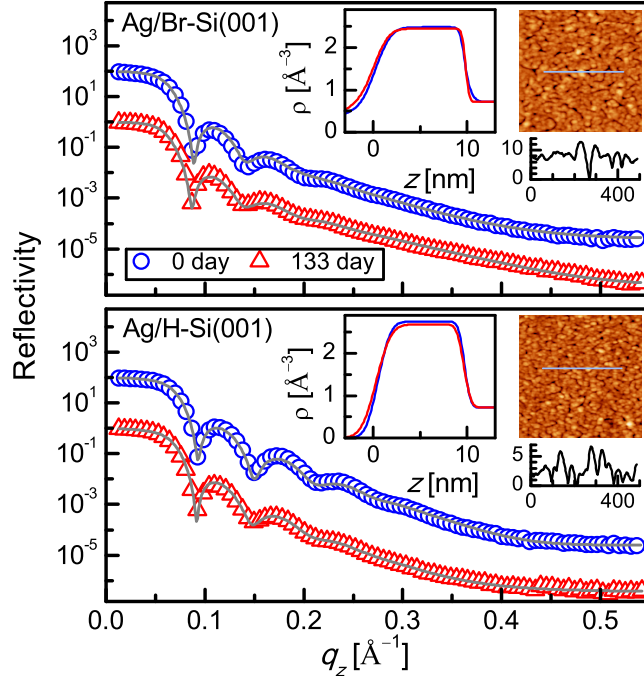
Figure 5.8: Time-evolution XRR data (different symbols) and analyzed curves (solid line) of Ag nanolayers on two differently pretreated Si(001) substrates *at UHV conditions* in two panels. In each panel, data and curves are shifted vertically for clarity. Inset: corresponding analyzed EDPs and STM image (of scan size 750×750 nm^2) along with line profile showing height-variation (in nm).

those are at UHV conditions, which is also evident from the corresponding EDPs. STM images of the same samples (when at UHV conditions) collected at different time suggest that there is no appreciable change in the topography of the samples with time. Typical topography of each samples along with a line profile are shown in the inset of Fig. 5.8. Height-variation of the Ag/Br-Si(001) sample is found to be more compared to that of the Ag/H-Si(001) sample, consistent with the EDPs, suggesting initial small dewetting nature of the Ag/Br-Si(001) sample and better wetting nature of the Ag/H-Si(001) sample, which however, remain unchanged with time in UHV conditions.

5.2.3   Role of passivation in wetting and dewetting

It is known that the surface and interface free energies govern the growth mode of metal thin film on semiconductor surface [104], and any change in these energies (namely γ_s and γ_{in} due to the oxide growth) with time can strongly alter the growth mode of the film (from wetted to dewetted nature) on the substrates. The surface energy of H-passivated Si(001) surface ($\gamma_{\text{H-Si}}$) is known [206], which is less than that of the clean Si(001) surface (γ_{Si}), but comparable to that of the oxide covered Si(001) surface ($\gamma_{\text{O-Si}}$). On the other hand, the surface energy of Br-passivated Si(001) surface ($\gamma_{\text{Br-Si}}$) is not known. If we consider it to be comparable to that of the H-passivated Si(001) surface, then evolution of dewetted structures is mainly related to the interfacial free energy (which includes adhesion, in-plane diffusion, etc.) and its change with time. The values of of free energy and its change due to instability, which we are concerned about, are the average value. The passivated surface is not homogeneous in terms of passivation. Due to inhomogeneity some areas (can be referred to as the strongly passivated area) of the surface remain passivated for longer time compared to others (can be referred to as weakly passivated area) when exposed to open air, even in the presence of overlayer (Ag, Au). For the weakly passivated areas, fast desorption of H or Br atoms followed by the growth of oxide layer takes place, while for the strongly passivated areas, oxide layer rarely grows as the desorption is slow or almost negligible. The number-density and size of dewetted structures, which we observed here, are related to this inhomogeneous nature of the passivated surface, while the value of τ is related to the average instability of the passivated surface, which is different for different surface passivation.

The variation in initial growth or wettability of Ag nanolayer on different passivated surface, which is mainly related to the initial interfacial free energy, suggests that $\gamma_{\text{Au/H-Si}} \ll \gamma_{\text{Au/Br-Si}} < \gamma_{\text{Au/O-Si}}$. The value of $\gamma_{\text{Au/H-Si}}$ or $\gamma_{\text{Au/Br-Si}}$, however, changes with time and tries to be the value of $\gamma_{\text{Au/O-Si}}$. Within the surface, dewetting (after deposition) starts from the weakly passivated areas, where the fast growth of the native oxide layer quickly changes the interfacial free energies. Accordingly, Ag

atoms on weakly passivated areas leave 2D layer (L1) and go on top of the remaining L1 layer. It can be noted that the origin of the observed dewetting on passivated surface with time at ambient condition here is quite different from the surface unwetting during growth on clean surface at UHV condition found earlier [207]. The number density and size of the dewetted structures evolved in the Ag/Br-Si(001) sample indicate that the Br-Si(001) surface has large number of strongly Br-passivated area, which are very small in size. Growth of 3D structures having no preferred crystallographic direction take place around those strongly passivated points, by dewetting from weakly passivated area. However, dewetted Ag atoms cannot diffuse easily over relatively rough L1 layer, which restrict the size of 3D islands. It is know that large mobility of Ag on H-passivated Si(001) surface can helps to form better wetted as well as epitaxial layer, which is evident in the Ag/H-Si(001) sample. The high compactness and epitaxial nature of the Ag film, probably control the initial slow linear growth of dewetted structures at ambient conditions, while the high exponential growth time of dewetted Ag structures is related to the high stability of the H-Si(001) surface compared to that of the Br-Si(001) surface [43]. The growth of small number-density and relatively large size of Ag structure with time indicate that the H-Si(001) surface have small number of strongly H-passivated area, which are relatively large in size. Growth of large 3D epitaxial structures take place around those strongly passivated area, by similar dewetting from weakly passivated area and also through large mobility or in-plane diffusion over H-passivated area. Well faceted layered structures of large 3D-islands are evident form the SEM image (shown in the inset of Fig. 5.7), which seems to form due to migration and coalesce of small islands [208; 209].

5.3 Conclusions

The growth process of Ag nanolayers on differently passivated Si(001) substrates and its time evolution at ambient conditions have been investigated using complementary techniques like XRR, XRD, AFM and SEM. SK (layer-plus-island)-like growth mode

of Ag nanolayers have been observed initially, which is more towards FM (layer-by-layer)-like growth mode on H-passivated Si(001) surface, while that on Br-passivated Si(001) surface is more towards VW (island)-like growth mode as observed on native oxide covered Si(001) surface. Such initial growth modes remain almost unchanged in UHV conditions, while at ambient conditions strong evolution of growth has been observed. Dewetted 3D-island-like structures evolved due to the oxide growth at the interface. On the Br-passivated Si(001) surface, fast growth of large number of small size 3D structures having no preferential crystallographic direction have been observed, while on the H-passivated Si(001) surface, slow growth of small number of large size well faceted 3D epitaxial [Ag(001)/Si(001)] structures have been observed. Such transition from relatively wetted to dewetted structures of Ag nanolayer having epitaxy or not, along with initial growth can be understood considering interfacial energies as $\gamma_{Ag/H\text{-}Si} \ll \gamma_{Ag/Br\text{-}Si} < \gamma_{Ag/O\text{-}Si}$. Surface free energy, surface mobility and surface instability of the passivated surfaces govern and control the growth and evolution of such interesting structures of silver on silicon.

Chapter 6

Cu on passivated Si surface: Coexistance of interdiffusion and dewetting

6.1 Introduction

Now a days, Cu interconnect technology has replaced aluminium technology in high performance Si microelectronic devices [210–212]. As there is definite gain upon moving from Al ($\rho \sim 2.7$ $\mu\Omega$-cm) to Cu ($\rho \sim 1.7$ $\mu\Omega$-cm), it is likely that Cu will be dominant interconnect technology for Si integrated circuits until some new paradigm is developed [213]. Also, as the metal pitch decreases and the number of metal layers increases, it becomes increasingly important to control the chemical physics and reliability of interconnect structures. A particular concern with Cu technology is that Cu may interact with dielectric insulator materials to degrade the interface and lead to a loss of adhesion, or Cu diffusion into the dielectric materials [214]. Although Cu is a key component of such interconnects, interdiffusion of Cu from the surface into the bulk of the silicon chip can adversely affect device performance [130]. In reality, the physics of Cu in Si is more complicated than indicated above, and is an active area of research [130]. Therefore, a further understanding of the Cu/Si interface, Cu contamination in Si, and the potential effects of hydrogen-ubiquitous in processing-could be significant in combating surface-to-bulk diffusion of Cu on Si
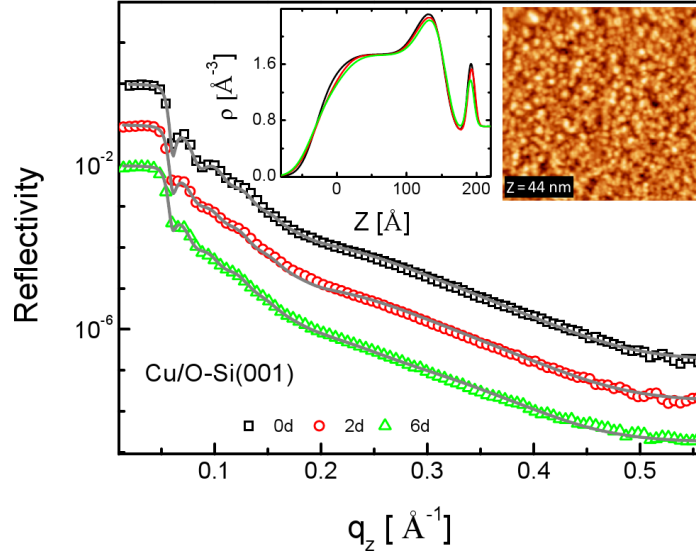
Figure 6.1: Time-evolution XRR data (different symbols) and analyzed curves (solid line) of Cu nanolayers on native oxide covered Si(001) substrate. Data and curves are shifted vertically for clarity. Inset: corresponding analyzed EDPs and AFM image (of scan size 2000×2000 nm^2) after prolonged dewetting and interdiffusion. z indicates the maximum height-variation. In legends, 'd' indicates the time in day.

and in improving the processing of valuable Cu-based interconnects.

Native oxide layer acts as a diffusion barrier at the metal-semiconductor interface. Such oxide layer can be removed by passivation methods. Among these H-passivation is more suitable compared to Br-passivation in order to get larger diffusion of Au into Si substrate. Whereas Ag does not diffuse into Si, it makes abrupt interface with the substrate. It has been shown that Ag film is more compact or wetted on the H-passivated Si surface in comparison with Br-passivated one. In case of Cu, it has intermediate tendency to interact with Si substrate. However, to our knowledge one or two study have been made so far where they have investigated the role of native oxide in interdiffusion of Cu into Si substrate at elevated temperature [31; 135; 215]. No such study have been made so far at room temperature (RT) by changing different passivating elements like H, Br etc. at the interface in order to control the growth of Cu nanolayer at the time of deposition and beyond that.

The purpose of this investigation is to study the initial growth behavior of Cu nanolayer on Si substrate by varying different passivating elements like H, Br at the interface at RT and also to explore how it evolves with time after deposition. For that XRR measurements of Cu/Si(001) samples were carried out using a VXRD setup as a function of time. The topography of the Cu nanolayers on differently passivated Si(001) substrates in small scales but in great details were mapped through AFM technique at ambient conditions. The evolution of topography in large area and in greater statistics of the Cu nanolayers on differently passivated Si(001) substrates were mapped through SEM technique.

6.2 Results and discussion

6.2.1 Electron density profile and its evolution

Time-evolution XRR data of Cu nanolayers on differently passivated Si(001) substrates at ambient conditions are shown in Fig. 6.1 and 6.2. Oscillations are evident in all curves. The shift towards lower q_z value with time, which is a indicative of some increment in thickness, depends on initial passivation conditions. Rapid shift is observed in both H-passivated and Br-passivated Si surfaces, while very slight change in the XRR profile and EDP (shown in the inset of Fig. 6.1) is detected. For this reason Cu/O-Si(001) sample is excluded for further discussions. The corresponding EDPs of other two samples are shown in the Fig. 6.3. It can be noted that all EDPs can be divided mainly into four parts: first part is the diffused Cu layer L_d into Si substrate whose thickness rapidly increases with time; second part is L1, one part of the original deposited Cu layer (of fixed thickness about 4 nm) at the bottom, it is very compact and takes nearly the bulk Cu density [$2.27e/\text{Å}^3$], electron density of which decreases with time and third part is L2, rest part of originally deposited layer which is not much compact compared to the lower one [i.e. L1 layer], whose density also decreases but thickness remains nearly same, and the last layer i.e. L3 which is the top Cu layer that forms due to migration of Cu from original layers L1

135
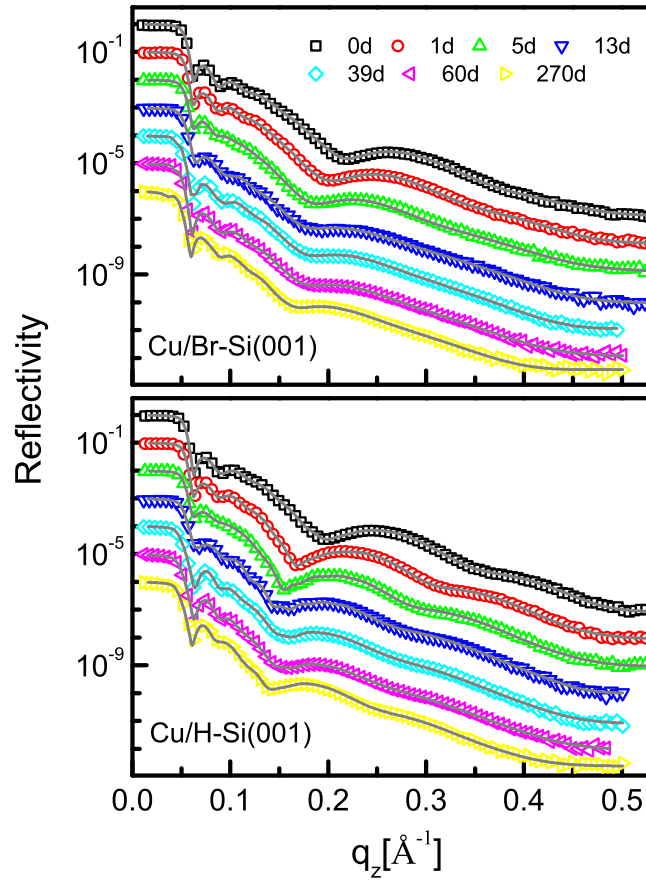
Figure 6.2: Time-evolution XRR data (different symbols) and analyzed curves (solid line) of Cu nanolayers on two differently pretreated Si(001) substrates in two panels. In each panel, data and curves are shifted vertically for clarity. In legends, 'd' indicates the time in day.
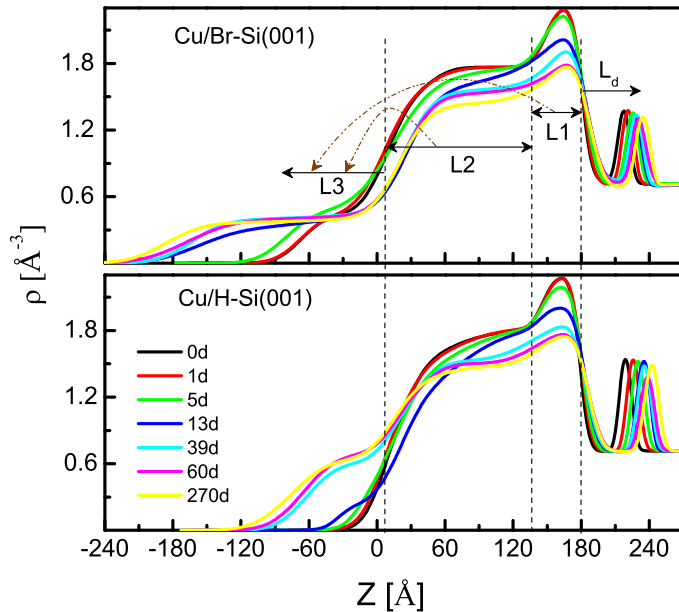
Figure 6.3: Analyzed EDPs, which consist of three layers (L1, L2 and L3) above Si substrate and one layer (L_d) into Si substrate as indicated for two samples in two panels. In legends, 'd' indicates the time in day.

and L2, both thickness and electron density of which increases with time. However, the initial values of different parameters and their variation with time are different for different samples.

6.2.2 Topography and its evolution

6.2.2.1 Atomic force microscopy

Typical AFM images of Cu nanolayers, taken in contact mode after prolonged dewetting and interdiffusion in different passivated Si(001) substrates, are shown in Fig. 6.4. The topography, obtained from the AFM images, suggests that all films are composed of islands. Apart from this few scattered big 3D-islands has been observed in both the samples. In the Cu/Br-Si(001) sample the size of these 3D-islands varies from 180-250 nm whereas in Cu/H-Si(001) sample it varies from 120-150 nm which is smaller relative to the former sample. The shape of the islands in both the
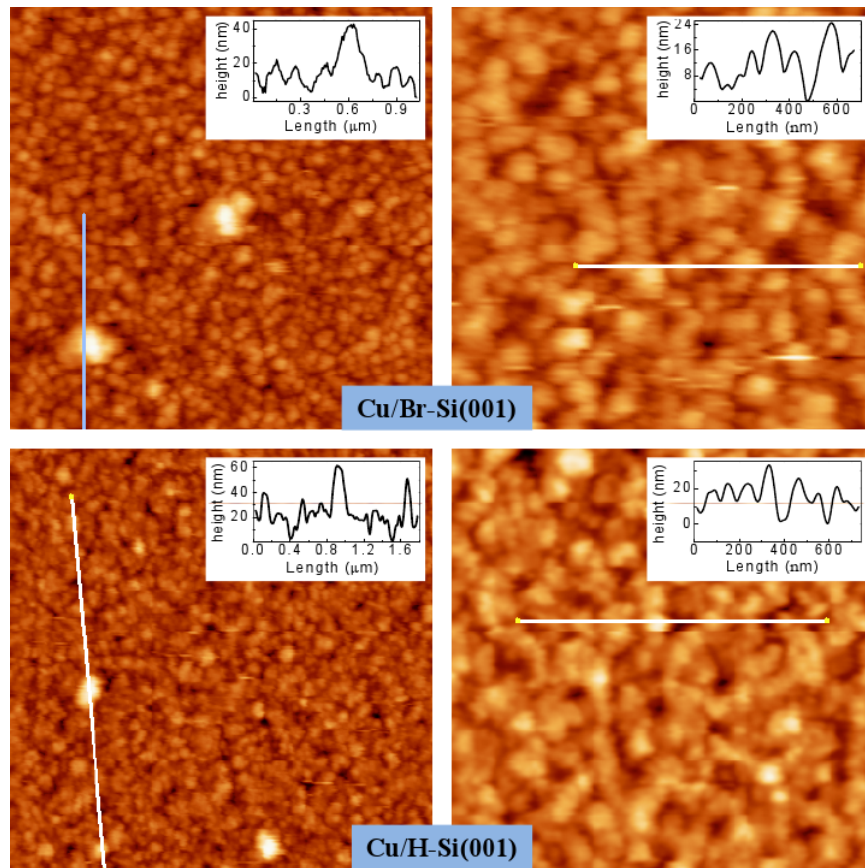
Figure 6.4: AFM images of scan size 2000×2000 nm^2 (left) and 1000×1000 nm^2 (right) along with line profiles showing height-variation (in nm) of the two samples.
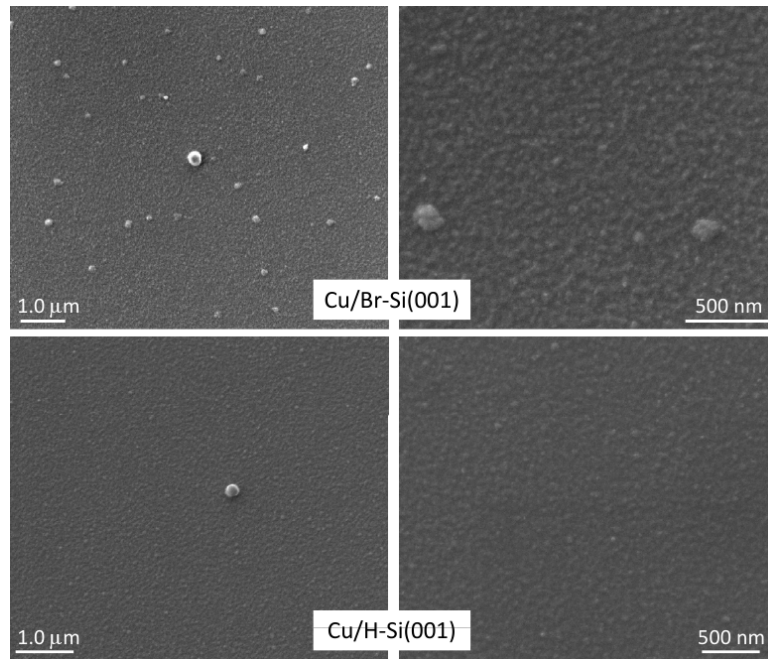
Figure 6.5: SEM images of Cu nanolayers on two differently pretreated Si substrates after prolonged dewetting and interdiffusion.

samples does not show faceting nature which is observed for directed crystalline or epitaxial growth.

6.2.2.2 Scanning electron microscopy

SEM images of two Cu films, after prolonged evolution due to dewetting and interdiffusion, are shown in Fig. 6.5. SEM image is taken in order to get an idea about the morphology in large scale. Island like features have been observed in both samples. But few big sized 3D-islands are randomly scattered on the surface as observed in the AFM images. These islands is prominent in Br-passiaveted sample relative to H-passivated sample which is also consistent with AFM morphology.
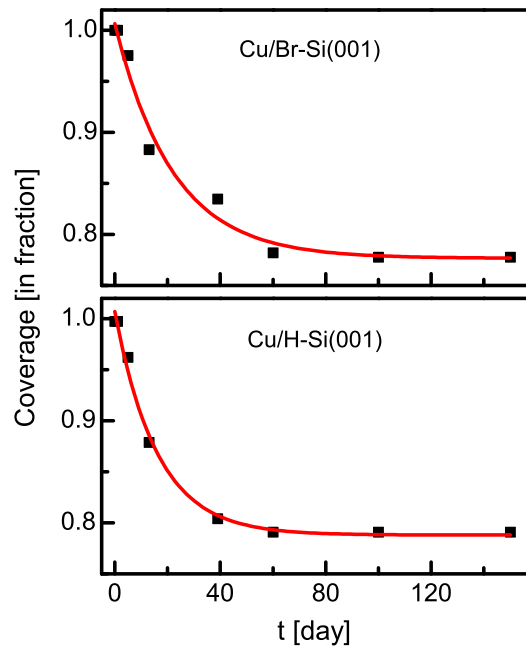
Figure 6.6: Variation in coverage of Cu (from original L1 layer) with time on two differently pretreated Si(001) substrates in two panels. Solid line represents simple exponential decay.

6.2.3 Dewetting and Interdiffusion

In order to understand the evolution of Cu nanolayer, the variation of its coverage in the dense wetted layer L1 has been calculated from EDPs for both samples. After normalizing the electron density at different time by the bulk value (2.27 $e/\text{Å}^3$) it is plotted as a function of time in Fig. 6.6. Apart from this layer, also there is large variation of L2 layer due to dewetting of Cu with time. Here we have only considered L1 layer evolution, because this layer is of very high density which is more sensitive to x-ray. However, it is evident from Fig. 6.6 that the nature of variation of Ag nanolayer coverage C for two samples are not much different. For the Cu/H-Si(001) sample, coverage decays more rapidly from the beginning in exponential nature compared to Cu/Br-Si(001) sample.

The variation of coverage can be quantitatively analyzed using following general relations

$$C(t) = (C_i - C_f)e^{-t/\tau} + C_f \;, \qquad (6.1)$$

where t is the measurement time, C_i and C_f are the initial and final coverage and τ is the decay time. Analysis of the time-evolution coverage data using Eq. 6.1 are shown in Fig. 6.6. Parameters obtained from the analysis are $C_i \approx 1$, $C_f \approx 0.78$ and $\tau \approx 22$ days for the Cu/Br-Si(001) sample; while $C_i \approx 0.99$, $C_f \approx 0.79$ and $\tau \approx 16$ days for the Cu/H-Si(001) sample. The value of τ for the former sample is quite large. The decay of Cu nanolayer just like Ag nanolayer described in chapter 5 can be related to the growth of oxide layer at the interface by desorbing the passivating elements like H and Br. From the previous study on Ag/Si as described in chapter 5 we have seen that the τ value is large in case of H-passivated Si surface compared to Br-passivated one. Whereas in this case τ value is lower for H-passivated surface. This thing can be understood by considering the fact that here since not only the dewetting takes place interdiffusion also takes place which may be responsible for slight decaying in coverage as well as lowering in τ value.

Diffusion length L_d has been calculated from the EDPs and plotted as a function of time which is shown in Fig. 6.7. L_d increases in similar fashion for two samples
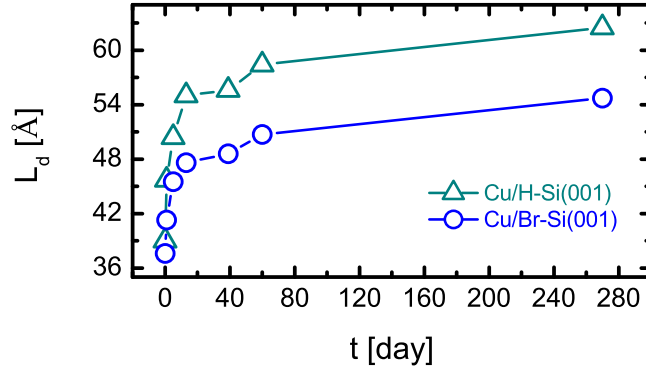
Figure 6.7: Diffusion length L$_d$ plot as a function of time t for two samples.

Table 6.1: Relevant parameters, such as the resistivity (ρ) at RT, the electronegativity (δ) in Pauling scale, the covalent atomic radii (R_a).

Element	ρ	R_a	δ
	[$\mu\Omega$-cm]	[Å]	
Au	2.2	1.44	2.54
Ag	1.6	1.53	1.93
Cu	1.7	1.38	2.00

just like similar fashion. For Cu/H-Si(001) sample L$_d$ increases from 39 Å to 63 Åwhereas for Cu/Br-Si(001) sample L$_d$ increases from 38 Å to 55 Å. It should be mentioned here that L$_d$ for Cu/O-Si(001) sample remains constant nearly around 35 Å. Cu diffusion in amount into native oxide covered Si is not negligible, rather it is comparable to other two samples.

In chapter 4 we have seen only the interdiffusion of Au into Si substrate whereas in chapter 5 we only observed dewetting of Ag on Si with time. No detectable diffusion of Ag into Si is being observed. Here in case of Cu/Si system we observed both phenomena i.e., interdiffusion and dewetting. One part diffuses into Si and another part dewets the Si surface with time. In the following we shall discuss the reason

behind the difference in reactivities of these three systems. In case of Au and Ag, though both materials are quite similar to each other, i.e., crystal structures, lattice constants and so on such drastic difference in reactivity has been observed. There is a very slight difference in covalent radius (tabulated in Table 6.1) which would not be responsible here for different reactivities. Now the only difference which is under consideration is the electronegativity, i.e., Ag is less negative than Au (given in Table 6.1) which causes the different reactivity [216]. Because the onset o the intermixing reaction in the Au-Si system was accompanied by the energy shift of $Si(2p)$ and $Au(4f)$ core levels due to electron transfer from Si to Au, it may be quite natural that more electronegative Au is more reactive than Ag. Therefore, the mechanism proposed by Itoh and Gibson [217] is more accurate to state that both the screening effect and the electron transfer must be responsible for the M-Si reaction. Namely, the former triggers the reaction and the latter i.e., electronegativity of the specific metal determines the final reactivity. Since the triggering effect or the breakage of sp^3 tetrahedral coordination in Si by Ag metallic overlayer is clearly shown by Rossi *et al.* [218], but the low electronegativity of Ag leads to rather weak reactivity. In case of Cu which shows intermediate tendency in reaction with Si can be understood considering the atomic size effect. Though the electronegativity of Cu (given in Table 6.1) is slightly greater than Ag, the covalent radius (given in Table 6.1) is smaller than Ag which is mainly responsible for diffusive interface.

6.3   Conclusions

The growth and evolution of Cu nanolayers on differently passivated Si(001) substrates at ambient condition have been studied. Initial compactness and smoothness of Cu nanolayer on the H-passivated and Br-passivated Si(001) surface are nearly same. Co-existance of dewetting and interdiffusion has been observed in Cu nanolayer deposited on these passivated Si(001) surfaces. Amount of dewetting and interdiffusion strongly depend on surface treatment. Diffusion of Cu into H-passivated Si surface is greater than Br-passivated surace whereas dewetting is

dominant in Br-passivated Si surface rather than H-passivated surface. The growth of dewetted 3D-island-like structures (Volmer-Weber-like mode) from comparatively wetted Cu nanolayer (Stranski-Krastanov-like mode) and moreover initially diffused nanolayer of Cu is propagating through Si are evident in both cases. Such evolution of growth is through dewetting (related to the change in the interfacial energy due to the oxide-growth), migration and coalesce of Cu, which can even produce 3D-islands on both passivated surfaces and also interdiffusion through native oxide free areas results in a very thin diffused nanolayer of Cu into Si. The growth-rate, size, number-density of 3D-islands and thickness, composition of diffused nanolayer depend on different types of passivations. These differences can be realized considering the growth-time of oxide (i.e. instability of passivated surface) which not only blocks the interdiffusion to give a control in the thickness as well as density but also enhances the dewetting, in-plane inhomogeneity of interfacial energy (i.e. inhomogeneous nature of passivation) and in-plane diffusion of Cu on the passivated surfaces.

Chapter 7

Langmuir-Blodgett film on passivated Si surface: Observation of hydrophilic and hydrophobic interaction

7.1 Introduction

Metal-organic films [49; 219] of well ordered structure and controlled thickness [147; 148] can be grown easily using Langmuir-Blodgett (LB) technique [136; 220]. Such LB films are ideal for testing basic physics of low-dimensional systems, viz. electrical transport, magnetism, and melting in two-dimensional (2D) systems [136–138], specific growth mechanism arising from different types of observed in-plane correlations[139–142], etc. These films also show unique properties and have promising applications in the field of biosensors, catalysis, nonlinear optics, microelectronics, and nanotechnology [9–16]. However, physical properties of LB films strongly depend on their structure. Defects [49], imperfection [51], and instabilities [143] in the structure are the main obstacles behind their proper applications. Defects,

---

Some parts of the presented work in this chapter are published in: Phys. Rev. B **81**, 045404 (2010), Chem. Phys. Lett. **500**, 90 (2010).

which are mainly observed in the LB films, are the 'pinhole' type defects [140; 144] and can partially be removed by increasing pH [47; 48] of or by dissolving different metal ions [49] in the water subphase. Different substrates have also been used to understand the substrate effects in controlling LB structure [49; 143; 147–149].

In this chapter, we systematically investigate three things: (1) role of passivating elements (such as H, Br and O) in the growth and stability of LB films, (2) role of metal ions (such as Ni^{2+} and Cd^{2+}) in the growth and stability of LB films and (3) the role of environments in the stability of the passivated surface as predicted from the growth of LB films.

7.2   Passivation dependent growth

It is well known that substrate surface condition plays important role in the growth and stability of any nanolayer on it [143; 221]. Substrate surface condition can be modified through different ways; by passivating with foreign atomic layer (such as hydrogen, bromine, etc.) or by growing self-assembled monolayer (of say silane). This essentially modifies the surface free energy or polarity of the surface and accordingly, wetting-dewetting or hydrophilic-hydrophobic nature of the surface can be tuned [72; 73; 152–154; 221]. Studies of LB films on some such modified substrates have already been carried out, which show that the different layered structure can indeed be grown [49; 51–53]. However, in-plane control or overall stability of such structure has not been studied well. On the other hand, strong influence has already been observed in the growth and stability (time evolution in-plane and out-of-plane structures) of metal nanolayer on differently passivated silicon substrates which is described in chapter 5, namely the interfacial instability at ambient conditions induces the wetting to dewetting transition in the Ag nanolayers, which then provides interesting nanostructures having different size, number density, and even crystallinity and/or epitaxy, depending on initial Si surface passivation. Such passivated Si surfaces also have different hydrophilic-hydrophobic nature, which can control the growth and stability of the LB films or can control the formation of

interesting metal-organic nanostructures. However, not much study has been made in this direction.

In this study, our aim precisely is to look into this matter and for that nickel arachidate (NiA) LB films have been deposited on differently-terminated Si(001) substrates. The structure of the LB films and its evolution with time have been monitored using XRR and AFM techniques. XRR data were collected as a function of time. AFM images were collected in tapping mode to minimize the tip induced damage of soft materials, few days after deposition.

7.2.1 Results and discussion

7.2.1.1 X-ray reflectivity and electron-density profile

XRR data and analyzed curves of NiA LB films deposited by 1 stroke and 3 strokes on freshly oxide grown OH-terminated Si(001) substrates are shown in Fig. 7.1. EDPs are shown in the inset of Fig. 7.1. EDPs confirm that the NiA molecules are attached to the substrates through heads and formed single asymmetric monolayer (AML, i.e., molecules in asymmetric configuration [222] with hydrophilic head in one side and hydrophobic tails in other side) structure on 1s-NiA/OH-Si LB film, while formed one AML followed by one symmetric monolayer (SML, i.e., molecules in symmetric configuration [222] with Ni containing head in the middle and hydrocarbon tails in both sides) structures on 3s-NiA/OH-Si LB film. EDP of 3s-NiA/OH-Si LB film also suggests that the coverage of the top SML structure is similar to that of bottom AML structure. It can be noted that the thickness of one SML is double that of one AML. No changes have been observed in the XRR curves and its analysed EDPs with time, suggesting clearly that such LB films are very stable.

Time-evolution XRR data and analyzed curves of NiA LB film on HF treated Si(001) substrate, deposited by 2 strokes, are shown in Fig. 7.2. EDPs obtained from the analysis are shown in the inset of Fig. 7.2. EDPs suggest that the NiA molecules are attached to the substrate through tails and form one SML. However, the height and width of the peak (corresponding to the heads) in the EDPs clearly
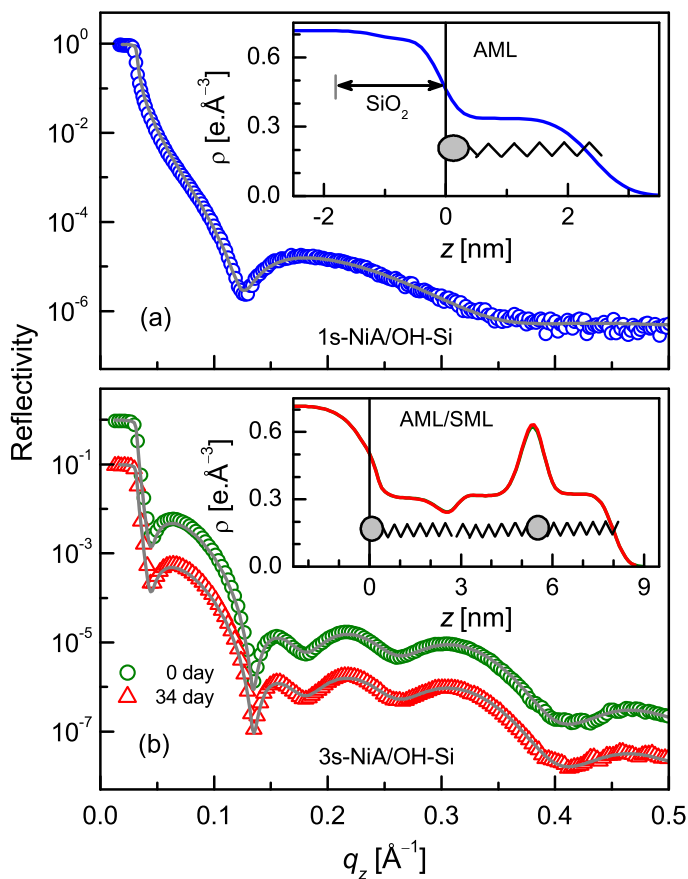
Figure 7.1: XRR data (different symbols) and analyzed curves (solid line) of NiA LB films deposited on OH-terminated Si(001) substrates, (a) after deposition by 1 stroke and (b) as a function of time after deposition by 3 strokes (curves are shifted vertically for clarity). Insets: corresponding EDPs showing possible structures and stability of LB films on OH-terminated surfaces.
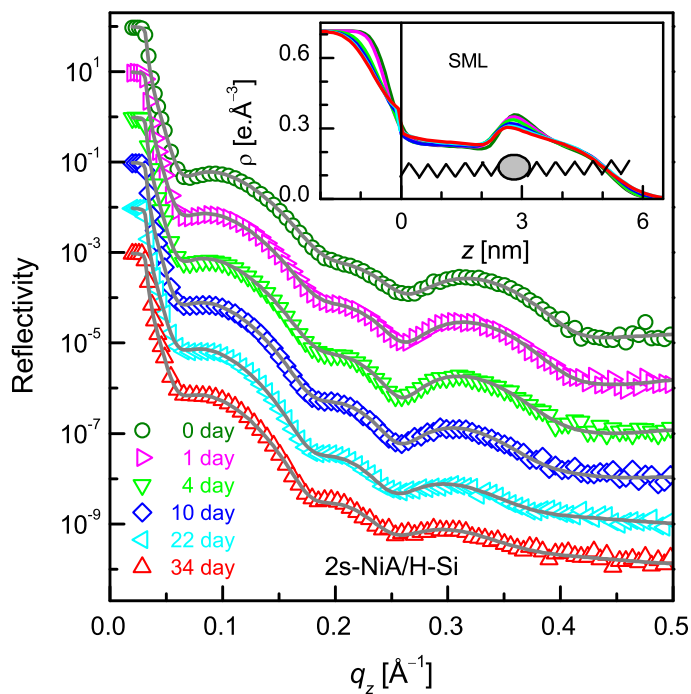
Figure 7.2: Time-evolution XRR data (different symbols) and analyzed curves (solid line) of NiA LB film on H-terminated Si(001) substrate, deposited by 2 strokes (curves are shifted vertically for clarity). Insets: corresponding EDPs showing possible structures and stability of LB films on H-terminated surfaces.

indicate that the coverage as well as the organization of molecules in the SML are less compared to that of 3 strokes NiA LB films deposited on OH-terminated Si(001) substrates. Also, the NiA LB film on the H-terminated Si(001) substrate is not very stable. Changes with time, although small, are evident from the EDPs. The electron densities of the top portion of the substrate and the head region of the film decrease with time. The first one can be associated with the growth of native oxide on silicon, which takes place even in presence of covered layer [43; 221], while the latter one might be due to the reorganization (or configurational change) of the NiA molecules. To understand such changes or instability of the film quantitatively, the oxide coverage (C_{ox}) at substrate surface and the head amount (M_H) in SML configuration have been plotted in Fig. 7.3. The growth of C_{ox} or the decay of M_H can be analyzed using following relations:

$$C_{\mathrm{ox}}(t) = C_{\min} + \Delta C(1 - e^{-t/\tau_{\mathrm{ox}}}) \tag{7.1}$$

$$M_H(t) = M_{\min} + \Delta M e^{-t/\tau_H} \tag{7.2}$$

where $C_{\min}$ is the minimum oxide coverage present initially, $C_{\min} + \Delta C$ is the maximum oxide coverage reached finally, ΔC is the change in coverage and τ_{ox} is its growth time, while $M_{\min} + \Delta M$ is the maximum head amount present initially, $M_{\min}$ is the minimum head amount reached finally, ΔM is the change in head amount and τ_H is its decay time. The analyzed curves obtained using Eqs. (7.1) and (7.2) are shown in Fig. 7.3. The analysis shows that the change in both the parameters with time is about 13%, while the value of τ_{ox} is about 6 days and that of τ_H is about 8 days.

XRR data and the analyzed curves of NiA LB films on Br-terminated Si(001) substrates, deposited by different numbers of strokes, are shown in Fig. 7.4. Corresponding EDPs are shown in the inset of Fig. 7.4, which indicate that in all the cases the attachments of NiA molecules with Br-terminated Si surfaces are partially through heads and partially through tails. EDPs of the films deposited by 1 and 2 strokes are almost similar. In both cases the Br-terminated Si surface is covered
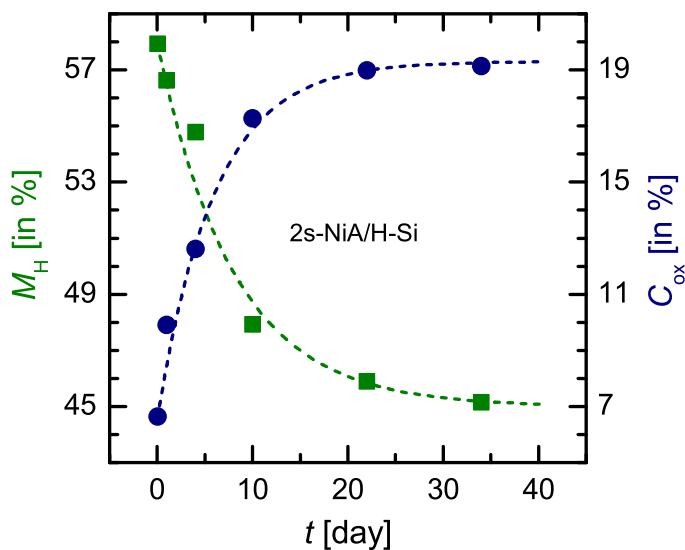
Figure 7.3: Head amount (M_H) in SML configuration and oxide coverage at substrate surface as a function of time (t) for NiA LB film on H-terminated Si(001) substrate, deposited by 2 strokes.

with two different structures, namely AML and SML. EDP of the film deposited by 3 strokes is quite interesting. Deconvolution of EDP suggests that, in such film, Br-terminated Si surface is covered with four different structures, such as AML, SML, AML/SML, and SML/SML. Also no appreciable change in the EDP has been observed as a function of time, suggesting such structures of NiA LB films on the Br-terminated Si surface are quite stable.

7.2.1.2 Atomic force microscopy and topography

AFM images of NiA LB films deposited on differently-terminated Si(001) substrates after prolonged evolution are shown in Fig. 7.5. Topography is composed of different heights or layers, which are indicated by the number (in unit of AML length) in the images. It is again necessary to mention that the height of SML ($\sim$5.5 nm) is double of that of AML ($\sim$2.7 nm). So, the numbers 0, 1, 2, 3, and 4 correspond to the heights of Si surface (reference plane), AML ($\sim$2.7 nm), SML ($\sim$5.5 nm), AML/SML
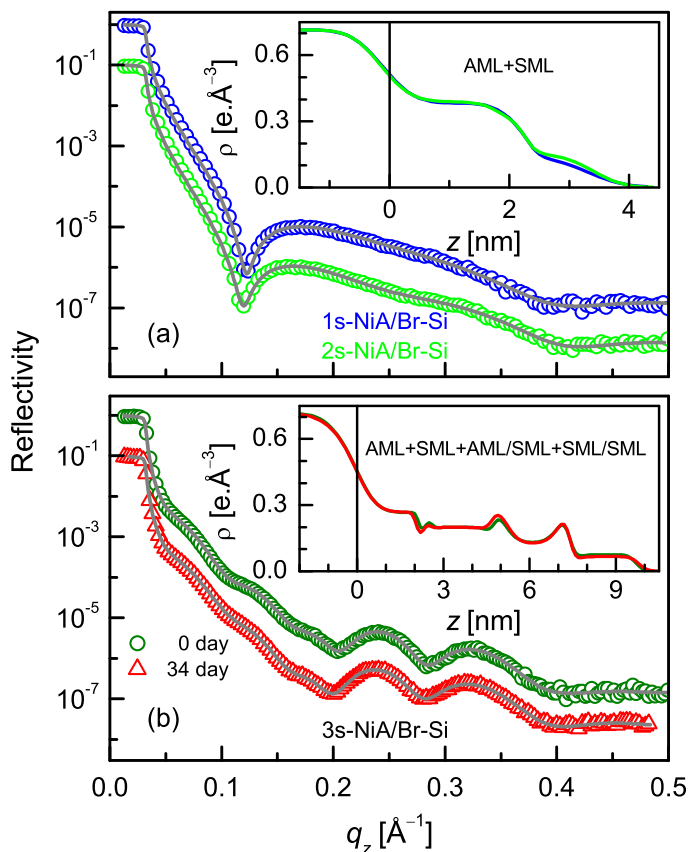
Figure 7.4: XRR data (different symbols) and analyzed curves (solid line) of NiA LB films on Br-terminated Si(001) substrates (a) after deposited by 1 and 2 strokes and (b) at two time intervals after deposited by 3 strokes. Curves are shifted vertically for clarity. Insets: corresponding EDPs showing possible structures and stability of LB films on Br-terminated surfaces.
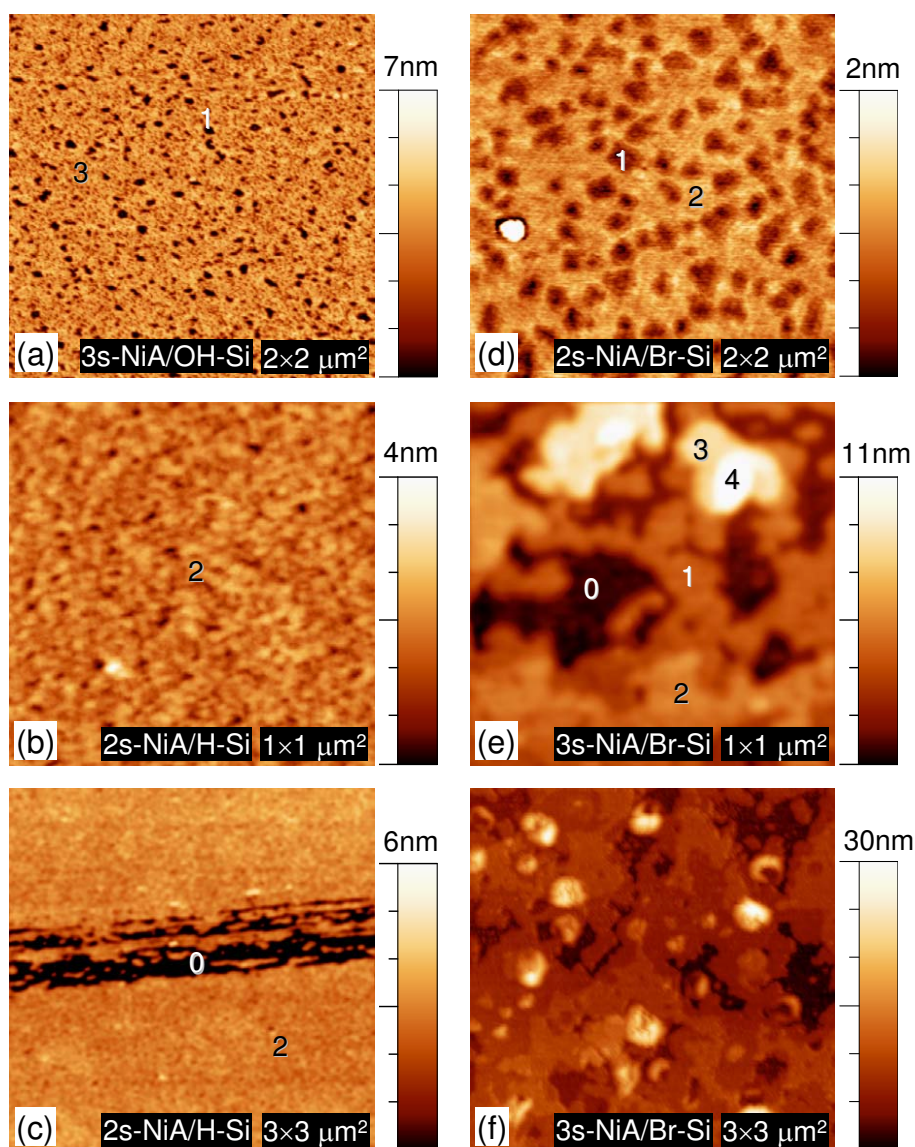
Figure 7.5: AFM images showing topography of NiA LB films on differently-terminated Si(001) substrates: (a) on OH-terminated Si(001) substrates, deposited by 3 strokes, of scan size 2×2 μm^2, (b) and (c) on H-terminated Si(001) substrate, deposited by 2 strokes, of scan sizes 1×1 and 3×3 μm^2, respectively, (d) on Br-terminated Si(001) substrates, deposited by 2 strokes, of scan size 2×2 μm^2, (e) and (f) on Br-terminated Si(001) substrate, deposited by 3 strokes, of scan sizes 1×1 and 3×3 μm^2, respectively. Presence of layers of different heights (in unit of AML length) are indicted by the numbers.

($\sim$8.2 nm), and SML/SML ($\sim$11.0 nm) structures, respectively. Topography of NiA LB film on OH-terminated Si surface, deposited by 3 strokes [Fig. 7.5 (a)], shows that the top surface is quite smooth (compact) with some pinhole defects, characteristics of LB films [48; 49; 140]. The observed heights of the pinhole type defects, i.e. the depths of the black regions from top surface are mostly about 5 nm with maximum about 8 nm. Considering maximum depth arising from the bare Si substrate, the thickness and the corresponding structure of the film are about 8 nm and AML/SML, respectively, consistent with the XRR analysis. On the other hand, though the heights of the majority of the defects, according to the AFM image, are about 5 nm (which corresponds to the absence of top SML structure), the actual heights of the majority of the defects are about 8 nm (corresponding to the absence of total AML/SML structure) as evident from the EDP (no significant decrease in the electron density of the top SML region compared to that of the bottom AML one). This difference can be understood by considering the convolution effect of the AFM tip with the small in-plane size pinhole defects, which restrict the estimation of actual depth. Defect-free or at least small size defects are expected for the LB films deposited at high pH compared to that for the normal pH one [48]. Topography of NiA LB film on H-terminated Si surface, deposited by 2 strokes [Fig. 7.5 (b)], shows that the top surface is relatively rough (less compact) although defect free. The relative height of the film compared to the scratched portion [Fig. 7.5 (c)], corresponds to the SML thickness, consistent with the XRR analysis. Topography of NiA LB film on Br-terminated Si surface, deposited by 2 strokes [Fig. 7.5 (d)], shows areas having two distinct heights. The height difference is about 2 nm. Considering the XRR results, low and high height areas can be identified as AML and SML, respectively. Topography of NiA LB film on Br-terminated Si surface, deposited by 3 strokes [Fig. 7.5 (e)], verifies the presence of four different structures, as obtained from the XRR results. It is necessary to mention that apart from such four structures, ring-shaped islands of large heights [Fig. 7.5 (f)] are also present. However, number or fractional coverage of those islands are very small and do not appear in the XRR results as they are insensitive to the analysis. From Fig. 7.6 it
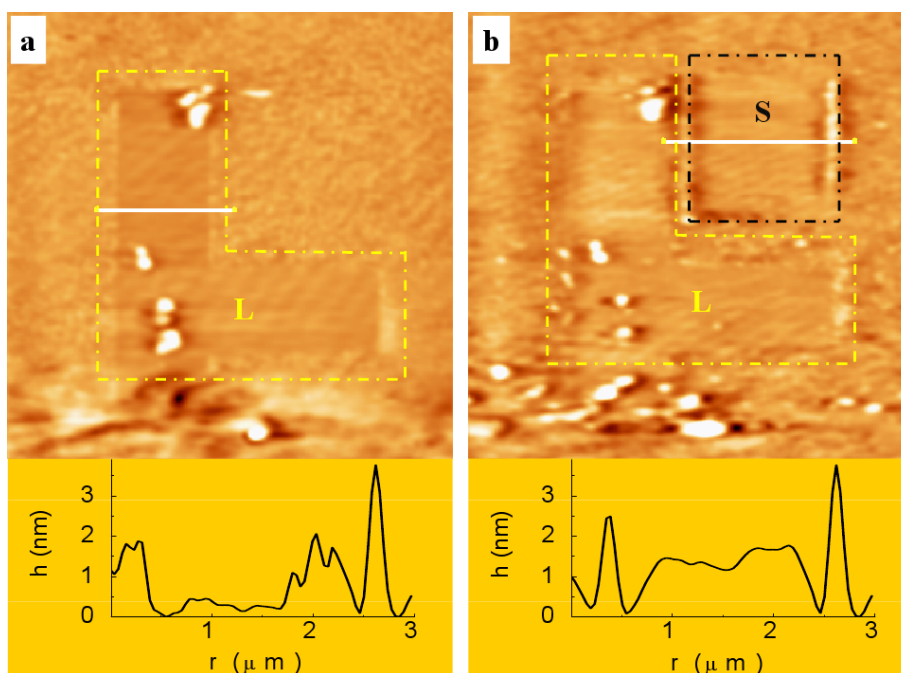
Figure 7.6: Scratch made by AFM tip in the 2s-NiA/H-Si sample. L shape (marked as L) and a square shape (marked as S) pattern.

is evident that the LB film on H-terminated Si surface can be easily scratched with AFM tip by applying force, just above 1.5 nN, unlike LB films on other terminated Si surfaces. L-shape pattern (marked as 'L') and a square shape pattern (marked as 'S') adjacent of L is created in the NiA LB film. Fig. 7.6 (a) shows only the L pattern i.e., before creation of S pattern whereas Fig. 7.6 (b) shows the image after the creation of S pattern besides the L pattern.

7.2.1.3 Structure and growth mechanism

The structures of the NiA LB films on differently-terminated Si substrates, as obtained from the EDP and topographic results, are shown schematically in Fig. 7.7. It can be noted that the hydrophilic or hydrophobic nature of the surface can be easily verified with necked eyes. As it is known that if the surface is hydrophilic, the water layer tries to wet the surface and if the surface is hydrophobic, it dewets. So, by observing the wetting or dewetting properties of the water with the surface,

155
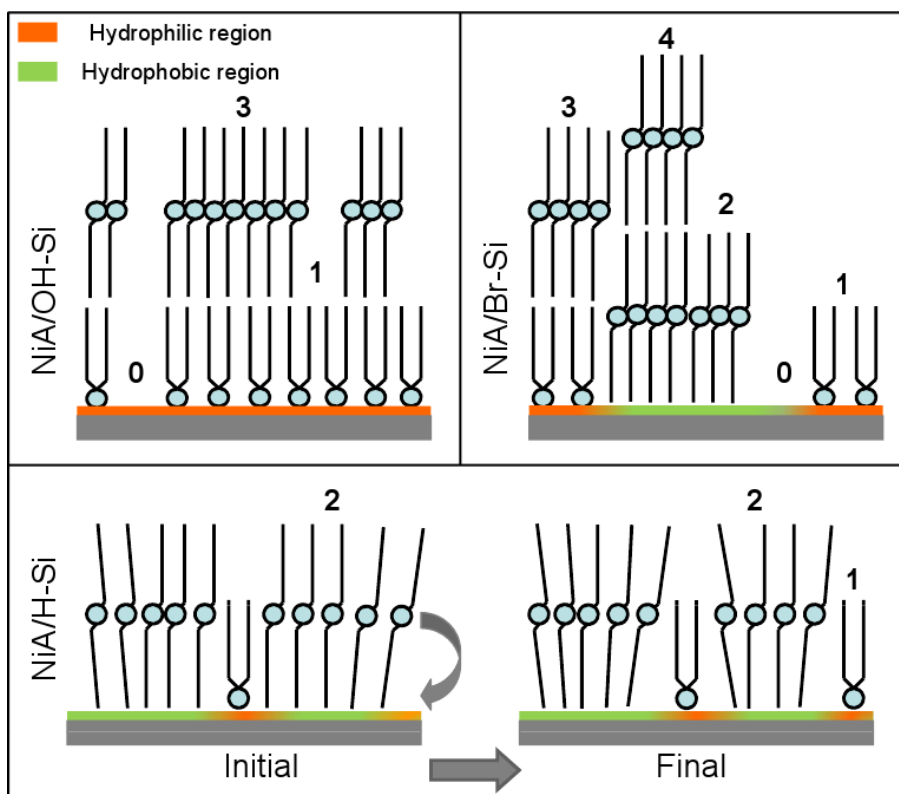
Figure 7.7: Schematic illustration of structures of NiA LB films on differently-terminated Si(001) substrates and their time-evolution. Different numbers indicate the heights (in unit of AML length) of a film on those areas with corresponding structures.

one can infer the nature of the surface, at least qualitatively. Regarding stability, it is well known that oxide passivated (here OH-terminated) Si surface is stable, but H- or Br-passivated Si surface is not so stable in ambient condition, even in the presence of overlayer [43; 221]. With time, H- or Br-passivated layer desorbs and native oxide layer grows. The growth time of oxide layer is, however, different for differently-passivated surface.

As the OH-terminated Si surface is hydrophilic in nature, the attachment of NiA molecules to the substrate is through hydrophilic heads, which takes place during first up stroke of deposition. Consequently, the first layer is AML and subsequent

layers are SMLs. Single SML forms after one complete down-up stroke. Accordingly, AML/(SML)$_n$ structure can be grown on OH-terminated Si substrate by n number of down-up strokes after first up stroke. The in-plane structure of the film is quite smooth, apart from pinhole defects. Presence of pinhole defects is the signature of less number of molecules in a layer, which is probably related to the transfer ratio less than one and/or further dissolution. Observed structure (shown schematically in Fig. 7.7) can be understood considering strong in-plane (head-head) interaction of NiA molecules compared to out-of-plane (substrate-head) interaction and uniform nature of the passivated Si surface. Combination of both probably allow NiA molecules to diffuse in-plane to form compact smooth structure separated by defects. Since the OH-terminated Si surface is stable, the LB structure form on it is also stable.

The H-passivated Si surface behaves hydrophobic in nature and correspondingly hydrophobic tails of NiA molecules attached to the substrate during first down stroke of deposition. After complete down-up stroke, the layer that form on the substrate is SML, which will be same for subsequent down-up strokes. Accordingly, SML/(SML)$_n$ structure can be grown on the H-terminated Si surface by n number of down-up strokes after first down-up stroke. It can be noted that no pinhole defects have been observed (from AFM), although there are less number of molecules in a layer (as evident from EDP), which can be understood considering inhomogeneous and unstable natures of the H-passivated Si surface [221]. Inhomogeneous nature probably imposes restriction in the in-plane diffusion of NiA molecules through tails within hydrophobic domains, while the growth of hydrophilic region through open space destabilizes the nearby molecules, making the in-plane structure comparatively rough and less compact. Additionally, the in-plane and out-of-plane interactions of NiA molecules on H-terminated surface are through tail-tail and substrate-tail, respectively, unlike NiA molecules on OH-terminated surface. Such different interactions can also play some role in making different structure.

The Br-passivated Si surface is whether hydrophilic or not, is not known. However, it is known that the Br-passivated Si surface is more unstable than H-passivated
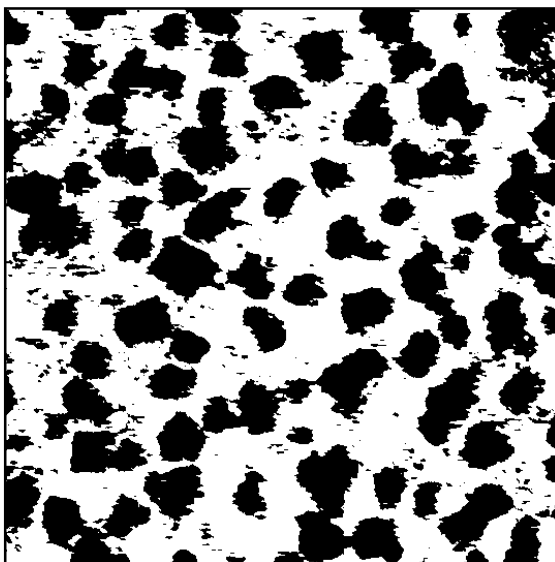
Figure 7.8: Schematic presentation of Br-passivated Si(001) surface showing presence of both hydrophobic (white) and hydrophilic (black) areas, arising from inhomogeneous nature of passivation. The surface areas, where native oxide layer already grown, are considered hydrophilic, while the area, which till remains Br-passivated, is considered hydrophobic.

Si surface [43; 221] and inhomogeneous in nature. So, it is expected that prior to deposition, oxide layer might have grown on some portion of the Br-treated Si surface by replacing the Br atom. This has been shown schematically in Fig. 7.8. The areas, which are weakly passivated (shown by black color) can change easily to oxide covered one, thus becoming hydrophilic, while other areas, which are strongly passivated (shown by white color) still remain Br-passivated and probably behave like hydrophobic.

Deposition of NiA LB film on Br-passivated Si substrate, by 1 stroke or 2 strokes, show nearly similar structure. By deposition through single up stroke, heads of NiA molecules are expected to attach with the hydrophilic portion of the substrate and accordingly, AML structure with partial coverage, is only expected. However, in practice SML structure is also observed. The coverage of the film, combining AML and SML, is quite good as evident from the EDP [Fig. 7.4 (a)]. This can occur either by direct attachments of heads and tails to the hydrophilic and hydrophobic portions, respectively or through continuous diffusion and configurational change of some of the NiA molecules from initially attached hydrophilic to nearly hydrophobic portions thereby enabling further attachment to the hydrophilic portion during single up stroke. Any such unusual process can takes place if the inhomogeneous nature of the substrate creates perturbation in the Langmuir monolayer or if the flipping speed is much higher than deposition speed. In case of deposition through a complete down-up stroke, tails of NiA molecules are attached to the hydrophobic portion of the substrate during down stroke, while heads are attached to the hydrophilic portion during up stroke. Accordingly, both AML and SML structures grow on Si surface, as observed experimentally.

In subsequent down-up stroke of deposition, SML structure is expected to grow above the previous one and accordingly, $AML/(SML)_n + SML/(SML)_n$ structure is expected to form by n such down-up strokes. In practice, we observed $AML/(SML)_{0,1,..n} + SML/$ structure with some ring shaped islands of large heights. Due to the presence of both hydrophobic and hydrophilic regions, strain is probably developed in the structure across the hydrophobic/hydrophilic interface. Such strain, which is developed in the

film by 1 or 2 strokes of deposition, will try to release. We propose that in subsequent deposition this release takes place by flipping of some molecules from the substrate and dumping it near that interface. Large heights ring shaped islands are formed due to this dumping, while AML or SML structure again formed by deposition in the region from where the materials have been flipped off. If this is the process, then size and shape of the ring should be related to those of the hydrophobic areas in the Br-terminated surface [i.e., AML areas in Fig. 7.5(d) or black areas in Fig. 7.8]. Although there are some similarities, we find deviation as well. So further studies are require for proper understanding.

7.3 Metal ion dependent growth

The unusual structures and stability that is observed for NiA LB films, may change with changing headgroup containing metal ions. Indeed, in some works [50; 223], it has been observed that with change of metal ions the morphology of the films on hydrophilic substrate (OH-terminated) changes drastically. The head-head interaction [54] and metal ion-hydrocarbon tail bond strength [50] dictates the final morphology of the grown film.

Similar to NiA LB films, XRR and AFM measurements were carried out to investigate the structure and time evolution of CdA LB film on three differently treated Si surfaces. Also by comparing the structures of the NiA and CdA LB systems, we have tried to find out the role of metal ion in growth and stability of the film.

7.3.1 Results and discussion

7.3.1.1 X-ray reflectivity and electron-density profile

XRR data of the 3s-CdA/OH-Si sample collected initially and after 21 days are shown in Fig. 7.9, which are nearly identical. Both data were analyzed considering a thin oxide layer on top of Si substrate followed by two layers of CdA molecules:
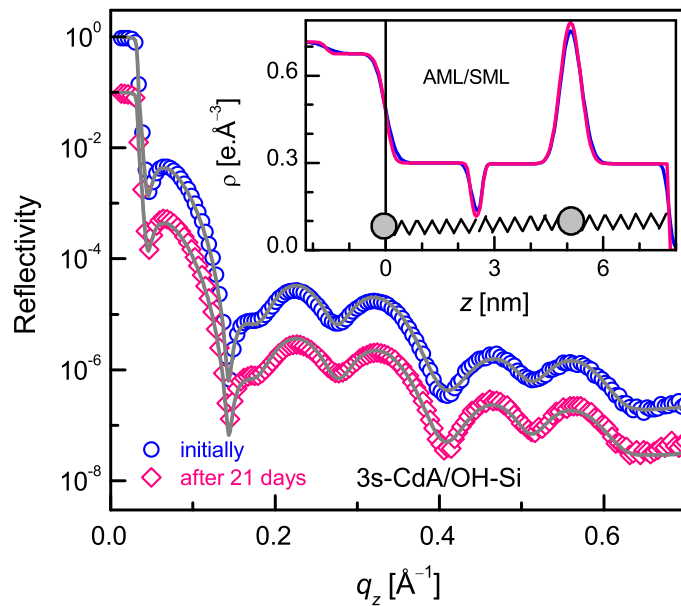
Figure 7.9: Time-evolution XRR data (different symbols) and analyzed curves (solid line) of CdA LB film on OH-passivated Si substrate, deposited by three strokes. Data and curves are shifted vertically for clarity. Inset: corresponding EDPs showing possible structure.

Figure 7.10: Time-evolution XRR data (different symbols) and analyzed curves (solid line) of CdA LB film on H-passivated Si substrate, deposited by two strokes. Data and curves are shifted vertically for clarity. Inset: corresponding EDPs showing possible structure.

AML first and SML on top it. Best fitted XRR curves thus obtained are shown in Fig. 7.9 and corresponding EDPs are in the inset. EDPs show that the AML/SML structure of the film is near perfect, compact ($\sim 95\%$ coverage, considering the electron density of the tail portion (ρ_{tail}) of a perfect and compact structure (either AML or SML) is about 0.32 e.$\mathring{A}^{-3}$) and stable in ambient condition. Also compared to the film-substrate interfacial roughness ($\sigma_{\text{in}} \approx 5$ $\mathring{A}$), the top surface roughness of the film ($\sigma_{\text{top}} \approx 3$ $\mathring{A}$) is found to be quite small and decreases further (to $\sigma_{\text{top}} \approx 2$ $\mathring{A}$) with time. Width of the head portion of the SML structure (d_{H}), obtained from the FWHM of the peak, is ~ 8 $\mathring{A}$.

XRR data of the 2s-CdA/H-Si sample collected initially and after 33 days are shown in Fig. 7.10. Small changes in the XRR data are observed with time, namely slight smearing of peak at $q_z \approx 0.3$ $\mathring{A}^{-1}$ and marginal right shift in the position of dip at $q_z \approx 0.4$ $\mathring{A}^{-1}$ and peak at $q_z \approx 0.5$ $\mathring{A}^{-1}$. In order to understand the

162

structure of the film and its evolution with time, both reflectivity data were analyzed considering a thin layer on top of Si substrate followed by SML of CdA molecules. Best fitted XRR curves thus obtained are shown in Fig. 7.10 and corresponding EDPs are in the inset. It is clear from the EDPs that the structure of the film remains almost unchanged with time. What is changed is the film-substrate interfacial region, namely the decrease of electron density due to the formation of oxides at Si surface. Interestingly, such change in the interface can not disturb the quite perfect and compact ($\sim 80\%$ coverage) SML structure of the film. The top surface roughness of the film ($\sigma_{\text{top}} \approx 4$ Å) is found quite small compared to the film-substrate interfacial roughness ($\sigma_{\text{in}} \approx 8$ Å), indicating the tendency of CdA molecules to form ordered SML structure. This tendency continues with time and improves the ordering even after the formation of oxides at the interface, which is evident from the further decrease of top surface roughness (to $\sigma_{\text{top}} \approx 3$ Å). The value of d_{H} is ~ 8 Å, which means that the ordering of the head-groups of this film is comparable to that of the 3s-CdA/OH-Si sample.

XRR data and analyzed curves of 1s-CdA/Br-Si, 2s-CdA/Br-Si and 3s-CdA/Br-Si samples are shown in Fig. 7.11. EDPs obtained from the analysis of XRR data are included in the insets of Fig. 7.11. EDP suggests that the AML structure with reduced thickness is formed on Br-terminated Si surface by single up stroke of deposition. Reduced thickness probably indicates imperfect nature of the film. In the XRR data of 2s-CdA/Br-Si and 3s-CdA/Br-Si samples, small hump near $q_z = 0.18$ Å^{-1} is observed initially, which vanishes with time. However, from the EDPs not much change is observed in the films with time. The structure of the 2s-CdA/Br-Si sample is AML+SML. The reduced thickness observed for both kind of layers is related to their imperfect nature. The amount of SML molecules are relatively small compared to AML molecules. The amount of latter seems to be comparable to that in the 1s-CdA/Br-Si sample. Due to the imperfect nature of the film some heads are always contributing in the electron density of tail portion. Considering $\rho_{\text{tail}} \approx 0.4$ e.Å^{-3} for full coverage with imperfect structure, the coverage of 1s-CdA/Br-Si sample with AML structure is about 75%. The coverage of 2s-CdA/Br-Si sample with AML
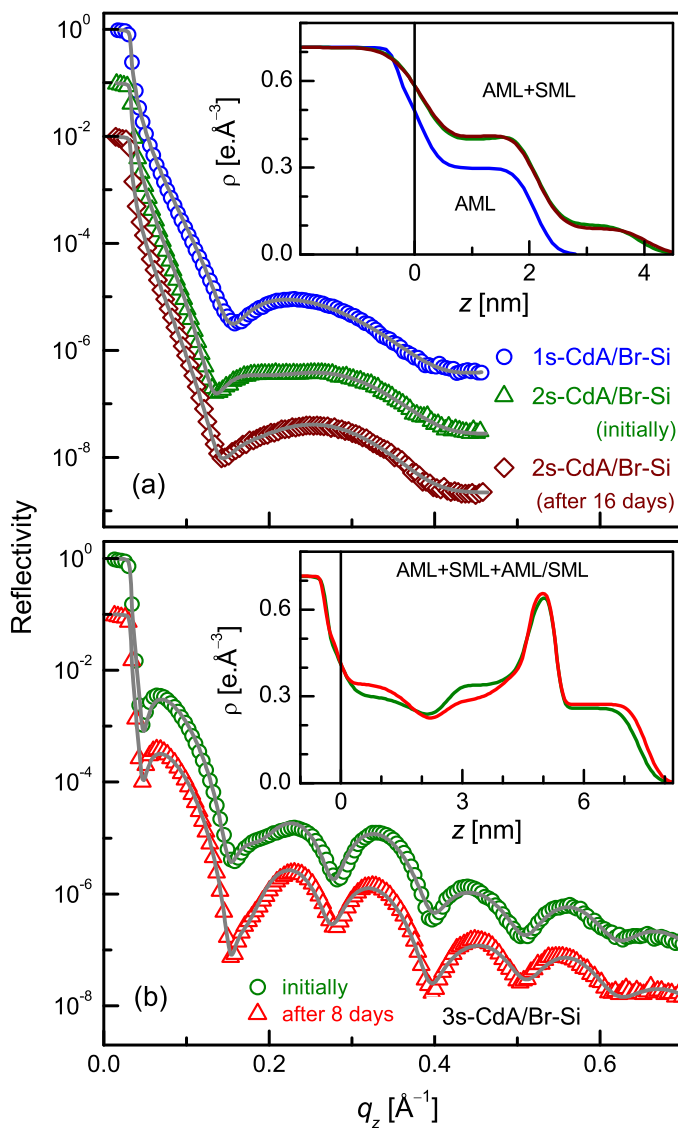
Figure 7.11: Time-evolution XRR data (different symbols) and analyzed curves (solid line) of CdA LB films on Br-passivated Si substrates, deposited by (a) one and two strokes and (b) three strokes. In each panel, data and curves are shifted vertically for clarity. Inset: corresponding EDPs, indicating possible structures.

structure is again 75%, which increases marginally with time and rest is with SML structure decreases accordingly. This indicates that the imperfect structures are quite stable.

EDPs of the 3s-CdA/Br-Si sample (inset of Fig. 7.11(b)), are slightly different from those of 3s-CdA/OH-Si sample (inset of Fig. 7.9), which indicates the presence of other structures apart from AML/SML structure. To find out all the structures, EDPs of the 3s-CdA/Br-Si sample were deconvoluted. It is found that initially the film consists of two different structures: AML/SML and SML, of which AML/SML is the majority. In SML structure not all molecules lie in same vertical position, some are attached directly to the substrate (labeled as B1) and others are slightly shifted upwards (labeled as B2). With time additional AML structure is found and the coverage of AML/SML structure increases. Both happens in expanse of SML structure (B1 and B2), the coverage of which decreases with time.

7.3.1.2 Atomic force microscopy and topography

Typical AFM images of CdA LB films deposited on differently treated Si(001) substrates are shown in Fig. 7.12. Corresponding model structures are also shown in Fig. 7.12. AFM image of 3s-CdA/OH-Si sample [Fig. 7.12(a)] shows that it consists of pinhole-type defects, which are large in number but small in size. Otherwise the surface is very smooth. Maximum depth of the defects is about 8 nm, which corresponds to the Si surface relative to the AML/SML structured smooth film. Considering the XRR results, pinhole-like defects cover about 5% of the surface. Fig. 7.12(d) schematically shows the structure of the film. AFM image of 2s-CdA/H-Si sample [Fig. 7.12(b)] shows that the top surface of the film is quite smooth, which is consistent with the XRR results. However, AFM images collected in larger length scale (not shown here) indicate the presence of some line-strip like scratches in smooth film. Although the origin of such scratches is not clear, their presence probably lower the coverage of the film to $\sim 80\%$, as predicted by EDP. Also, such scratches help to estimate the film thickness, and hence the structure of the film, which is
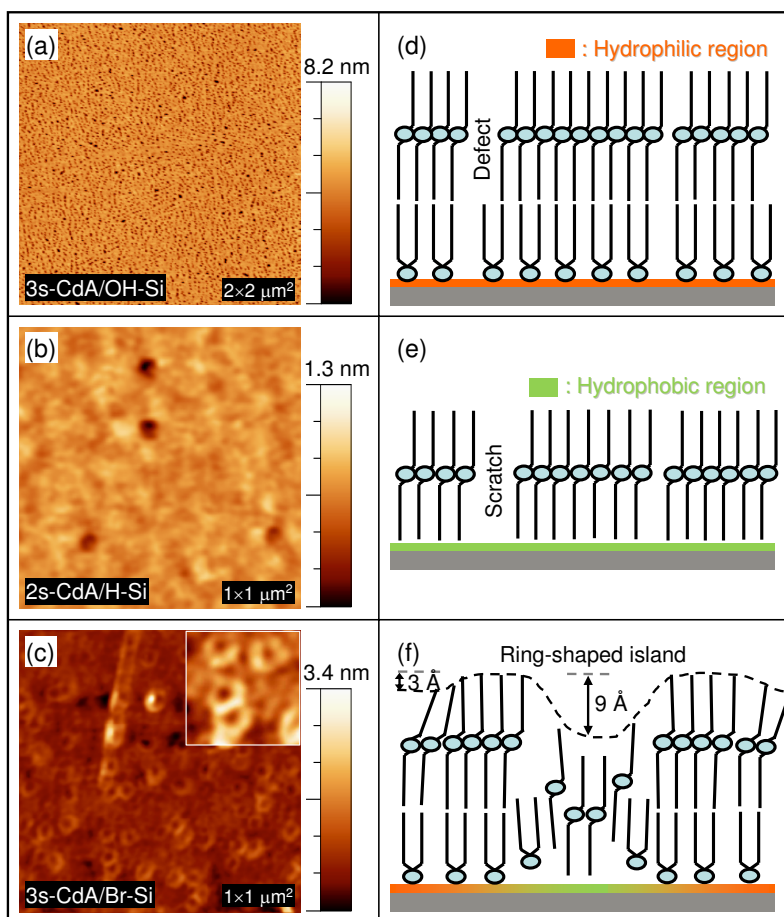
Figure 7.12: AFM images showing topography of CdA LB films (a) on OH-terminated Si substrate, deposited by three strokes, of scan size 2×2 μm^2, (b) on H-passivated Si(001) substrate, deposited by two strokes, of scan size 1×1 μm^2 and (c) on Br-terminated Si substrate, deposited by three strokes, of scan size 1×1 μm^2. Inset: Magnified image of scan size 200×200 nm^2. (d)-(f) Model structures of the films corresponding to the AFM images (a)-(c).

SML as shown schematically in Fig. 7.12(e). AFM image of 3s-CdA/Br-Si sample [Fig. 7.12(a)] is quite interesting. It shows the presence of ring-shaped islands having size about 70 nm and annular width about 25 nm. However, the ring-shaped islands do not lie on a flat surface, which is clear from the magnified view as shown in the inset, rather the depth inside (~ 9 Å) is more compared to the depth outside (~ 3 Å). Considering the XRR results, the structures corresponding to the inside and outside portions of the ring-shaped island are SML and AML/SML, respectively. The structure of the island itself is also AML/SML, but, such structure is probably more compact and order compared to that of the outside portion, which gives rise small height difference. This is shown schematically in Fig. 7.12(f). It is necessary to mention that no such ring-shaped islands are present in 1s-CdA/Br-Si and 2s-CdA/Br-Si samples.

7.3.1.3   Structure formation mechanism of LB films

In order to understand the mechanism behind the formation of different structures of CdA LB films on differently passivated Si surfaces, let us first compare the structures of the CdA LB films with those of the NiA LB films presented earlier. Table 7.1 summarizes different structures present in CdA and NiA films on three differently passivated Si surfaces deposited in different number of strokes. Also different parameters, such as film-substrate interfacial roughness (σ_{in}), top surface roughness of the film (σ_{top}) and head-width corresponding to the SML structure (d_{H}) for LB films on OH-Si and H-Si substrates are included in Table 7.1, which will be important in understanding the differences in the structures.

On OH-terminated Si substrates, both CdA and NiA LB films form AML structure in single up stroke of deposition and AML/SML structure in three strokes of deposition, which are consistent with the hydrophilic nature of the OH-terminated Si substrate. Film-coverage ($\sim 95\%$) and film-substrate interfacial roughness of the 3s-CdA/OH-Si sample are found similar to those of the 3s-NiA/OH-Si sample, indicating that these two parameters are film (i.e. head-groups) independent and

Table 7.1: Different layered structures for CdA and NiA LB films on differently passivated Si substrates deposited by different number (n) of strokes and relevant parameters such as film-substrate interfacial roughness (σ_{in}), top surface roughness of the film (σ_{top}), and head-width (d_H) corresponding to SML structure obtained from the analysis of XRR data and AFM images.

LB film	n	OH-Si σ_{in} (Å)	σ_{top} (Å)	d_H (Å)	Structure	H-Si σ_{in} (Å)	σ_{top} (Å)	d_H (Å)	Structure	Br-Si Structure
CdA	1				AML				-	AML
	2				-	8-12	4-3	8	SML	AML+SML
	3	5	3-2	8	AML/SML				-	AML+SML+AML/SML
NiA	1				AML				-	AML+SML
	2				-	6-10	9-14	11	SML	AML+SML
	3	6	7	10	AML/SML				-	AML+SML+AML/SML/SML

mainly related to the nature of the substrate. While the values of σ_{top} and d_{H} for the 3s-CdA/OH-Si sample are found smaller compared to those for the 3s-NiA/OH-Si sample, suggesting better ordering of the Cd head-groups compared to the Ni head-groups. With time, such ordering either remains same (for NiA LB film) or even improves (for CdA LB film). The latter is evident from the decrease (whatever small) in the value of σ_{top} (from 3 Å to 2 Å) with time.

CdA LB film forms SML structure on H-terminated Si substrate in two strokes of deposition similar to the NiA LB film, which is well understood from the hydrophobic nature of the H-terminated Si substrate. Comparison of different parameters, namely σ_{top} and d_{H} for the two films suggests that the ordering of the Cd head-groups is better compared to the Ni head-groups, while the AFM images and the EDPs suggest that the structure of the CdA LB film is more compact. However with time, oxides grow on the Si substrate, which increases the film-substrate interfacial roughness. Oxide growth destabilizes and deteriorates the structure of the NiA film, which is evident from the increase in the value of σ_{top} (from 9 Å to 14 Å) with time. However, unlike NiA film, oxide growth does not deteriorate the structure of the CdA film, rather improves the ordering, which is evident from the decrease (whatever small) in the value of σ_{top} (from 4 Å to 3 Å) with time.

CdA and NiA LB films on Br-terminated Si substrate deposited by two (down-up) strokes, show similar (AML+SML) structure. This is consistent with the coexisting (hydrophilic-hydrophobic) nature of the Br-terminated Si surface, where SML structure is formed on the hydrophobic portion during down-up stroke and AML structure is formed on the hydrophilic portion during up stroke only. Due to the inhomogeneous and unstable natures of the Br-terminated Si surface, it is expected that prior to the deposition, oxide layer might have grown in some portion of the surface replacing the Br atoms. Large coverage of AML structure compared to SML structure suggests that the Br-terminated Si surface is mostly ($\sim 75\%$) composed of hydrophilic portion and remains unchanged, while imperfect nature of both AML and SML structures indicates that the hydrophilicity and hydrophobicity of the respective portions of such Si surface are weak.

Structures of CdA LB films on Br-terminated Si substrates deposited by odd number of strokes are quite different from those of NiA LB films. In single up stroke of deposition, CdA LB film forms AML structure with partial coverage, while both AML and SML structures are observed for NiA LB film. Due to the coexisting (hydrophilic-hydrophobic) nature of the Br-terminated Si surface, growth of AML structure on the hydrophilic portion of the substrate in single up-stroke of deposition, is quite natural, which is the case for the CdA LB film. Also this suggests that during up-stroke of deposition, continuous diffusion and configurational change (or flipping) of molecules from hydrophilic to nearly hydrophobic portion, which was proposed for the unusual AML+SML structure of the NiA LB film, do not take place in case of CdA molecules.

In three stokes of deposition, CdA LB film forms AML+SML+AML/SML structure on Br-terminated Si substrate, unlike NiA LB film, which forms AML+ SML+AML/SML+SML/SML structure. The formation of structure for the NiA LB film has been understood considering further growth on AML+SML structured LB film having stress across hydrophobic/hydrophilic interface (that developed in one stroke of deposition), by down-up stroke of deposition. Release of stress also takes place in subsequent down-up stroke of deposition, which allow some molecules to flip-off from the substrate and dumped across the hydrophobic/hydrophilic interface to form large-heights ring-shaped islands. On the other hand, SML+AML/SML structure, with AML/SML as majority is expected for CdA LB film. In fact, that is what we observed initially, with slight modification, namely all molecules of SML structure do not lie in same vertical plane. Molecules close to hydrophobic/hydrophilic interface detached from the substrate and shifted upwards (B2) with respect to the rest (B1). Probably, oxide growth at the initial stages have weak hydrophilicity and can only shift SML structured molecules slightly upwards, but can not change the configuration of the molecules. With time, hydrophilicity increases and change in the configuration of molecules (from SML to AML) took place, which creates in-plane pressure. This pressure is mostly exerted on the AML/SML structured molecules close to the hydrophobic/hydrophilic interface making the molecules compact and

straighten compared to rest and showed-up as small-heights ring-shaped islands. It can be noted that unlike NiA LB film, dumping of molecules across the hydrophobic/hydrophilic interface, by flipping up from the substrate to release the stress, never occur in the CdA LB film.

It is clear from the observed structures that the LB films with Cd head-groups are more order compared to those with Ni head-groups. This can be understood considering the interaction (E) between the head-groups [54] and the bond-strength (D) between the metal ion and carboxylic ligand (CL) [50]. Interaction between the head-groups becomes stronger in presence of Cd ions rather than Ni ions (i.e. $E_{\text{Cd-Cd}} > E_{\text{Ni-Ni}}$). Strong interaction between Cd head-groups holds the adjacent molecules rigidly and makes them ordered. Also the metal ion-ligand bond-strength is stronger in the case of Cd ion compared to Ni ion (i.e. $D_{\text{Cd-CL}} > D_{\text{Ni-CL}}$) [50]. Such bond-strength difference is found to influence the patterns of the amphiphilic molecules, which lie horizontally on the HOPG substrate in the head-to-head and tail-to-tail configuration [50]. Metal ion specific bonding effect is also observed in the structure of the vertically aligned Langmuir monolayers or films [145; 224]. The difference between the structures of CdA and NiA LB films observed here clearly suggest that the bond-strength for the CdA molecules is better compared to that for the NiA molecules. Accordingly (considering both head-head interaction and metal ion-carboxylic ligand bond-strength), CdA molecules are well ordered, coupled and can not flip easily, while NiA molecules are relatively flexible and can flip.

7.4   Environment dependent growth

The polar-nonpolar nature (hydrophobic-hydrophilic) and stability of such passivated or terminated surfaces mainly H-passivated surface, which mostly used as the starting substrate for further processing for biological, energy and microelectronic applications [28], may be different in diffferent environments [225–227], depending upon the humidity of air [228–230], the amount of dissolved oxygen in water [231–233] and the presence of metal impurity [234–237] on the passivated surface, as these

can lead to the growth of oxide layer with time on the surface by desorbing the H-atom [43; 221]. It is well known that completely oxide cover or OH-terminated Si surface is hydrophilic in nature [72; 73] and is very stable. This is also very much evident from our study of NiA LB films presented earlier, namely the growth of asymmetric monolayer (AML) structure and AML/SML structure of NiA on Si by single (up) stroke and three (up-down-up) strokes of deposition, respectively, as presented again in Fig. 7.13. Now the questions are, what happens to the H-terminated Si surface, which is hydrophobic in nature, when subjected to different environments? Is it possible to transform it completely to hydrophilic, especially during nanolayer deposition and growth? Or is it possible to see the strain effect near hydrophobic/hodrophilic interface due to the partial transformation as observed for Br-terminated Si surface [238]?

Here, we have tried to find out the answers to some of these questions. For that, NiA LB films on H-passivated Si substrates are deposited in different strokes by keeping the substrates in subphase water having different pH with or without Ni metal ions and for different time. The structures of the LB films are then investigated using XRR and AFM techniques, which indicate that complete hydrophobic to hydrophilic transition of HF-treated Si substrate is indeed possible through certain pathway of environments. AFM images were collected in noncontact mode and in UHV ($\sim 10^{-9}$ mbar) conditions, after completion of XRR measurements. The mechanism behind such complete transition, essentially took place through partial transition (or oxidation) at each environment. To verify the hydrophilic or hydrophobic nature of the Si surface treated differently, contact angle measurements using home built setup were carried out. 4μl of water was placed on the treated Si surface using Hamilton syringe and the shape of the water droplet was captured by a traveling microscope followed by a digital camera. To know the chemical nature of the Si surface after treatment and after LB film deposition, XPS measurements of four different samples were performed in a multiprobe chamber (Omicron NanoTechnology) equipped with an Al Kα (E = 1486.6 eV) source and a hemispherical analyzer (EA 125).
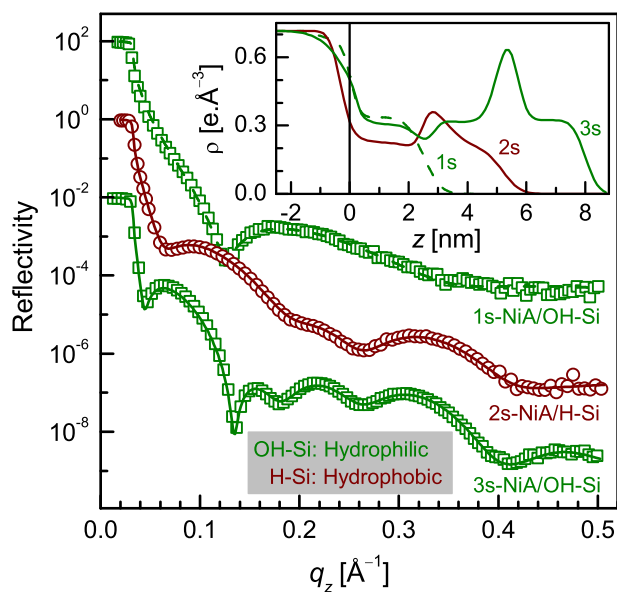
Figure 7.13: XRR data (symbol) and analyzed curves (solid line) of NiA LB films on OH-terminated Si substrates deposited by one and three strokes, and on H-terminated substrate deposited by two strokes. Insets: corresponding EDPs showing the natural hydrophilic and hydrophobic natures of the OH- and H-terminated Si substrates, respectively.

7.4.1   Results and discussion

7.4.1.1   X-ray reflectivity and electron-density profile

From XRR and EDP it is possible to estimate the structure of a film and by knowing the structure (AML or SML) just above the substrate one can predict the nature (hydrophobic or hydrophilic) of the substrate.

XRR data and analyzed curves of 1s-NiA/H-Si and 3s-NiA/H-Si samples are shown in Fig. 7.14. It can be noted that XRR profile of 1s-NiA/H-Si sample [Fig. 7.14(a)] is different from that of 1s-NiA/OH-Si sample (shown in Fig. 7.13), while XRR profile of the 3s-NiA/H-Si sample [Fig. 7.14(b)] is quite similar to that of 3s-NiA/OH-Si sample (shown in Fig. 7.13). This is also clear from the EDPs shown in the insets of Fig. 7.14. EDPs suggest that for 1s-NiA/H-Si sample, the structure is AML+SML, i.e. both AML and SML structures are present side-by-side, in nearly equal ratio, on the substrate, while for 3s-NiA/H-Si sample, the structure is AML/SML, i.e. only AML structure is present on the substrate. The AML and SML which are present in 3s-NiA/H-Si sample are quite perfect (straight and compact), while those in 1s-NiA/H-Si sample are imperfect (tilted and jumbled).

XRR data and analyzed curves of 1s-NiA/H-Si(NpH) and 3s-NiA/H-Si(NpH) samples are shown in Fig. 7.15. EDPs obtained from the analysis are shown in the insets of Fig. 7.15. Both XRR curve and EDP [see Fig. 7.15(a)] for 1s-NiA/H-Si(NpH) sample are similar to those of 1s-NiA/H-Si sample [see Fig. 7.14(a)], and so the corresponding structure. However, for the single stroke 'normal pH' sample, the coverage of SML structure is greater than that of AML structure, unlike 'high pH' one. For 3s-NiA/H-Si(NpH) sample, both XRR curve and EDP [see Fig. 7.15(b)] are quite different from those of 3s-NiA/H-Si sample [see Fig. 7.14(b)]. The structure of three strokes 'normal pH' sample is AML + AML/SML. Although, SML structure is not found on the substrate, the coverage of first layer with AML is quite low and the coverage with AML/SML structure is even lower.

Analysis of the XRR curves of 1s-NiA/H-Si(LT) and 1s-NiA/H-Si(2sNi) samples (not shown here) suggest that the structures of both films are AML+SML. Although,
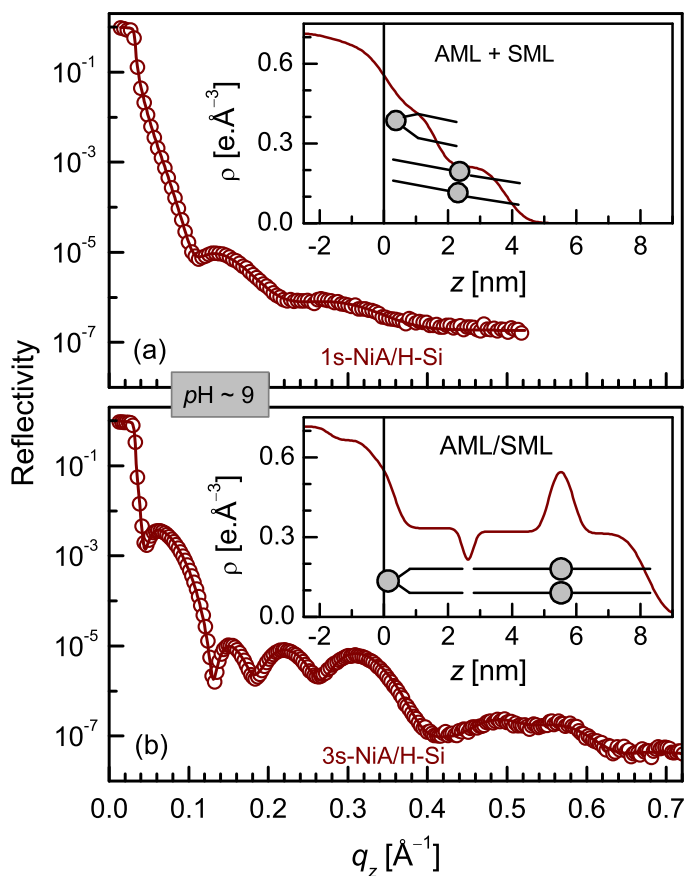
Figure 7.14: XRR data (symbol) and analyzed curve (solid line) of 'high pH' NiA LB films on H-terminated Si substrates deposited by (a) one stroke and (b) three strokes. Insets: corresponding EDPs showing the structures of the LB films.
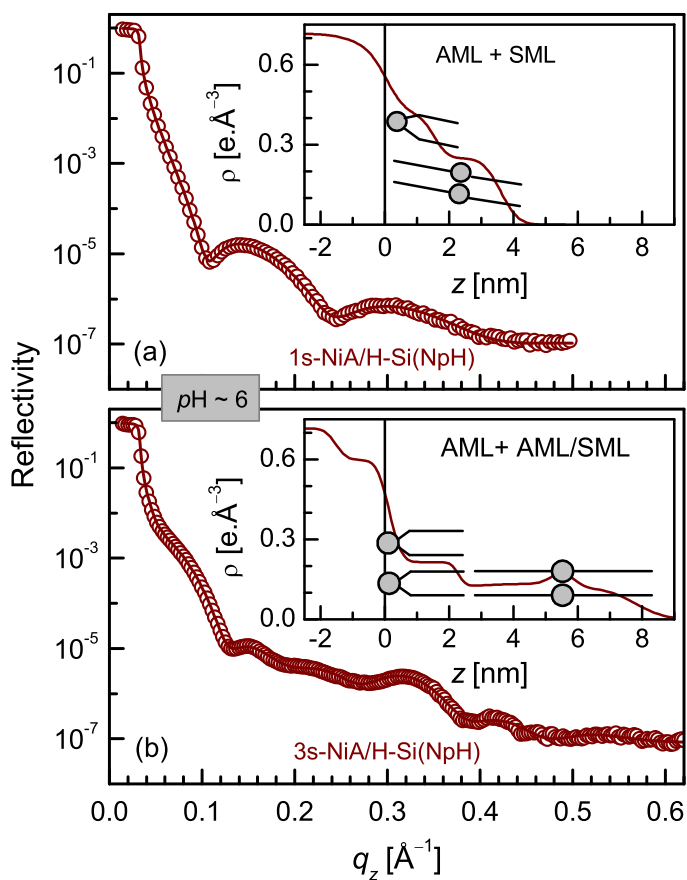
Figure 7.15: XRR data (symbol) and analyzed curve (solid line) of 'normal pH' NiA LB films on H-terminated Si substrates deposited by (a) one stroke and (b) three strokes. Insets: corresponding EDPs showing the structures of the LB films.
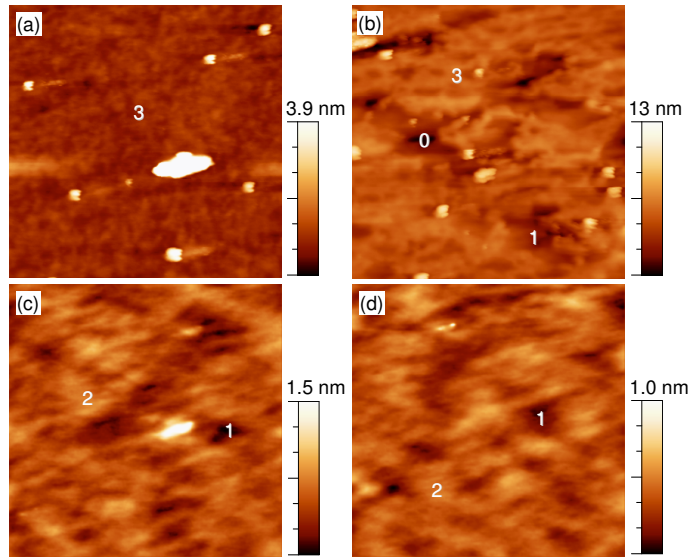
Figure 7.16: AFM images (of scan size 1×1 μm^2) showing topography of different pH NiA LB films on H-terminated Si substrates deposited by different strokes. (a) 'High pH' three strokes, (b) 'normal pH' three strokes, (c) 'high pH' one stroke and (d) 'normal pH' one stroke. Presence of layers of different heights (in unit of AML length) are indicted by the numbers.

the area corresponding to AML structure on the substrate is slightly greater than that of SML one, the surface is never completely covered with AML structure.

7.4.1.2   Atomic force microscopy and topography

Typical AFM images of four LB films are shown in Fig. 7.16. The topography of 3s-NiA/H-Si sample [Fig. 7.16)a)] is quite smooth and compact. Considering the XRR result, the height can be assigned to 3 (in unit of AML length), corresponding to the AML/SML structure. Domains of different heights, namely 0, 1 and 3 corresponding to substrate, AML and AML/SML structures are clearly visible in the AFM image of 3s-NiA/H-Si(NpH) sample [Fig. 7.16(b)], consistent with XRR result. The topography of 1s-NiA/H-Si and 1s-NiA/H-Si(NpH) samples [Fig. 7.16(c) and (d)] are quite similar. Both seems to compose of domains of two different heights and

considering the XRR results, the heights can be assigned to 1 and 2, corresponding to the AML and SML structures. The fact that the height difference between two such structures is less than 1 nm, is the imperfect nature of the films, as predicted by XRR.

7.4.1.3 Hydrophobic-hydrophilic transition pathway

Structures of the NiA LB films on HF-treated Si substrates deposited by different number of strokes and their stability obtained from XRR and AFM results, provide the hydrophobic to hydrophilic transition pathway, which is shown schematically in Fig. 7.17. SML structured NiA LB film is formed on H-terminated Si surface by two (down-up) strokes of deposition (i.e. in 2s-NiA/H-Si sample), which almost remains unchanged in air. This is a clear signature of stable hydrophobic nature of the H-terminated Si surface. On the other hand, AML+SML structured NiA LB film is formed on HF-treated Si surface by single (up) stroke of deposition (i.e. in 1s-NiA/H-Si, 1s-NiA/H-Si(NpH) and 1s-NiA/H-Si(LT) samples). This indicates partial conversion of hydrophobic surface to hydrophilic one, inside subphase water. The ratio between the coverage of AML and SML structures increases with the pH of the subphase water and with the duration for which the substrate was inside it, indicating increase in conversion with those two parameters. However, never completed with AML structure in such single stroke of deposition, unlike 1s-NiA/OH-Si sample, implying that the hydrophobic to hydrophilic transition of the HF-treated Si surface inside subphase water is always partial.

AML+AML/SML structured LB film, with partial coverage is formed on HF-treated Si surface by three (up-down-up) strokes of deposition in 'normal pH' condition (i.e. in 3s-NiA/H-Si(NpH) sample). Although, SML structure is not formed on the substrate, the hydrophilic nature of the substrate is only partial. The film formed on HF-treated Si surface by three (up-down-up) strokes of deposition in 'high pH' condition (i.e. 3s-NiA/H-Si sample), however, shows AML/SML structure similar to that of 3s-NiA/OH-Si sample. It can be noted that for the 1s-NiA/H-Si(2sNi)
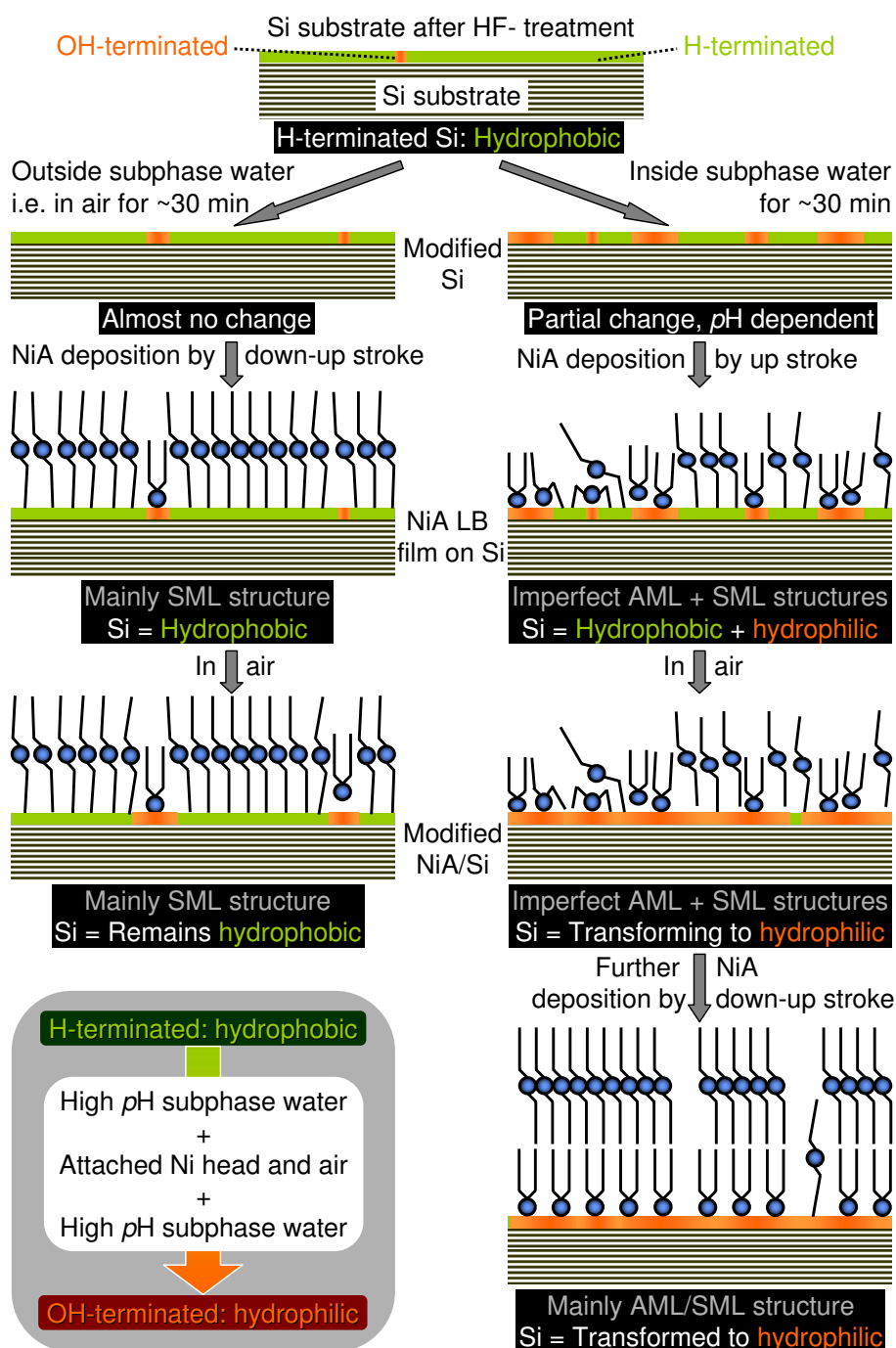
Figure 7.17: Schematics of the structures of NiA LB films on HF-treated Si substrates deposited by different number of strokes and the process involved for hydrophobic to hydrophilic transition of corresponding Si surface. SML structure on Si substrate: hydrophobic nature corresponding to H-terminated Si surface, AML or AML/SML structure on Si substrate: hydrophobic nature corresponding to OH-terminated Si surface and in between AML and SML mixed structure corresponding to H- and OH-terminated mixed Si surface.

sample, where only last up stroke is through Langmuir monolayer, the structure is neither AML/SML or complete AML. That means complete hydrophilic nature of the HF-treated Si surface is observed for the NiA LB film deposited in 'high pH' condition and in three stokes, all through Langmuir monolayer.

7.4.1.4 Hydrophobic-hydrophilic transition mechanism

H-terminated Si surface is hydrophobic in nature, while OH-terminated Si surface is hydrophilic in nature. So, in principle, the mechanism behind hydrophobic to hydrophilic transition is very simple, conversion of H-terminated surface to OH-terminated one. However, the questions are- when and how such conversion take place, i.e. what are the parameters responsible for such conversion? It is known that depending upon the sequence of deposition of LB films, substrate needs to place either inside subphase water (for odd number of stroke) or outside subphase water, i.e. in air (for even number of stroke) for about 30 min, until the pressure of Langmuir monolayer reached to a constant value of 30 mN/m to transfer. In air mainly oxygen interacts with the HF-treated surface whereas in solution apart from the dissolved oxygen many ions like OH^-, SO_4^{2-}, Ni^{2+} etc. are there which may interact with the passivated surface. Although native oxide grows on the passivated Si surface in ambient condition by desorbing the passivating element, the oxide growth rate depends on the passivating element. For H-passivated Si surface, the oxide growth rate in air is such that very little oxide or hydrophilic area could grow in 30 min. On the other hand, partial and complete hydrophilic transition of H-passivated Si surface in subphase water and in 3s-NiA/H-Si film are due to the growth of oxide on the Si surface. Since the amount of dissolved oxygen is much less in the subphase water compared to that in air, chemical reactions must take place under subphase water and there after in air for the growth of oxides on Si surface, which needs understanding.

A. Partial transition:

The possible conversion mechanism of the H-terminated Si surface to OH-terminated
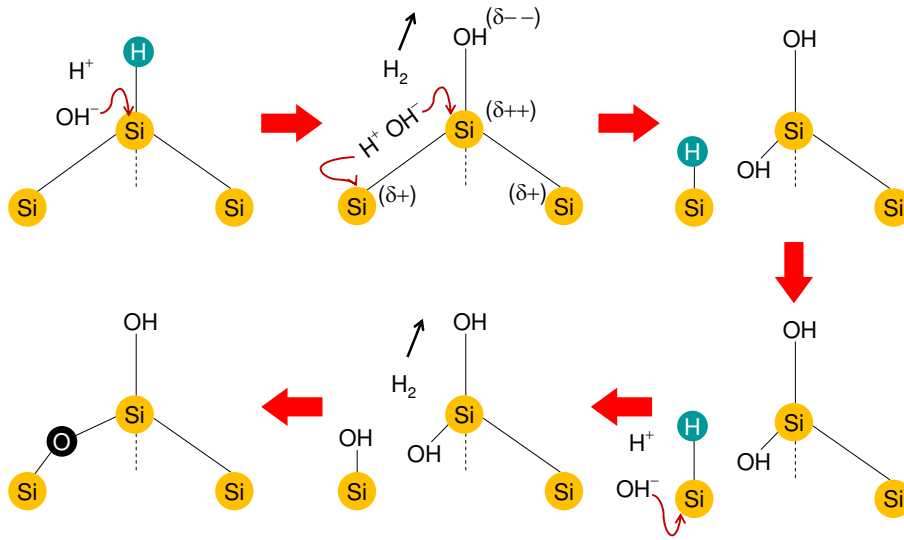
Figure 7.18: Possible conversion mechanism of Si surface under subphase water: from H-terminated to OH-terminated oxide.

one, through oxide formation, in subphase of water [72; 73; 239] is shown pictorially in Fig. 7.18. When H-terminated Si substrate is immersed into subphase water, H atoms are replaced by OH groups to form Si-OH (silanol) groups, according to the following reaction.

$$\text{Si-H} + \text{H}^+ + \text{OH}^- = \text{Si-OH} + \text{H}_2$$
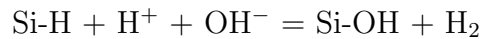
Due to the strong electronegativity of OH group, the charge induces to the Si atom bonded directly to it $(\delta++)$ is more compared to the next one $(\delta+)$. This polarization weaken the Si-SiOH back bond. In the next step, water molecules or dissolved H^+ and OH^- ions attack that back bond to form Si-H and Si-OH as given below.

$$\text{Si}^{\delta++}\text{-Si}^{\delta+} + \text{H}^+ + \text{OH}^- = \text{Si-H} + \text{Si-OH}$$

Si-H bond is further replaced by OH group to form Si-OH. When two such neighboring OH groups face each other then oxide is formed through a bridging reaction.

$$\text{Si-OH} + \text{Si-OH} = \text{Si-O-Si} + \text{H}_2\text{O}$$
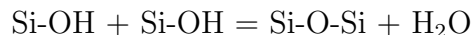
In this way, OH-terminated oxide layer is formed on the Si substrate under subphase water. It is necessary to mention that such reaction does not occur for Br-terminated Si surface, which is evident from the similar structure for two LB films (deposited either by up stroke or by down-up strokes) on Br-terminated Si surface (shown earlier in Fig. 7.4). Due to the higher electronegativity of Br atom (2.96) compared to that of H atom (2.20) [240], OH group could not replace the former one easily as they do the latter one. Even for H-terminated Si surface, such reaction rarely takes place in pure water. Presence of different ions, mainly OH^- ions in subphase water essentially helps such reaction. The coverage of OH-terminated oxide layer on the Si surface increases with the pH of the subphase water and with the duration for which the substrate was inside it, but never complete or full. Accordingly, hydrophobic to hydrophilic transition is only partial. The reason behind such partial coverage probably lies in the initial replacement of H atoms by OH groups, which is negligible inside pure water and only partial inside 'high pH' subphase water even after considerable time. However, is there exists any limiting value for such partial transition, similar to that observed for Si surface using selective surface-chemistry route [241], is not clear and needs further experimental and theoretical studies.

B. Complete transition:

Complete hydrophobic to hydrophilic transition occurs in air due to the presence of Ni head groups on partially transformed Si surface. It is known that the presence of some metals on the Si surface can create instability [242; 243] and enhance the oxidation rate of Si in air [234–237]. This is because the underlying Si-Si covalent bonds are weaken in presence of those metals (or metal ions) and accordingly associated Si atoms readily react with the ambient oxygen to form native oxide layer. In the partially transformed Si surface, AML structure is formed on hydrophilic portion and SML structure is formed on hydrophobic portion. That means Ni head groups are attached to the oxide (hydrophilic) portion of the surface and those head groups, although connected with the carboxylic ligands through ionic bonding, weaken the

nearby Si-Si covalent bonding by crossing the H-passivated layer and thereby increasing the oxide coverage in air. It can be noted that such Si-Si bond weaken may not occur through Br-passivated layer because of its large size (1.14 Å) and/or bond length with Si (2.15 Å) compared to those of H (0.37 and 1.48 Å, respectively) [240]. Since this conversion took place near the attached Ni portion, the final coverage of oxide layer depends on the amount of attached Ni and its distribution on the Si surface. This is in agreement with our results. For the 1s-Ni/H-Si(2sNi) sample, probably very few Ni^{2+} ions were physisorbed on Si surface in first up stroke, which limits the formation of OH-terminated oxide layer in air. The formation of OH-terminated oxide layer is not even complete in subsequent subphase water, which is evident from the final structure of the film (i.e. from the partial coverage with AML structure). For the films deposited in single up stroke and in two pH conditions, the number of Ni head groups attached to the Si surface and hence the formation of oxide layer in air are considerable. Among those two films, the number of Ni head groups attached to the Si surface is more for the film prepared in 'high pH' condition and correspondingly, the OH-terminated oxide layer in air is nearly complete. Although, complete hydrophilic nature of HF-treated Si surface we observed for 3s-Ni/H-Si sample, the complete transition essentially occur in air after first up stroke of deposition, as discussed. The fact that we do not observed the behavior of complete transition on the structure of the film in air because, such transition probably create little perturbation and do not reorganize the film in air. Water subphase in subsequent deposition probably helps to reorganize the film, as observed. The fact that the structure of the 1s-Ni/H-Si sample do not change completely to SML with time, because in air the change in the configuration of molecules is very difficult. Subphase water in subsequent deposition can however change the structure through reorganization (or configurational change) of NiA molecules, as observed.

C. Direct evidence:

The proposed mechanism for hydrophobic to hydrophilic transition of HF-treated
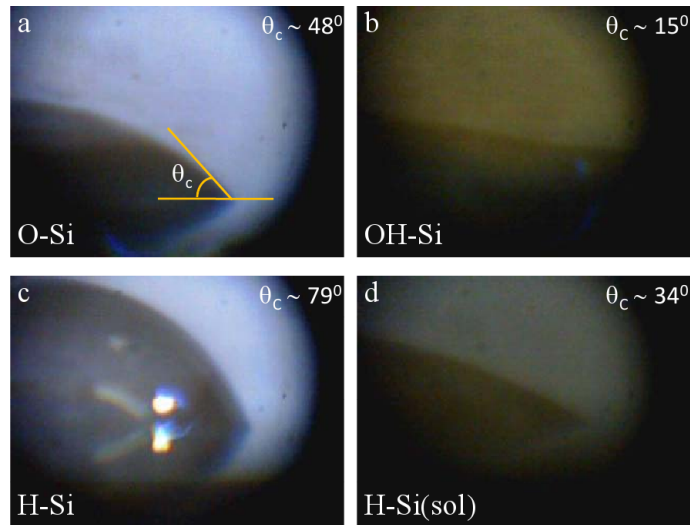
Figure 7.19: Captured images through traveling microscope followed by a digital camera of the $4\mu l$ water droplets on differently treated substrates along with the contact angle measurement indicated by the lines

surface is well supported by XPS and contact angle measurement.

1. Contact angle measurement:

Contact angle (θ_C) between water droplet and differently treated Si surfaces are shown in Fig. 7.19. The values of θ_C for HF-treated Si surface (referred as H-Si) and RCA cleaned Si surface (referred as OH-Si) are found to be 79° and 14-17°, respectively, while that for sonicated Si surface (referred as O-Si) is $\sim 48°$. These correspond to hydrophobic and hydrophilic natures of H-Si and OH-Si, respectively [156], while O-Si surface shows intermediate wetting behavior. Contact angle for H-Si substrate after keeping it inside $NiSO_4$ solution for about 40 min. [referred as H-Si(sol)] is $\sim 34°$. This suggests that the surface of H-Si(sol) becomes hydrophilic compared to H-Si substrate but less hydrophilic compared to OH-Si substrate. That means inside $NiSO_4$ solution, OH-terminated hydrophilic spots grow on H-terminated hydrophobic matrix, making overall substrate partially hydrophilic.
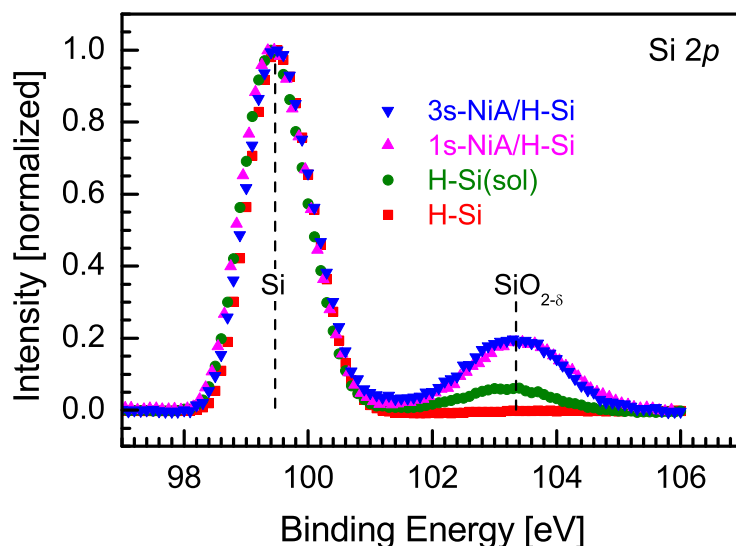
Figure 7.20: XPS spectra of four different samples in the Si $2p$ binding energy region. Two peaks appear due to substrate (Si) and surface or interfacial oxide layer ($SiO_{2-\delta}$), are indicated.

2. X-ray photoelectron spectroscopy:

The Si $2p$ core-level XPS spectra of H-Si, H-Si(sol), 1s-NiA/H-Si and 3s-NiA/H-Si samples are shown in Fig. 7.20. XPS spectra for first two samples were collected just after preparation, while those for latter two samples were collected after all x-ray measurements. The peak at ~ 99.5 eV represents Si^0 chemical state, while that at ~ 103.4 eV represents Si^{4+} chemical state, corresponding to silicon (Si) substrate and silicon oxide ($SiO_{2-\delta}$) layer, respectively [244; 245]. It is necessary to mention that the spectra in Fig. 7.20 are presented after normalizing each spectrum with its Si^0 peak intensity. Presence of silicon oxide in the H-Si sample is not observed, while that in other three samples is clearly evident. This indicates that the surface of H-Si sample is well passivated with H atoms and is stable in air, at least for the time, before it transfer into the UHV chamber. It can be noted that for the 2s-NiA/H-Si sample, this was the substrate condition when deposition of NiA molecules starts and complete hydrophobic nature of such is quite natural. The oxide signal for

185

1s-NiA/H-Si and 3s-NiA/H-Si samples are quite strong and nearly similar, while that for H-Si(sol) is relatively weak. Latter indicates that the oxide growth on the surface of H-Si(sol) sample is only partial. This was the substrate condition for the 1s-NiA/H-Si sample when deposition starts and partial hydrophilic and hydrophobic natures of such substrate is well expected. XPS spectrum of 1s-NiA/H-Si sample clearly shows that further oxide really grows at the film-substrate interface of such sample with time in air and is nearly complete (comparing with the XPS spectrum of 1s-NiA/H-Si sample) as proposed, although not much structural change is observed.

7.5 Conclusions

Structure and stability of LB films of NiA and CdA on differently passivated Si surfaces were studied using XRR and AFM techniques. Hydrophilic, hydrophobic and coexisting natures of the OH-, H- and Br-passivated Si surfaces, respectively, are clearly evident from the structures of the both LB films. The quality of these two LB films (on OH- and H-passivated Si surfaces) along with the structure (on Br-passivated Si surface) are very different on such passivated surfaces. The order of the Cd head-groups in the SML structure, formed directly on hydrophobic Si surface or through AML structure on hydrophilic Si surface, are found far better compared to that of the Ni head-groups. This clearly suggests that $E_{\text{Cd-Cd}} > E_{\text{Ni-Ni}}$, i.e. the interaction between Cd head-groups is stronger compared to that between Ni head-groups and/or $D_{\text{Cd-CL}} > D_{\text{Ni-CL}}$, i.e. the bond-strength between Cd ion and carboxylic ligand is better compared to that between Ni ion and carboxylic ligand. Influence of such effects is also observed for the LB films on the Br-terminated Si surface. For example CdA molecules show that they are coupled and can not flip easily, while NiA molecules show that they are flexible and can flip easily either from hydrophilic to nearby hydrophobic portion of Si surface during single stroke of deposition or from the substrate and dumping of molecules across the hydrophobic/hydrophilic interface to release the stress in the structure of the film during three strokes of deposition. Ring-shaped islands are observed in both LB film across the

hydrophobic/hydrophilic interface. They are quite regular but small in heights in CdA LB film compared to that in NiA LB film. There is a difference in their origin for two different LB films.

HF-treated Si surface, which is hydrophobic in nature and quite stable in air, transformed partially or completely to hydrophilic surface, inside subphase water or during NiA LB film growth by up-down-up strokes of deposition and in 'high pH' condition. This transition essentially takes place by conversion of H-terminated Si surface to OH-terminated one, through oxide formation. Although the amount of oxygen inside subphase water is less compared to that in air, the oxide formation inside subphase water is more, which takes place by chemical reaction in presence of highly electronegative OH^- ions. As the pH of the subphase water increases, the amount of OH^- ions increases and so the amount of oxide coverage. Also, as the duration for which the substrate was inside subphase water increases, the chances of chemical reaction increases and so the amount of oxide coverage, but never complete or full. The attachment of Ni head groups on the oxide portion of the partially transformed Si substrate by deposition of LB film, essentially weaken the nearby Si-Si bonding, which then readily react with oxygen to form oxides. Depending upon the amount of attached Ni head groups and its distribution on the Si surface, it is possible to have complete oxide coverage through such reaction in air. The signature of which is only visible in subsequent deposition, where reorganize of molecules are possible.

Chapter 8

Conclusions and outlook

8.1 Summary and concluding remarks

The main results of our studies are summarized first and then attempt have been made to draw some general conclusions connecting these results.

8.1.1 Summary

Broadly, the research work that has been reported in this thesis can be classified as follows:

1. Au/X-Si [X = O, H, Br]
The diffusion of Au into Si substrate strongly depends on the passivating elements like O, H, Br and also on the crystalline orientation of the Si substrate like Si(001), Si(111) at room temperature. Large diffusion of Au into Si(001) substrate when surface is pretreated with HF and, subsequently, large variation in the topography. While Au deposited on Si(001) surface further pretreated with Br shows small diffusion, that on untreated Si surface shows negligible diffusion with relatively smooth topography. The evolution of the Au-Si(001) interdiffused layer with time has been attributed to the diffusion of Au through unblocked Si surface. The unblocked area

through which diffusion takes place decreases exponentially with time. The growth of the blocking layer is related to the surface stability due to surface passivation. The nature of the diffusion in Au-Si(111) system is similar to that of the Au-Si(001) system. Though they are qualitatively similar but there is large quantitative differences. The diffused amount of Au into Si is greater in each passivation for Si(001) surface compared to Si(111) surface and the growth-time of oxide i.e. (τ) value is one order greater in case of Br-passivated Si(111) surface compared to Si(001) which indicates Br-passivated Si(111) is more stable compared to Br-passivated Si(001). The size, electronegativity, bond-energy etc. of the passivating materials and the number of dangling bonds on the Si surface determined the stability or instability of the Si surface. This instability, parameterized by growth-time alone, can control the amount of diffusion, apart from the openness of the Si surface structure.

The diffusion of Au into Si, which is only observed in ambient condition and not in UHV, is a clear signature of atmospheric pressure induced atomic diffusion into solid crystal and provides unique concept of inherent-pressure inside a crystal structure. It also provides a characteristic length scale, which is a measure of quantitative extent of pressure gradient, from the surface to the bulk of that solid crystal. The atomic diffusion observed here is more like a fluid flow, where relative pressure acts as a regulating valve, which not only controls the speed but also controls the direction of the flow. Apart from the pressure-gradient, such diffusion depends on the crystal structure and freeness of the diffusing atoms. The analysis suggests that the freeness of the diffusing atoms increases with decreasing thickness and/or coverage of Au layer. We claim that by changing the surface passivation, stability of the surface can be changed, which then can be used to control the layer of interdiffusion in nanometer length scale. Moreover the position of the diffused Au layer into Si can be tuned by varying the pressure acting on the Au film.

2. Ag/X-Si [X = O, H, Br]

No interdiffusion of Ag into Si, like Au, has been observed, rather the Ag/Si interface is found very sharp. Here, dewetting with time of Ag nanolayer has been observed at

ambient condition. However, the grown structure of Ag nanolayers and its stability are very much dependent on the passivations of Si(001) substrates. The SK (layer-plus-island)-like growth mode of Ag nanolayers have been observed initially, which is more towards FM (layer-by-layer)-like growth mode on H-passivated Si(001) surface, while that on Br-passivated Si(001) surface is more towards VW (island)-like growth mode as observed on native oxide covered Si(001) surface. Such initial growth modes remain almost unchanged in UHV conditions, while at ambient conditions strong evolution of growth has been observed. Dewetted 3D-island-like structures evolved due to the oxide growth at the interface. On the Br-passivated Si(001) surface, fast growth of large number of small size 3D structures having no preferential crystallographic direction have been observed, while on the H-passivated Si(001) surface, slow growth of small number of large size well faceted 3D epitaxial [Ag(001)/Si(001)] structures have been observed. Such transition from relatively wetted to dewetted structures of Ag nanolayer having epitaxy or not, along with initial growth can be understood considering interfacial energies as $\gamma_{Ag/H\text{-}Si} \ll \gamma_{Ag/Br\text{-}Si} < \gamma_{Ag/O\text{-}Si}$. Surface free energy, surface mobility and surface instability of the passivated surfaces govern and control the growth and evolution of such interesting structures of silver on silicon.

3. Cu/X-Si [X = O, H, Br]

Co-existance of dewetting and interdiffusion has been observed in Cu nanolayer deposited on differently passivated Si(001) surfaces. Though initial compactness and smoothness of Cu nanolayer on the H-passivated and Br-passivated Si(001) surfaces are nearly same, the amount of dewetting and interdiffusion strongly depend on surface treatments. Diffusion of Cu into H-passivated Si surface is greater than Br-passivated surace whereas dewetting is dominant in Br-passivated Si surface rather than H-passivated surface. The growth of dewetted 3D-island-like structures (Volmer-Weber-like mode) from comparatively wetted Cu nanolayer (Stranski-Krastanov-like mode) and moreover initially diffused nanolayer of Cu is propagating through Si are evident in both cases. Such evolution of growth is through dewetting

(related to the change in the interfacial energy due to the oxide-growth), migration and coalesce of Cu, which can even produce 3D-islands on both passivated surface and also interdiffusion through native oxide free areas results in a very thin diffused nanolayer of Cu into Si. The growth-rate, size, number-density of 3D-islands and thickness, composition of diffused nanolayer strongly depend on different types of passivations. These differences can be realized considering the growth-time of oxide (i.e. instability of passivated surface) which not only blocks the interdiffusion to give a control in the thickness as well as density but also enhances the dewetting, in-plane inhomogeneity of interfacial energy (i.e. inhomogeneous nature of passivation) and in-plane diffusion of Cu on the passivated surfaces.

4. LB/X-Si [LB = NiA, CdA and X = OH, H, Br]

Hydrophilic, hydrophobic and coexisting natures of the OH-, H- and Br-passivated Si surfaces, respectively, are clearly evident from the structures of the NiA and CdA LB films. The quality or order (on OH- and H-passivated Si surfaces) along with the structure (on Br-passivated Si surface) of LB films are very different for different headgroup. The order of the Cd head-groups in the SML structure, formed directly on hydrophobic Si surface or through AML structure on hydrophilic Si surface, are found far better compared to that of the Ni head-groups. This clearly suggests that $E_{\text{Cd-Cd}} > E_{\text{Ni-Ni}}$, i.e. the interaction between Cd head-groups is stronger compared to that between Ni head-groups and/or $D_{\text{Cd-CL}} > D_{\text{Ni-CL}}$, i.e. the bond-strength between Cd ion and carboxylic ligand is better compared to that between Ni ion and carboxylic ligand. Influence of such effects is also observed for the LB films on the Br-terminated Si surface. For example CdA molecules show that they are coupled and can not flip easily, while NiA molecules show that they are flexible and can flip easily either from hydrophilic to nearby hydrophobic portion of Si surface during single stroke of deposition or from the substrate and dumping of molecules across the hydrophobic/hydrophilic interface to release the stress in the structure of the film during three strokes of deposition. Accordingly, ring-shaped islands are formed on both LB films across the hydrophobic/hydrophilic interface. However,

they are quite regular but small in heights in CdA LB film compared to that in NiA LB film. Formation of first one is more like 'buckling' associated with coupled or restricted motion of Cd headgroups, while that of the latter one is more like 'collapse' associated with flexible or easy motion of Ni headgroups.

HF-treated Si surface, which is hydrophobic in nature and quite stable in air, transformed partially or completely to hydrophilic surface, inside subphase water or during NiA LB film growth by up-down-up strokes of deposition and in 'high pH' condition. This transition essentially takes place by conversion of H-terminated Si surface to OH-terminated one, through oxide formation. Although the amount of oxygen inside subphase water is less compared to that in air, the oxide formation inside subphase water is more, which takes place by chemical reaction in presence of highly electronegative OH^- ions. As the pH of the subphase water increases, the amount of OH^- ions increases and so the amount of oxide coverage. Also, as the duration for which the substrate was inside subphase water increases, the chances of chemical reaction increases and so the amount of oxide coverage, but never complete or full. The attachment of Ni head groups on the oxide portion of the partially transformed Si substrate by deposition of LB film, essentially weaken the nearby Si-Si bonding, which then readily react with oxygen to form oxides. Depending upon the amount of attached Ni head groups and its distribution on the Si surface, it is possible to have complete oxide coverage through such reaction in air. The signature of which is only visible in subsequent deposition, where reorganize of molecules are possible.

8.1.2 General conclusions

Si surface passivated or terminated differently, shows interesting behavior towards nanolayer.

- When nanolayer is made of Au, which reacts easily with Si, then openness and blocking (due to growth of native oxide layer) natures of passivated Si surfaces control the interdiffusion. Formation and movement of interdiffused nanolayer at room

temperature are observed, which is a clear signature of atmospheric pressure induced atomic diffusion into solid crystal and provides unique concept of inherent pressure inside a crystal structure. Such diffusion also depends on the crystal structure and freeness of the diffusing atoms.

- When nanolayer is made of Ag, which forms sharp interface with Si, then surface free energy, surface mobility, and surface instability of the passivated Si surfaces govern and control the growth and evolution of wetted-dewetted structures of Ag on Si with or without epitaxy.

- When nanolayer is made of Cu, then the passivated Si surface and its dynamics control both the interdiffusion and the wetting-dewetting behavior.

- When nanolayer is made of metal-organic molecules, which have hydrophilic headgroups and hydrophobic tails, then hydrophilic, hydrophobic or coexisting nature of the terminated Si surfaces control the structure of the Langmuir-Blodgett films. Presence of both hydrophilic and hydrophobic regions on Br-passivated Si surface, which is associated with the inhomogeneity and instability, create interesting nanostructures to release interfacial stress through 'buckling' or 'collapse' of molecules containing Cd or Ni headgroups, respectively. The hydrophilic-hydrophobic (polar-nonpolar) nature of the unknown surface in molecular level or transition of nature of surface (say from hydrophobic to hydrophilic) is possible to find out by knowing the structure of LB film on it.

8.2   Scope for further studies

In many ways the experiments carried out in this dissertation have generated as many questions as answers. There are a number of important avenues for future research. Some key opportunities are summarized below.

In chapter 4 and 6 we have observed Gaussian-shape diffused nanolayers of Au and Cu into Si substrates. The shape is quite interesting from the fundamental point of view. Reason behind the formation of such diffused layer from the initial stage

of deposition is not well understood. Also its movement in presence of atmospheric pressure not in UHV open-up a fundamental question about the concept of inherent pressure inside the crystal structure. What is the exact mechanism of the movement of diffused layer inside the crystal structure ? To answer such fundamental questions the detailed theoretical understanding is necessary.

We believe that the transport properties of such controlled diffused nanolayer will be interesting due to the confinement effects. At the same time it will be complicated due to the presence of different layers. One of our aim is to separate out the effect of different layers. For that we are planning to carry out the electrical transport measurements (conventionally two or four probe as well as by scanning tunneling spectroscopy) of the system in different combination (by varying Au concentration into Si and by pressure). Above study can be continued for any other diffusive metal-semiconductor systems (like Cu/Si, Pt/Si etc.) which are under interest.

The wet chemical passivation technique can be used to form desired structure of soft materials like LB film of amphiphilic molecules and nanoparticles on the substrate surface by using photoresist as a musk. Also this technique can be useful to study the transport properties of such materials. In order to transport study by STS specially on nanoparticles which is usually covered by a hydrophobic layer it is essential to minimize the transport barrier to facilitate the electron tunneling. Prior to deposition such molecules on the substrate, the substrate surface should be make hydrophobic. We have discussed in chapter 7 that the wet chemical passivation technique can be used to make a surface hydrophobic and accordingly there is a possibility to replace the previous technique i.e. a deposition of OTS layer (which has a minimum thickness of 2 nm) on the substrate surface. In case of wet chemically passivated surface there is a one foreign atomic layer between the soft material and the substrate. This facilitates the electron tunneling across the sample in order to get good STM or STS results.

References

[1] P. Buffat and J. P. Borel, Phys. Rev. A **13**, 2287 (1976). 1

[2] I. P. Batra, S. Ciraci, G. P. Srivastava, J. S. Nelson, and C. Y. Fong, Phys. Rev. B **34**, 8246 (1986). 1

[3] R. Lazzari and J. Jupille, Surf. Sci. **482**, 823 (2001). 2

[4] T. J. Yen et al., Science **303**, 1494 (2004). 2

[5] J. O. Dimmock, Opt. Express **11**, 2397 (2003). 2

[6] M. Copel, M. C. Reuter, E. Kaxiras, and R. M. Tromp, Phys. Rev. Lett. **63**, 632 (1989). 2, 5, 31, 117

[7] K. Sumitomo, T. Kobayashi, F. Shoji, K. Oura, and I. Katayama, Phys. Rev. Lett. **66**, 1193 (1991). 2, 31, 118

[8] W. M. Bullis, Solid State Electron. **9**, 143 (1966). 3

[9] G. G. Roberts, Adv. Phys. **34**, 475 (1985). 3, 4, 34, 145

[10] I. R. Peterson, J. Phys. D **23**, 379 (1990). 4

[11] L. A. Feigin, R. L. Kayushina, T. B. Dubrovsky, and V. V. Erokhin, Prog. Colloid. Polym. Sci. **93**, 276 (1993).

[12] K. Tollner, R. Popovitz-Biro, M. Lahav, and D. Milstein, Science **278**, 2100 (1997).

[13] C. P. Collier, R. J. Saykally, J. J. Shiang, S. E. Henrichs, and J. R. Heath, Science **277**, 1978 (1997).

[14] R. Singhal, A. Chaubey, K. Kaneto, W. Takashima, and B. D. Malhotra, Biotechnol. Bioeng. **85**, 277 (2004).

[15] S. N. Sawant et al., J. Phys. Chem. B **110**, 24530 (2006).

[16] K. Hosoki, T. Tayagaki, S. Yamamoto, K. Matsuda, and Y. Kanemitsu, Phys. Rev. Lett. **100**, 207404 (2008). 3, 34, 145

[17] R. H. Tredgold, A. J. Vickers, and R. A. Allen, J. Phys. D **17**, L5 (1984). 3

[18] J. D. Swallen, Langmuir **3**, 932 (1987). 3

[19] D. R. Nelson and B. I. Halperin, Phys. Rev. B **21**, 5312 (1980). 3

[20] S. A. Darst, H. O. Ribi, D. W. Pierce, and R. D. Kornberg, J. Molec. Biol **203**, 269 (1988). 3

[21] G. G. Roberts, *Langmuir-Blodgett Films*, Plenum, New York, 1990. 4

[22] E. H. Nicollian and A. Goetzberger, Bell Syst. Tech. J. **46**, 1055 (1967). 4

[23] M. A. Green, Appl. Phys. Lett. **33**, 178 (1978).

[24] E. Yablonovitch, R. M. Swanson, W. D. Eades, and B. R. Weinberger, Appl. Phys. Lett. **48**, 245 (1986). 4

[25] E. Yablonovitch, D. L. Allara, C. C. Chang, T. Gmitter, and T. B. Bright, Phys. Rev. Lett. **57**, 249 (1986). 4

[26] U. Mohideen, W. S. Hobson, S. J. Pearton, F. Ren, and R. E. Slusher, Appl. Phys. Lett. **64**, 1911 (1994). 4

[27] K. Nakamura, S. Ichimura, and H. Shimizu, Appl. Surf. Sci. **100/101**, 444 (1996). 4

[28] R. Boukherroub, Curr. Opin. Solid State Mater. Sci. **9**, 66 (2005). 4, 171

[29] K. Sekar, P. V. Satyam, G. Kuri, D. P. Mahapatra, and B. N. Dev, Nucl. Instrum. Methods Phys. Res. B **73**, 63 (1993). 4, 5, 14, 32, 79, 98

[30] C. H. Lee et al., Phys. Rev. B **62**, 17134 (2000). 4, 79, 98

[31] N. Benouattas, A. Mosser, and A. Bouabellou, Appl. Surf. Sci. **252**, 7572 (2006). 5, 14, 134

[32] W. R. Wilcox and T. J. LaChapelle, J. Appl. Phys. **35**, 240 (1964). 5, 78

[33] A. Rodriguez, H. Bracht, and I. Yonenaga, J. Appl. Phys. **95**, 7841 (2004). 78

[34] T. Nakahara, S. Ohkura, F. Sholi, T. Hanawa, and K. Oura, Nucl. Instrum. Methods B **45**, 467 (1990). 5

[35] T. Nakahara, S. Ohkura, F. Sholi, T. Hanawa, and K. Oura, J. Appl. Phys. **85**, 7135 (1999). 5, 6

[36] K. Fukutani, H. Iwai, Y. Murata, and H. Yamashita, Phys. Rev. B **59**, 13020 (1999). 5, 32, 118

[37] J. D. Struthers, J. Appl. Phys. **27**, 1560 (1956). 5, 30

[38] J. D. Struthers, J. Appl. Phys. **28**, 516 (1957). 5, 30

[39] J. F. Watts and J. Wolstenholme, *An Introduction to Surface Analysis by XPS and AES*, Wiley. 6

[40] G. P. Carey et al., Journal of Vacuum Science and Technology A **3**, 255 (1985). 6

[41] J. Daillant and A. Gibaud, *X-ray and Neutron Reflectivity: Principles and Applications*, Springer, Paris, 1999. 6, 53, 58

[42] M. Tolan, *X-ray Scattering from Soft-Matter Thin Films*, Springer, Berlin, 1999. 6

[43] J. K. Bal and S. Hazra, Phys. Rev. B **75**, 205411 (2007). 6, 29, 104, 119, 127, 131, 150, 156, 159, 172

[44] G. Kuri, M. Gupta, R. Schelldorfer, and D. Gavillet, Appl. Surf. Sci. **253**, 1071 (2006). 6

[45] N. Suresh, R. Thakur, D. Phase, and S. Chaudhari, Vacuum **72**, 419 (2004).

[46] M. Delheusy et al., Appl. Phys. Lett. **92**, 101911 (2008). 6

[47] D. Y. Takamoto et al., Science **293**, 1292 (2001). 7, 34, 146

[48] S. Kundu, A. Datta, and S. Hazra, Chem. Phys. Lett. **405**, 282 (2005). 7, 34, 146, 154

[49] D. K. Schwartz, Surf. Sci. Rep. **27**, 245 (1997). 7, 34, 35, 145, 146, 154

[50] W. Dong, R. Wang, G. Mao, and H. Möhwald, Soft Matter **2**, 686 (2006). 7, 160, 171

[51] S. Hazra, A. Gibaud, A. Desert, V. Gacem, and N. Cowlam, Physica B **283**, 45 (2000). 7, 34, 35, 145, 146

[52] Y. Zhang, Z. Tun, and A. M. Ritcey, Langmuir **20**, 6187 (2004). 7, 35

[53] M. K. Mukhopadhyay, M. K. Sanyal, A. Datta, J. Webster, and J. Penfold, Chem. Phys. Lett. **407**, 276 (2005). 7, 35, 146

[54] D. K. Schwartz, J. Garnaes, R. Viswanathan, and J. A. Zasadzinski, Science **257**, 508 (1992). 7, 35, 160, 171

[55] A. L. Barabási and H. E. Stanley, *Fractal Concepts in Surface Growth*, Cambridge University Press, Cambridge, 1995. 13, 92, 95, 97

[56] R. J. Archer, J. Electrochem. Soc. **104**, 619 (1957). 13

[57] F. Lukes, Surf. Sci. **30**, 91 (1972).

[58] S. I. Raider, R. Fitsch, and M. J. Palmer, J. Electrochem. Soc. **112**, 413 (1975). 15

[59] H. R. Philip and E. A. Taft, J. Appl. Phys. **53**, 5224 (1982).

[60] E. A. Taft, J. Electrochem. Soc. **135**, 1022 (1988).

[61] T. Hattori et al., Jpn. J. Appl. Phys. **28**, L296 (1989). 13

[62] D. Graf, M. Grundner, and R. Shulz, J. Appl. Phys. **68**, 5155 (1990). 15

[63] D. Graf, M. Grundner, D. Muhlhoff, and M. Dellith, J. Appl. Phys. **69**, 7620 (1991). 15

[64] M. Morita, T. Ohmi, E. Hasegawa, M. Kawakami, and K. Suma, Appl. Phys. Lett. **55**, 562 (1989). 15, 16

[65] M. J. Bedzyk, W. Gibson, and J. A. Golovchenko, J. Vac. Sci. Technol **20**, 634 (1982). 16, 22

[66] K. Sekar, G. Kuri, D. P. Mahapatra, and B. N. Dev, Surf. Sci. **302**, 25 (1994). 16

[67] D. J. Monk, D. S. Soane, and R. T. Howe, J. Electrochem. Soc. **140**, 2339 (1993). 17

[68] K. Osseo-Asare, J. Electrochem. Soc. **143**, 1339 (1996). 17

[69] Periodic Table of Elements, *http* : *//www.dayah.com/periodic* . 20, 21, 100

[70] Wired Chemist, *http* : *//www.wiredchemist.com* . 20, 21, 100

[71] G. W. Trucks, K. Raghavachari, G. S. Higashi, and Y. J. Chabal, Phys. Rev. Lett. **65**, 504 (1990). 21, 79, 98

[72] H. F. Okorn-Schmidt, IBM J. Res. Develop. **43**, 351 (1999). 21, 35, 146, 172, 181

[73] X. G. Zhang, *Electrochemistry of Silicon and Its Oxide*, Kluwer Academic Publishers, New York, 2004. 21, 35, 146, 172, 181

[74] K. Sekar, P. V. Satyarn, G. Kuri, D. Mahapatra, and B. Dev, Nucl. Instrum. Methods B **71**, 308 (1992). 22

[75] J. F. Chang, T. F. Young, Y. L. Yang, H. Y. Ueng, and T. C. Chang, Mater. Chem. Phys. **83**, 199 (2004). 22, 79

[76] R. Walser and R. Bene, Appl. Phys. Lett. **28**, 624 (1976). 23, 32

[77] K. N. Tu, Appl. Phys. Lett. **27**, 221 (1975). 24

[78] A. Hiraki, Surf. Sci. Rep. **3**, 357 (1984). 24

[79] L. Braicovich et al., Phys. Rev. B **20**, 5131 (1979). 24, 29, 30

[80] A. Hiraki, J. Electrochem. Soc. **27**, 2662 (1980). 24

[81] M. del Giudice, J. J. Joyce, and J. H. Weaver, Phys. Rev. B **36**, 4761 (1987). 25

[82] B. Lamontagne, E. Sacher, and M. R. Wertheimer, Appl. Surf. Sci. **78**, 399 (1994). 25

[83] H. J. Grey and A. Isaacs, *Dictionary of Physics*, 3rd ed., Longman, Singapore, 1991. 26

[84] A. Einstein, Annalen der Physik **17**, 549 (1905). 26

[85] A. Einstein, Annalen der Physik **19**, 371 (1906). 26

[86] U. Gösele, W. Frank, and A. Seeger, Appl. Phys. **23**, 36 (1980). 27

[87] F. C. Frank and D. Turnbull, Phys. Rev. **104**, 617 (1956). 27

[88] P. G. Shewmon, *Diffusion in Solids*, J. Williams Book company, Jenks Oklahoma, 1983. 28

[89] S. K. Ghandhi, *The Theory and Practice of Microelectronics*, John Wiley, New York, 1968. 29

[90] C. B. Collins, R. O. Carlson, and C. J. Gallagher, Phys. Rev. **105**, 1168 (1957). 29, 30, 78

[91] G. L. Lay, Surf. Sci. **132**, 169 (1983). 30

[92] A. Hiraki, Surf. Sci. Rep. **3**, 357 (1983). 30, 110

[93] S. L. Molodtsov, C. Laubschat, G. Kaindl, A. M. Shikin, and V. K. Adamchuk, Phys. Rev. B **44**, 8850 (1991). 30

[94] A. Cros and P. Muret, Mater. Sci. Rep. **8**, 271 (1992). 29, 30, 78, 110, 127

[95] L. Ma, J. Wang, Q. Lu, and G. Wang, Chem. Phys. Lett. **405**, 208 (2005). 29, 31, 118

[96] J.-J. Yeh et al., Phys. Rev. Lett. **70**, 3768 (1993).

[97] K. Pedersen and P. Morgen, J. Phys.: Condens. Matter **9**, 9497 (1997).

[98] C. Grupp and A. Taleb-Ibrahimi, Phys. Rev. B **57**, 6258 (1998).

[99] J. H. Kim, G. Yang, S. Yang, and A. H. Weiss, Surf. Sci. **475**, 37 (2001). 79

[100] Y. Haruyama, K. Kanda, and S. Matsui, Radiat. Phys. Chem. **75**, 1943 (2006). 29, 30

[101] T. Ishida, Y. Nakajima, J. Endo, D. Collard, and H. Fujita, Nanotechnology **20**, 065705 (2009). 30

[102] B. L. Sharma, *Diffusion in Semiconductors*, Trans. Tech. Pub., Germnay, 1970. 30

[103] I. Daruka and A.-L. Barabási, Phys. Rev. Lett. **79**, 3708 (1997). 31, 117

[104] V. A. Shchukin and D. Bimberg, Rev. Mod. Phys. **71**, 1125 (1999). 31, 117, 118, 130

[105] L. Huang, S. J. Chey, and J. H. Weaver, Phys. Rev. Lett. **80**, 4095 (1998). 31, 118, 119

[106] T. Muller and H. Nienhaus, J. Appl. Phys. **93**, 924 (2003). 118

[107] B. Sundaravel, A. K. Das, S. K. Ghose, K. Sekar, and B. N. Dev, Appl. Surf. Sci. **137**, 12 (1999).

[108] V. Derycke et al., Nature Materials **2**, 253 (2003).

[109] A. Nishiyama et al., Surf. Sci. **350**, 229 (1996).

[110] T. Yasue and T. Koshikawa, Surf. Sci. **377-379**, 923 (1997).

[111] W. Widdra, S. I. Yi, R. Maboudian, G. A. D. Briggs, and W. H. Weinberg, Phys. Rev. Lett. **74**, 2074 (1995). 31, 118

[112] F. K. LeGoues, M. Liehr, M. Renier, and W. Krakow, Phil. Mag. B **57**, 179 (1988). 31, 118

[113] G. A. Smith, K. H. Park, G. C. Wang, T. M. Lu, and W. M. Gibson, Surf. Sci. **233**, 115 (1990).

[114] D. C. McKenna, G. C. Wang, and K. Rajan, J. Electron. Mater. **20**, 753 (1991).

[115] T. C. Nason, L. You, and T. M. Lu, J. Appl. Phys. **2**, 466 (1992).

[116] K. Takahiro, S. Nagata, and S. Yamaguchi, Appl. Phys. Lett. **69**, 2828 (1996). 31, 118

[117] S. Tanaka, T. Abe, and T. Yamashina, Chem. Lett. **6**, 599 (1974). 31, 118, 127

[118] N. Marechal, E. Quensnel, and Y. Panleau, J. Vac. Sci. Technol. A **12**, 707 (1994). 31, 118, 127

[119] J. H. Je, T. S. Kang, and D. Y. Noh, J. Appl. Phys. **81**, 6716 (1997). 31, 118

[120] T.-B. Hur, H. K. Kim, and J. Blachere, Phys. Rev. B **75**, 205306 (2007). 31, 118

[121] R. Naik, C. Kota, B. U. M. Rao, and G. W. Auner, J. Vac. Sci. Technol. A **12**, 1832 (1994). 32, 118

[122] X. B. Zhang et al., Surf. Sci. **340**, 317 (1995).

[123] K. Oura, V. G. Lifshits, A. A. Saranin, A. V. Zotov, and M. Katayama, Surf. Sci. Rep. **35**, 1 (1999).

[124] I. Matsuda et al., Phys. Rev. B **63**, 125325 (2001).

[125] T. Fujino, T. Okuno, M. Katayana, and K. Oura, Jpn. J. Appl. Phys. **40**, L1173 (2001).

[126] A. Arranz et al., Phys. Rev. B **65**, 075405 (2002). 32, 118

[127] L. Soltz and F. M. D'Heurle, Thin Solid Films **189**, 269 (1990). 32

[128] C. A. Chang, J. Appl. Phys. **67(1)**, 566 (1990). 32

[129] C. A. Chang and C. K. Hu, Appl. Phys. Lett. **57(6)**, 617 (1990). 32

[130] A. A. Istratov and E. R. Weber, J. Electrochem. Soc. **149**, G21 (2002). 32, 133

[131] J. M. Poate, K. N. Tu, and J. W. Mayer, *Thin Films Interdiffusion and Reactions*, Wiley, New York, 1978. 32

[132] W. Frank, W. Gosele, H. Mehrer, and A. Seeger, *Diffusion in Crystalline Solids*, Academic Press, New York, 1984. 32, 78

[133] T. Y. Tan and U. Gösele, Appl. Phys. A **31**, 1 (1985). 32

[134] M. Grundner and H. Jacob, Appl. Phys. A **39**, 73 (1986). 32

[135] N. Benouattas, A. Mosser, D. Raiser, J. Faerber, and A. Bouabellou, Appl. Surf. Sci. **153**, 79 (2000). 32, 134

[136] M. C. Petty, *Langmuir-Blodgett Films: An Introduction*, Cambridge University Press, New York, 1996. 33, 145

[137] H. D. Sikes and D. K. Schwartz, Science **278**, 1604 (1997).

[138] E. Hatta, T. Maekawa, K. Mukasa, and Y. Shimoyama, Phys. Rev. B **60**, 14561 (1999). 33, 145

[139] A. Gibaud, N. Cowlam, G. Vignaud, and T. Richardson, Phys. Rev. Lett. **74**, 3205 (1995). 33, 145

[140] J. K. Basu, S. Hazra, and M. K. Sanyal, Phys. Rev. Lett. **82**, 4675 (1999). 34, 146, 154

[141] J. K. Basu and M. K. Sanyal, Phys. Rep. **363**, 1 (2002).

[142] X.-H. Li, M. Li, and Z.-H. Mai, Phys. Rev. B **69**, 235407 (2004). 33, 145

[143] J. A. Zasadzinski, R. Viswanathan, L. Madsen, J. Garnaes, and D. K. Schwartz, Science **263**, 1726 (1994). 34, 35, 145, 146

[144] T. Geue, M. Schultz, U. Englisch, R. Stömmer, and U. Pietsch, J. Chem. Phys. **110**, 8104 (1990). 34, 146

[145] V. M. Kaganer, H. Möhwald, and P. Dutta, Rev. Mod. Phys. **71**, 779 (1999). 34, 171

[146] R. Viswanathan, J. A. Zasadzinski, and D. K. Schwartz, Science **261**, 449 (1993). 34

[147] A. Malik, M. K. Durbin, A. G. Richter, K. G. Huang, and P. Dutta, Phys. Rev. B **52**, R11654 (1995). 34, 145, 146

[148] V. Nitz et al., Phys. Rev. B **54**, 5038 (1996). 145

[149] J. B. Peng, G. T. Barnes, and I. R. Gentle, Adv. Colloid Interface Sci. **91**, 163 (2001). 34, 146

[150] J. A. Spink, J. Coll. Interf. Sci. **23**, 9 (1967). 34

[151] R. Viswanathan, D. K. Schwartz, J. Garnaes, and J. A. N. Zasadzinski, Langmuir **8**, 1603 (1992). 35

[152] V. A. Shchukin and D. Bimberg, Rev. Mod. Phys. **71**, 1125 (1999). 35, 146

[153] C. Y. Ruan, V. A. Lobastov, F. Vigliotti, S. Chen, and A. H. Zewail, Science **304**, 80 (2004).

[154] P. L. Silvestrelli, F. Toigo, and F. Ancilotto, J. Phys. Chem. B **110**, 12022 (2006). 35, 146

[155] G. Kissinger and W. Kissinger, phys. stat. sol. a **123**, 185 (1991). 36

[156] S. Adachi, T. Arai, and K. Kobayashi, J. Appl. Phys. **80**, 5422 (1996). 36, 184

[157] P. J. Kelly and R. D. Arnell, Vacuum **56**, 159 (2000). 39

[158] J. A. Thorton, J. Vac. Sci. Technol. **15**, 171 (1978).

[159] R. K. Waits, J. Vac. Sci. Technol. **15**, 171 (1978). 39

[160] S. A. Campbell, *The Science and Engineering of Microelectronic Fabrication*, Oxford University, New York, 1996. 40, 118

[161] L. G. Jacobsohn and F. L. Freire, J. Vac. Sci. Technol. **A17**, 2841 (1999). 41

[162] T. K. Subramanyam, B. S. Naidu, and S. Uthana, Cryst. Res. Technol. **35**, 1193 (2000). 41

[163] R. S. Robinson, J. Vac. Sci. Technol. **16**, 185 (1979). 41

[164] Y. Lifshitz, S. R. Kasi, and J. W. Rabalais, Phys. Rev. Lett. **62**, 1290 (1989). 41

[165] R. W. James, *The Optical Principles of the Diffraction of X-Rays*, Bell and sons, London, 1948. 53

[166] L. D. Landau and E. M. Lifshitz, *Electrodynamics of continuous media: Course of Theoretical Physics vol 8*, Pergamon, Oxford, 1960. 53, 54

[167] D. Oxtoby, F. Novack, and S. A. Rice, J. Chem. Phys. **76**, 5278 (1982). 53, 54

[168] L. G. Parratt, Phys. Rev. **95**, 359 (1954). 62

[169] S. Kundu et al., J. Phys. D: Appl. Phys. **31**, L73 (1998). 62, 118

[170] S. Morita, R. Wiesendanger, and E. Meyer, *Noncontact Atomic Force Microscopy*, Springer, Heidelberg, 2002. 62

[171] D. Sarid, *Scanning Force Microscopy*, Oxford University, New York, 1994. 62, 65

[172] C. J. Chen, *Introduction to Scanning Tunneling Microscopy*, Oxford University, New York, 1993. 68, 79

[173] I. Horcas et al., Rev. Sci. Instrum. **78**, 013705 (2007). 73

[174] U. Gösele and H. Strunk, Appl. Phys. **20**, 265 (1979). 78

[175] A. V. Vaisleib, M. G. Goldiner, O. Y. Keloglu, and I. N. Kotov, J. Appl. Phys. **70**, 6809 (1991). 78

[176] L. C. Ciacchi and M. C. Payne, Phys. Rev. Lett. **95**, 196101 (2005). 78

[177] T. Watanabe, K. Tatsumura, and I. Ohdomari, Phys. Rev. Lett. **96**, 196102 (2006). 78

[178] L. A. Baker, A. R. Laracuente, and L. J. Whitman, Phys. Rev. B **71**, 153302 (2005). 78

[179] H. D. Hallen, A. Fernandez, T. Huang, R. A. Buhrman, and J. Silcox, J. Vac. Sci. Technol. B **9**, 585 (1991). 79

[180] V. N. Antonov, J. S. Palmer, P. S. Waggoner, A. S. Bhatti, and J. H. Weaver, Phys. Rev. B **70**, 045406 (2004). 79

[181] J. J. Boland, Phys. Rev. Lett. **65**, 504 (1990). 79

[182] D. A. Edwards, J. Polym. Sci., Part B: Polym. Phys. **34**, 981 (1996). 87

[183] A. J. Liu and S. R. Nagel, *Jamming and Rheology: Constrained Dynamics on Microscopic and Macroscopic Scales*, Taylor & Francis, London, 2001.

[184] G. Hornung, B. Berkowitz, and Barkai, Phys. Rev. E **72**, 041916 (1995). 87

[185] S. K. Sinha, E. B. Sirota, S. Garoff, and H. B. Stanley, Phys. Rev. B **38**, 2297 (1988). 92, 95

[186] F. Family and T. Viscek, *Dynamics of Fractal Surface*, World Scientic, Singapore, 1991. 92

[187] J. A. Kubby and J. J. Boland, Surf. Sci. Rep. **26**, 61 (1996). 100

[188] A. Korkin, J. C. Greer, G. Bersuker, V. V. Karasiev, and R. J. Bartlett, Phys. Rev. B **73**, 165312 (2006). 100

[189] A. Fick, Phil. Mag. **10**, 30 (1855). 104, 108

[190] A. F. W. Willoughby, Rep. Prog. Phys. **41**, 1665 (1978). 107

[191] M. J. Aziz, S. Circone, and C. B. Agee, Nature **390**, 596 (1997). 108

[192] R. B. Stinchcombe and F. D. A. A. ao Reis, Phys. Rev. B **77**, 035406 (2008). 108

[193] H. B. Vanfleet, D. L. Decker, and H. R. Curtin, Phys. Rev. B **5**, 4849 (1972). 109, 110

[194] P. M. Fahey, P. B. Griffin, and J. D. Plummer, Rev. Mod. Phys. **61**, 289 (1989).

[195] O. Sugino and A. Oshiyama, Phys. Rev. B **46**, 12335 (1992).

[196] M. J. Aziz et al., Phys. Rev. B **73**, 054101 (2006).

[197] N. E. B. Cowern, Phys. Rev. Lett. **99**, 155903 (2007). 109, 110

[198] H.-J. Gossmann et al., Appl. Phys. Lett. **63**, 639 (1993). 110

[199] Z. H. Jafri and W. P. Gillin, J. Appl. Phys. **81**, 2179 (1993).

[200] S. C. Jain et al., J. Appl. Phys. **91**, 8919 (2002). 110

[201] P. Buffat and J.-P. Bore, Phys. Rev. A **13**, 2287 (1976). 110

[202] B. Gergen, H. Nienhaus, W. H. Weinberg, and E. W. McFarland, Science **294**, 2521 (2001). 117

[203] L. Gavioli, K. R. Kimberlin, M. C. Tringides, J. F. Wendelken, and Z. Zhang, Phys. Rev. Lett. **82**, 129 (1999). 118

[204] S. Banerjee, S. Mukherjee, and S. Kundu, J. Phys. D: Appl. Phys. **34**, L87 (2001). 118

[205] T. Castro, R. Reifenberger, E. Choi, and R. P. Andres, Phys. Rev. B **42**, 8548 (1990). 118

[206] S. Mathew, B. Satpati, B. Joseph, and B. N. Dev, Appl. Surf. Sci. **249**, 31 (2005). 118, 130

[207] J. C. Glueckstein, M. M. R. Evans, and J. Nogami, Phys. Rev. B **54**, R11066 (1996). 131

[208] J. M. Zuo and B. Q. Li, Phys. Rev. Lett. **88**, 255502 (2002). 131

[209] J. S. Palmer, P. Swaminathan, S. Babar, and J. H. Weaver, Phys. Rev. B **77**, 195422 (2008). 131

[210] R. Rosenberg, D. C. Edelstein, C.-K. Hu, and K. P. Rodbell, Annu. Rev. Mater. Sci. **30**, 229 (2000). 133

[211] S. P. Murarka and S. W. Hymes, Crit. Rev. Solid State Mater. Sci. **20**, 87 (1995).

[212] S. P. Murarka, I. V. Verner, and R. J. Gutmann, *Copper-Fundamental Mechanisms for Microelectronic Applications*, Wiley, New York, 2000. 133

[213] D. R. Lide, *CRC Handbook of Chemistry and Physics*, CRC Press, New York, 2000. 133

[214] K. Nagao, J. B. Neaton, and N. W. Ashcroft, Phys. Rev. B **68**, 125403 (2003). 133

[215] T. Nakahara, S. Ohkura, F. Shoji, and T. Hanawa, Nucl. Instrum. Methods B **45**, 467 (1990). 134

[216] A. Hiraki, Surf. Sci. Rep. **3**, 357 (1984)). 143

[217] T. Itoh and J. W. Gibson, J. Vacuum Sci. Tcchnol. A **2**, 561 (1984)). 143

[218] G. Rossi, I. Abbati, L. Braicovich, I. Lindau, and W. E. Spiccr., Solid State Commun. **39**, 195 (1981)). 143

[219] A. Ulman, *Introduction to Ultrathin Organic Films*, Academic Press, New York, 1991. 145

[220] K. B. Blodgett and I. Langmuir, Phys. Rev. **51**, 964 (1937). 145

[221] J. K. Bal and S. Hazra, Phys. Rev. B **79**, 155412 (2009). 146, 150, 156, 157, 159, 172

[222] S. Kundu, A. Datta, and S. Hazra, Phys. Rev. E **73**, 051608 (2006). 147

[223] S. Mukherjee, A. Datta, A. Giglia, N. Mahne, and S. Nannarone, Chem. Phys. Lett. **451**, 80 (2008). 160

[224] J. Kmetko, A. Datta, G. Evmenenko, and P. Dutta, J. Phys. Chem. B **105**, 10818 (2001). 171

[225] M. Dai, Y. Wang, J. Kwon, M. D. Halls, and Y. J. Chabal, Nature Materials **8**, 825 (2009). 171

[226] X. Zhang, E. Garfunkel, Y. J. Chabal, S. B. Christman, and E. E. Chaban, Appl. Phys. Lett. **79**, 4051 (2001).

[227] S. Rivillon, F. Amy, Y. J. Chabal, and M. M. Frank, Appl. Phys. Lett. **85**, 2583 (2004). 171

[228] M. Niwano et al., J. Appl. Phys. **76**, 2157 (1994). 171

[229] T. Ohmi, J. Electrochem. Soc. **143**, 2957 (1996).

[230] E. S. Snow, G. G. Jernigan, and P. M. Cambell, Appl. Phys. Lett. **76**, 1782 (2000). 171

[231] Y. J. Chabal and S. B. Christman, Phys. Rev. B **29**, 6974 (1984). 171

[232] M. Ranke and Y. R. Xing, Surf. Sci. **157**, 339 (1985).

[233] E. Kondoh, M. R. Baklanov, F. Jonckx, and K. Maex, Mater. Sci. Semicond. Process. **1**, 107 (1998). 171

[234] T. Hanada and M. Kawai, Vacuum **41**, 650 (1990). 171, 182

[235] D. Graf, M. Grundner, D. Muhlhoff, and M. Dellith, J. Appl. Phys. **69**, 7620 (1991).

[236] S. Xu et al., J. Mater. Sci. Technol. **9**, 437 (1993).

[237] N. Takano, N. Hosoda, T. Yamada, and T. Osaka, Electrochemica Acta **44**, 3743 (1999). 171, 182

[238] J. K. Bal, S. Kundu, and S. Hazra, Phys. Rev. B **81**, 045404 (2010). 172

[239] D. Graf, M. Grundner, and R. Chulz, J. Vac. Sci. Technol. A **7**, 808 (1989). 181

[240] J. K. Bal and S. Hazra, Defect Diffus. Forum **297-301**, 1133 (2010). 182, 183

[241] D. J. Michalak et al., Nature Materials **8**, 825 (2009). 182

[242] A. Hiraki, Surf. Sci. Rep. **3**, 357 (1983). 182

[243] J. K. Bal and S. Hazra, Phys. Rev. B **79**, 155405 (2009). 182

[244] F. J. Himpsel, F. R. McFeely, A. Taleb-Ibrahimi, J. A. Yarmoff, and G. Hollinger, Phys. Rev. B **38**, 6084 (1988). 185

[245] A. Pasquarello, M. S. Hybertsen, and R. Car, Phys. Rev. B **53**, 10542 (1996). 185

List of publications in journals

Related to my thesis:

1. Interfacial role in room-temperature diffusion of Au into Si substrates,

   J. K. Bal and S. Hazra, *Phys. Rev. B*, **75**, 205411 (2007).

2. Atmospheric pressure induced atomic diffusion into solid crystal,

   J. K. Bal and S. Hazra, *Phys. Rev. B*, **79**, 155405 (2009).

   [Highlighted in *Virtual Journal of Nanoscale science & Technology, vol. 19 issue 15 (2009)*].

3. Time-evolution growth of Ag nanolayers on differently passivated Si(001) surfaces,

   J. K. Bal and S. Hazra, *Phys. Rev. B*, **79**, 155412 (2009).

4. Growth and stability of Langmuir-Blodgett films on OH-, H-, or Br-terminated Si(001),

   J. K. Bal, S. Kundu and S. Hazra, *Phys. Rev. B*, **81**, 045404 (2010).

   [One image is highlighted in *PRB Kaleidoscope (2010)*].

5. Evolution of interdiffused Gaussian-shape nanolayer in Au-Si(111) system at ambient condition,

   J. K. Bal and S. Hazra, *Defect Diffus. Forum*, **297-301**, 1133-1139 (2010).

6. Hydrophobic to hydrophilic transition of HF-treated Si surface during Langmuir-Blodgett film deposition,

   J. K. Bal, S. Kundu and S. Hazra, *Chem. Phys. Lett.* **500**, 90 (2010).

7. Role of metal ions and passivating elements on structure and stability of Langmuir-Blodgett films,

   J. K. Bal, S. Kundu and S. Hazra [*Communicated*].

Not related to my thesis:

1. Correlation between local structure and refractive index of e-beam evaporated (HfO_2-SiO_2) composite thin films,

   N. C. Das, N. K. Sahoo, D. Bhattacharyya, S. Thakur, N. M. Kamble, D. Nanda, S. Hazra, **J. K. Bal**, J. F. Lee, Y. L. Tai and C. A. Hsieh; *J. Appl. Phys.* **108**, 023515 (2010).